

**Monolithic coupled-cavity laser diodes
for bio-sensing applications**

Robert Thomas

PhD Thesis

School of Physics and Astronomy,
Cardiff University.

March 2012

DECLARATION

This work has not been submitted in substance for any other degree or award at this or any other university or place of learning, nor is being submitted concurrently in candidature for any degree or other award.

Signed (candidate) Date

STATEMENT 1

This thesis is being submitted in partial fulfillment of the requirements for the degree of PhD

Signed (candidate) Date

STATEMENT 2

This thesis is the result of my own independent work/investigation, except where otherwise stated. Other sources are acknowledged by explicit references. The views expressed are my own.

Signed (candidate) Date

STATEMENT 3

I hereby give consent for my thesis, if accepted, to be available for photocopying and for inter-library loan, and for the title and summary to be made available to outside organisations.

Signed (candidate) Date

Abstract

This thesis describes an investigation into the potential of coupled-cavity semiconductor lasers for bio-sensing applications. This has involved the design and development of a fabrication process for a novel micro-fluidic coupled-cavity laser sensor. The efficiency of the etched inner laser facets of this device have been identified as a key determinant of the device behaviour. The multi-section gain characterization technique has been used to measure the efficiency of these facets to be $\eta = 0.48 \pm 0.13$.

Perturbation of the optical coupling between the two laser sections of the device can induce a wavelength shift in the laser output of $\Delta\lambda = 20 \pm 5 \text{ \AA}$. This wavelength change is attributed to the difference in the threshold gain requirements of the coupled-cavity and individual cavity modes of the device. A multi-mode travelling wave rate equation model has been used to predict that the size of this effect can be maximized by optimizing the cavity lengths of the device. For the AlGaInP quantum well material used in this work the coupling effect is maximized by using the shortest cavity lengths possible that can still achieve laser action.

The utility of including a segmented contact system to the coupled-cavity design has also been investigated. This modification enables wavelength tuning via the gain lever effect and self-pulsation through saturable absorption. A wavelength tuning range of $\Delta\lambda = 1.2 \pm 0.2 \text{ nm}$ has been measured for a single cavity laser with a segmented contact length ratio of 4:1. This tuning behaviour has been attributed to the carrier density dependence of the net modal gain peak. Rate equation modelling has been used to interpret the self-pulsation behaviour of the segmented contact device and to demonstrate how optical pumping of a saturable absorber can increase the sensitivity of the coupled-cavity device.

Acknowledgements

I would like to thank my supervisor Prof. Peter Smowton for giving me the opportunity to carry out this research and encouraging me through the difficult periods of this project. I am especially grateful to Peter for taking me on as his student when my original supervisor left the University during my first year.

I would also like to thank the members of the technical staff who have helped me during my studies. In particular, Chris Dunscombe for his help with wire bonding, Ian Robinson who helped me with AFM measurements and Rob Tucker who etched PCB boards for me and generally helped with all things electrical.

I would like to acknowledge Dr Gareth Edwards and Sam Shutts for their work on AlGaInP plasma etching which has been of great benefit to me, and Dr Angela Sobiesierski and Dr Haoling Liu for the many interesting discussions, in particular regarding self-pulsation in laser diodes.

Most importantly I would like to thank my parents for their continuous support throughout this time.

Conference presentations

“Coupled-cavity edge-emitting laser for biosensing applications” R. Thomas, P. M. Smowton, H. D. Summers and G. T. Edwards, Photonics West 2010.

CHAPTER 1: INTRODUCTION AND BACKGROUND	1
1.1 Introduction	1
1.2 laser diodes: basic principles.....	6
1.2.1 The semiconductor gain medium.....	6
1.2.2 The p-n junction	10
1.2.3 Optical resonator.....	11
1.2.4 Threshold gain and longitudinal modes.....	12
1.3 Quantum well lasers	14
1.3.1 The double heterostructure	14
1.3.2 Quantum confinement.....	16
1.4 Semiconductor coupled-cavity lasers	19
1.4.1 The gap coupler	20
1.4.2 Coupled-cavity modes.....	24
1.5 Summary	29
CHAPTER 2: DEVICE FABRICATION	31
2.1 Introduction	31
2.2 Design concept.....	32
2.3 Quantum well material	33
2.4 Device design	34
2.5 Fabrication	36
2.5.1 Etched laser facets	36
2.5.2 Electrical contacts.....	40
2.5.3 Deep-etched channels.....	41
2.5.4 Integrated SU-8 micro-fluidics	42
2.5.5 Cleaving and packaging	44
2.6 Summary	46
CHAPTER 3: CHARACTERISATION OF ETCHED LASER FACETS	48
3.1 Introduction	48
3.2 Multi-section technique.....	50
3.2.1 Multi-section device	50
3.2.2 Measurement principle	51
3.2.3 Experimental procedure.....	53
3.2.4 Multi-section results.....	54
3.3 Cleaved and etched facet laser threshold measurements	56
3.3.1 Laser devices	56
3.3.2 Experimental Procedure.....	57
3.3.3 Results	57
3.4 Surface roughness phase broadening model.....	61
3.4.1 AFM surface roughness measurement	62
3.4.2 Results	63
3.5 Summary	67

CHAPTER 4: THE COUPLED-CAVITY SENSOR	69
4.1 Introduction	69
4.2 Light source/photo-detector configuration	71
4.3 Coupled-cavity modes.....	74
4.4 Coupled-cavity sensing mechanism	78
4.5 Multi-mode travelling-wave rate equation model	81
4.5.1 Rate equations	81
4.5.2 Gain functions	85
4.6 Coupled-cavity simulations	87
4.6.1 Coupling of spectrally misaligned laser sections.....	87
4.6.2 Optimisation of cavity lengths	89
4.7 Summary	92
CHAPTER 5: GAIN-LEVERING AND SELF-PULSATION	94
5.1 Introduction	94
5.2 Wavelength tuning in segmented contact quantum well lasers	96
5.2.1 Wavelength tuning results	99
5.2.2 Wavelength tuning analysis	101
5.2.3 Optimisation of the tuning range.....	105
5.3 Self-pulsation.....	106
5.3.1 Net modal gain spectra as a function of reverse bias.....	107
5.3.2 Light – current characteristics with reverse bias	108
5.3.3 Self-pulsation analysis	110
5.3.4 Frequency tuning with optical pumping	112
5.3.5 Optical pump sensor	113
5.4 Summary	114
CHAPTER 6: SUMMARY AND CONCLUSIONS	116
6.1 Conclusions	116
6.2 Future work.....	118
Appendix 1 Scattering matrix elements	121
Appendix 2 Gaussian beam gap loss model	124
Appendix 3 Table of cleaved and etched facet laser properties.....	128

Chapter 1:

Introduction and background theory

1.1 Introduction

Human life expectancy has steadily increased over the last century due in large part to the advances that have been made in biomedical research [1]. Crucial to these advances are the cytometric techniques that have been developed for the investigation of cell biology. Since its invention over 400 years ago, the microscope in its various forms has been the mainstay of the cell biologist; together with modern cell staining technologies the microscope can provide detailed information regarding both cell form and function. However, analysing large numbers of cells in this way is a time-consuming and labour-intensive process and the image data that is produced, whilst detailed, does not lend itself readily to statistical analysis.

The invention of the laser in 1960 enabled new cytometric techniques such as flow cytometry to emerge that overcame the limitations of microscopy by significantly increasing the rate at which statistical cell population data can be obtained. The flow cytometer processes large numbers of cells rapidly by passing them in a single file, suspended in a fluid stream, through a laser beam, see figure 1.1. Multiple cellular parameters can then be determined simultaneously by measuring the fluorescence and light scatter from each cell as it passes through the laser beam using an array of sensitive photo-multiplier tubes and photo-detectors.

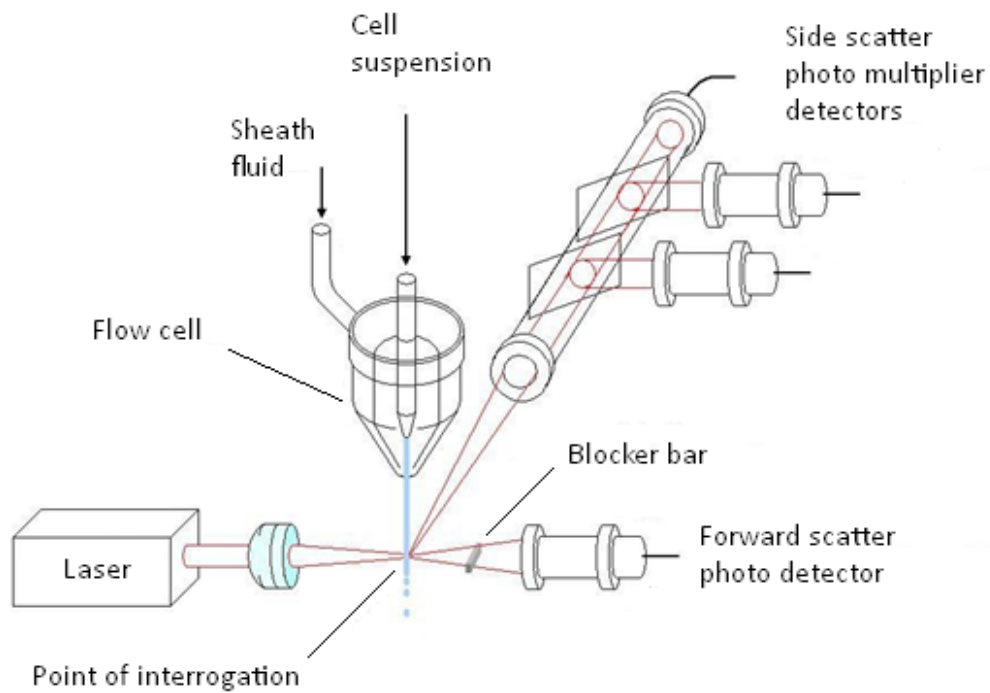


Figure 1.1 Schematic illustration of a flow cytometer showing the position of the optical components in relation to the fluid stream containing cells (after [1]).

The results of each measured parameter can be analysed individually but more typically the data is analyzed by comparing two different parameters in a cytogram, see figure 1.2.

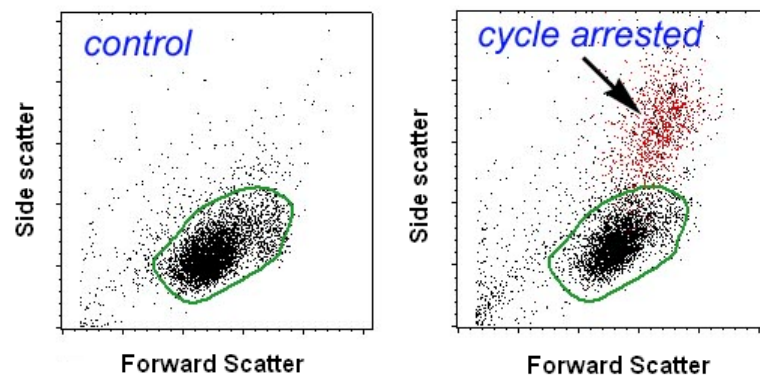


Figure 1.2 Example of a flow cytometer data set, which can be interpreted as cell cycle arrest in a population of cells[†]. Plotting the forward and side scattered light against one another allows the two distinct cell populations to be resolved.

[†]Private communication with Professor H. D. Summers, Multidisciplinary Nanotechnology Centre, Swansea University SA2 8PP, U.K.

Flow cytometry is the standard for statistical cell biology, however, flow cytometers are large and costly machines and the reliability of results depends on regular calibration and careful sample preparation.

In recent years, interest in micro total analysis systems (μ TAS) has led to the creation of a new generation of smaller, cheaper biosensors that hybridizes semiconductor lasers with micro-fluidic cell delivery chips in order to provide rapid in situ biological analysis [2, 3]. An example of this approach is the external cavity laser sensor [2], see figure 1.3. A 215 μ m long InGaAsP laser diode is integrated into a micro-fluidic chip package fabricated in polydimethylsiloxane (PDMS) on a glass substrate. A micro-fluidic channel passes cells through an external cavity formed between the laser and an external reflector. The refractive index of the cell can be measured from the change brought about in the output power of the laser due to change in the optical path length of the external cavity caused by the presence of the cell.

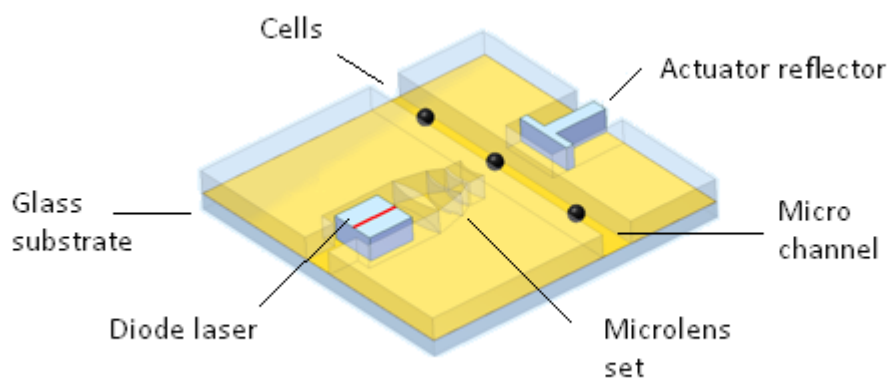


Figure 1.3 Illustration of a hybrid external cavity laser/micro-fluidic chip that can be used to measure the refractive index of cells (after [2]).

Another aspect of semiconductor based photonics which has not been utilised to the same degree is the potential for monolithic integration of the cell delivery micro-fluidics into the optically-active semiconductor. In this work a micro-fluidic coupled-cavity (MFCC) laser sensor is proposed, in which, cells may be passed through the gap coupler sections of an array of coupled-cavity lasers via a micro-fluidic channel etched into the semiconductor crystal, see figure 1.4. In theory, both the wavelength and output power of the device are dependent on the strength of coupling between the two laser sections. Perturbation of the gap coupler scattering losses, caused by a passing cell, should therefore be evident in the output of the device, making for a potentially highly sensitive detection mechanism. Furthermore, the monolithic nature of this design offers significant advantages in terms of achieving good alignment and close proximity between the sensor and the analyte.

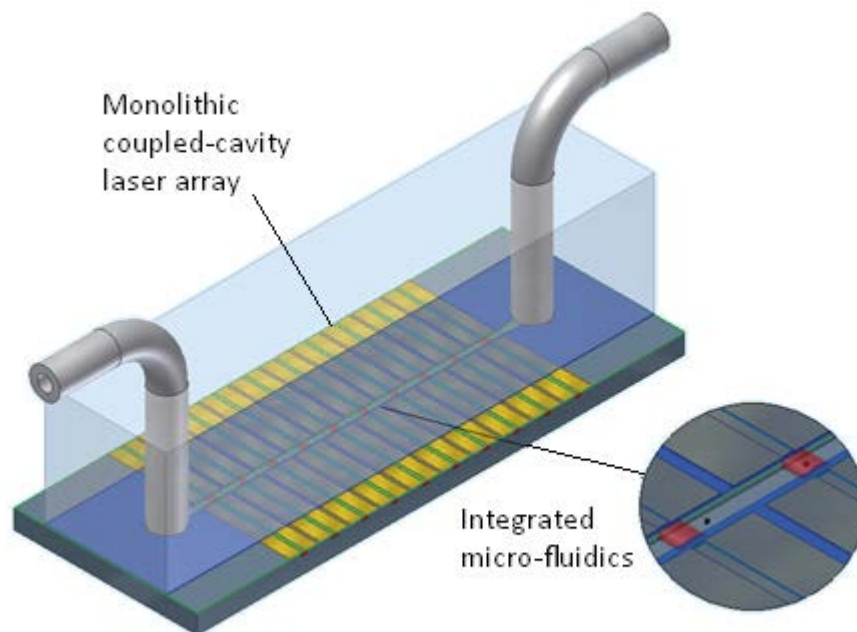


Figure 1.4 Illustration of the proposed monolithic coupled-cavity laser sensor with integrated micro-fluidics. **Inset** cells pass through the gap couplers of the arrayed coupled-cavity lasers as they travel along the micro-fluidic channel.

The aim of this project has been to investigate how the optical coupling that exists within a monolithic coupled-cavity laser might be used as a bio-sensing mechanism. This thesis presents the theoretical and experimental results of this investigation.

The following sections of this chapter provide some of the necessary background theory relating to semiconductor lasers, in particular quantum well and coupled-cavity devices. Chapter 2 includes a discussion of the design and fabrication work that has been carried out to develop a prototype MFCC device. The monolithic nature of this design requires that the inner laser facets of the device are created using a plasma etching process. The coupling strength, and therefore the sensitivity, of the device, is expected to be highly dependent on the efficiency of the etched facets. A priority of this work, therefore, has been to develop a methodology for the characterisation of etched laser facets; the results of this study are presented in chapter 3.

In chapter 4 the sensing potential of the prototype device has been investigated experimentally using standard device characterisation techniques i.e. measurement of the light versus current characteristics and lasing spectra. Interpretation of these results has been carried out using a multi-mode travelling wave rate equation model, developed for the purpose of simulating experimental device behaviour. Chapter 5 explores how the sensitivity of the coupled-cavity device might be improved by using segmented contact lasers in order to facilitate wavelength tuning via the gain lever effect and self-pulsation by saturable absorption. Chapter 6 presents the conclusions of the thesis and discusses the direction future work might take in order to gain further insight into the behaviour of coupled-cavity laser sensors.

1.2 Laser diode basic principles

This section provides a brief description of the basic ingredients of the laser diode, the semiconductor gain medium that provides coherent amplification of light, electrical pumping of the medium at a p-n junction and the optical resonator that maintains the coherence of the light output and also imposes directionality on it.

1.2.1 The semiconductor gain medium

The most fundamental component of the laser is a gain medium that is capable of coherently amplifying light that passes through it. Modal gain can be defined as the fractional increase in the energy in an optical mode of the laser cavity, U , per unit distance travelled through the medium, L :

$$G = \frac{1}{U} \frac{\Delta U}{\Delta L} \quad (1.1)$$

In the case of a diode laser the gain medium is the crystal lattice of a semiconductor material. The valence electrons of an atom occupy discrete energy levels but when two atoms are brought together their valence electrons configure themselves in one of two possible energy states: a bonding state and an anti-bonding state. When lots of atoms come together to form the crystal lattice of a semiconductor, these bonding and anti-bonding states form into near continuous bands of closely spaced states separated by a forbidden energy gap E_g , see figure 1.5.

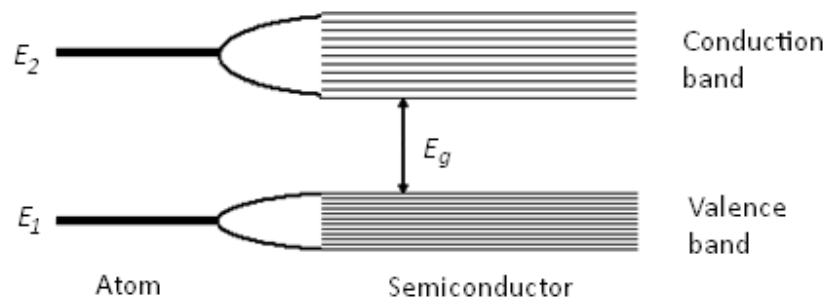


Figure 1.5 The discrete energy levels E_1 and E_2 of an atom split into bands of allowed energy states separated by a forbidden energy gap E_g in a semiconductor [4].

For an electron to make a transition between an energy state in the valence band and one in the conduction band it must do so by absorbing or emitting a quantum of energy equal to the energy difference between the two states. For transitions involving light, these energy quanta are photons, the frequencies of which are proportional to the energy difference of a transition:

$$h\nu = E_2 - E_1 \quad (1.2)$$

where the constant of proportionality h is Planck's constant (Js) and ν is the frequency of the light (s^{-1}). Momentum must also be conserved during the transition but, because photons have negligible mass, the electron must have the same momentum in both the initial and final states. The three different types of radiative transition that take place between the conduction and valence bands of the semiconductor are illustrated in figure 1.6.

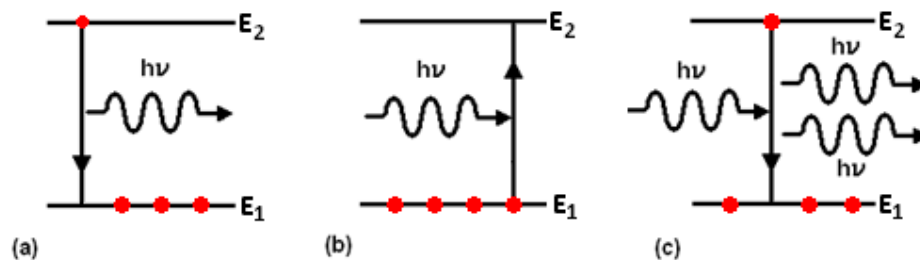


Figure 1.6 Radiative band-to-band transitions in a semiconductor: (a) spontaneous emission, (b) stimulated absorption and (c) stimulated emission.

Spontaneous emission: an electron occupying a state in the conduction band spontaneously drops down into a lower valence band energy state. In making this transition, the energy that had been stored in the system while it was in the higher energy state, is released in the form of a photon with a frequency corresponding to the energy difference between the two states. Whilst the frequency of the photon is well defined, its direction, phase and polarisation are random.

Stimulated absorption: an incident photon is absorbed promoting an electron from the valence band to the conduction band, leaving a positive net charge, or, hole, in the valence band. The rate at which this transition occurs is proportional to the probability of an electron occupying the lower state f_1 and the upper state being empty $(1 - f_2)$ and to the density of photons $P(h\nu)$ with energies equal to the difference in energy between the two states:

$$R_{12} = Rf_1(1 - f_2)\Gamma P(h\nu) \quad (1.3)$$

where R is the radiative transition rate constant and Γ is the confinement factor which represents the ratio of the gain region volume to the volume of the optical mode.

Stimulated emission: an electron occupying an energy state in the conduction band can be perturbed into a downward transition by an interaction with an incident photon. As with the spontaneous downward transition, as the electron recombines with a hole in the valence band it releases its stored energy in the form of a photon, this time however, the photon has the same direction, phase and polarization as that of the one that initiated the transition. If these two photons stimulate further downward transitions, the process quickly results in an avalanche of coherent photons. This coherent amplification of light is the basis of laser action. The downward transition rate for the stimulated emission process can be written as

$$R_{21} = Rf_2(1 - f_1)\Gamma P(h\nu) \quad (1.4)$$

where f_2 is the probability of an electron occupying an upper state and $(1 - f_1)$ is the probability of the lower state being empty of electrons.

The probability of an electron occupying a state with energy E , in the conduction or valence band, can be described using Fermi-Dirac statistics:

$$f_2 = \frac{1}{1 + \exp\left(\frac{E_2 - E_{fc}}{kT}\right)} \quad (1.5)$$

$$f_1 = \frac{1}{1 + \exp\left(\frac{E_1 - E_{fv}}{kT}\right)} \quad (1.6)$$

where E_{fc} and E_{fv} are quasi Fermi energies for the electrons in the conduction band and the valence band respectively (eV), k is the Boltzmann constant (eV K⁻¹) and T is the temperature (K).

In order to achieve net amplification of the light as it propagates through the material i.e. optical gain, the stimulated emission rate must exceed the stimulated absorption rate and the ratio of the stimulated rates, once the occupation functions have been substituted, yields

$$\frac{R_{21}}{R_{12}} = \frac{f_2(1 - f_1)}{f_1(1 - f_2)} = e^{\frac{\Delta E_F - (E_2 - E_1)}{kT}} \quad (1.7)$$

Equation 1.7 demonstrates that to achieve positive optical gain, the quasi-Fermi level separation ΔE_F must be greater than photon energy, which itself must be at least as large as the band gap energy of the semiconductor material:

$$E_{fc} - E_{fv} \equiv \Delta E_F > h\nu \geq E_g \quad (1.8)$$

This non-equilibrium condition, known as population inversion, can be maintained by electrically injecting charge carriers into the semiconductor at a p-n junction.

1.2.2 The p-n junction

The conductivity of an intrinsic semiconductor can be improved by doping it with impurity atoms that contribute free charge carriers to the crystal lattice. If the dopant atoms donate free electrons to the material, it is said to be n-type and the Fermi energy is raised towards the conduction band. Alternatively, if the dopant atoms accept valence electrons, then the material is p-type and the Fermi energy moves towards the valence band. A p-n junction is formed at an interface between a p-type and an n-type semiconductor material. Free electrons and holes in the vicinity of the junction can diffuse across it and recombine with one another, leaving a net ionic charge on each side. The resulting potential difference between the two sides opposes further diffusion and a depletion region with no free charge carriers is formed at the junction.

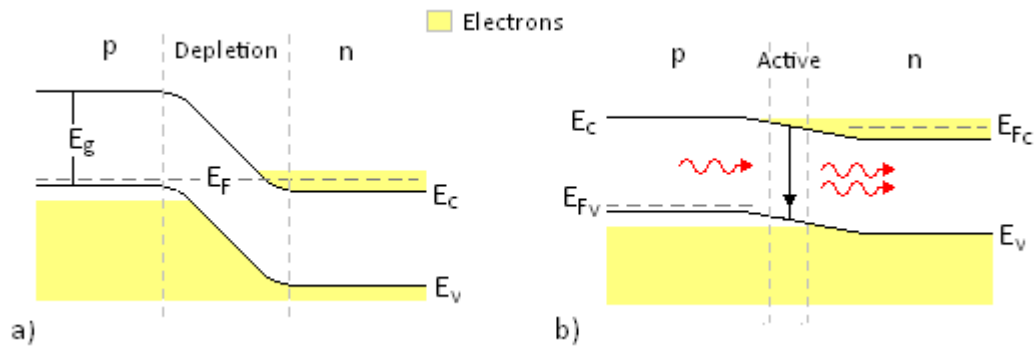


Figure 1.7 Energy band diagram of p-n junction at (a) zero bias and (b) Forward biased

If no external voltage is applied and the system is in thermal equilibrium, the Fermi energy on each side of the junction must be the same. The application of an external forward bias across the device raises the potential energy of the electrons on the n-side with respect to those on the p-side, effectively separating the Fermi energies of each and reducing the built-in junction potential. In this non-equilibrium state, electrons and holes can continuously diffuse into an active region where they are able to radiatively recombine by emitting a photon. In order to achieve positive optical gain in this active region, the condition set by equation 1.8 requires that the quasi Fermi level separation produced by the applied voltage, must be equal to, or greater than, the band gap energy of the material ($eV = \Delta E_F \geq E_g$).

1.2.3 The optical resonator

The directionality and phase coherence that characterise the stimulated emission process are maintained within a laser device by placing the gain medium inside an optical resonator. For diode lasers, the resonator, in its simplest form, can be created by cleaving the semiconductor along crystal planes to create two partially reflecting mirrors that are parallel to one another, illustrated in figure 1.8, (R_1 and R_2 are the power reflectivity coefficients of the two mirrors).

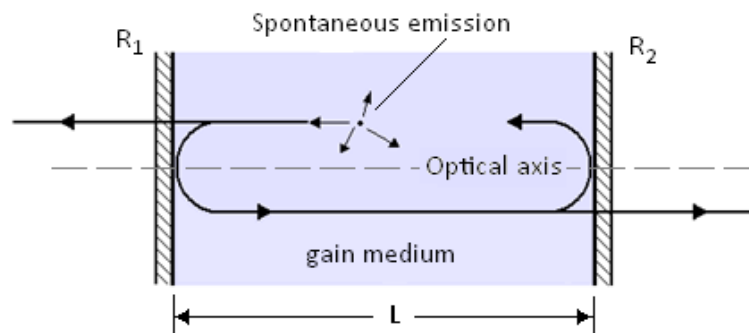


Figure 1.8 Optical feedback of amplified spontaneous emission inside the laser resonator.

Once population inversion has been achieved in the laser medium, spontaneous emission generated throughout the cavity, travelling in all directions, can be amplified by the stimulated emission process. The amplified spontaneous emission (ASE) travelling at an angle to the optical axis will either leave the cavity directly or leak away after several internal reflections. Only the light propagating in a direction parallel to the optical axis of the cavity will be reflected back and forth multiple times and, consequently, the coherence of the laser light is maintained within a discrete set of longitudinal cavity modes that are emitted from each facet along the direction of the optical axis.

1.2.4 Threshold condition and longitudinal modes

By integrating equation 1.1, it can be shown that the optical power in a mode propagating through the gain medium with an inverted carrier population, will increase exponentially with distance travelled. However, the mode will also suffer internal scattering losses and when confined within a resonator cavity, the fraction of light transmitted through the partially reflecting mirrors on each round trip also constitutes a cavity loss. When the level of population inversion is such that the modal gain exceeds the combined cavity losses, the optical power will increase on each round trip. This process cannot proceed unhindered however. As the intensity increases, it begins to deplete the inverted carrier population, which has the effect of suppressing the gain so that the round trip amplification is reduced and the light in the cavity diminishes. If electrical injection is maintained, the carrier population quickly recovers and the light level increases once again. This process repeats itself until, eventually, after several oscillations, the system relaxes towards a steady-state, where, ignoring the small contribution from the spontaneous emission to the optical mode, the round trip gain exactly equals the loss i.e. the net round trip amplification is equal to one [5]. This is shown schematically in figure 1.9.

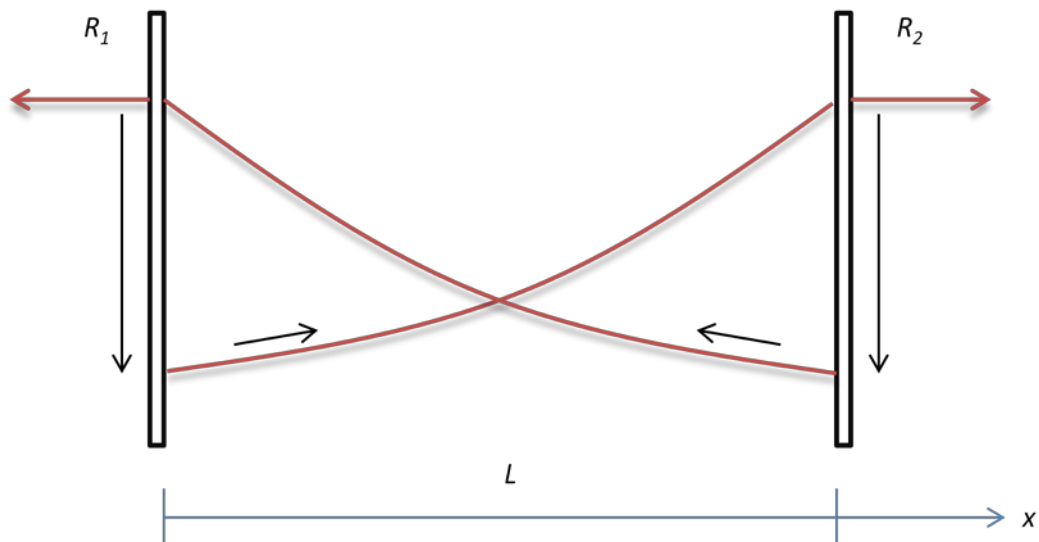


Figure 1.9 Schematic illustration of the round trip condition in the resonator cavity of a laser diode.

Approximating the electric field of an optical mode within the laser cavity as a sinusoidal plane wave solution to Maxwell's time independent wave equation for a medium with an induced electrical polarisation:

$$E(x) = E_0 \exp \left[i \left[n \left(\frac{2\pi}{\lambda_0} \right) - i \left(\frac{G - \alpha_i}{2} \right) \right] x \right] \quad (1.9)$$

where n is the refractive index of the gain medium and λ_0 is the wavelength of the light in vacuum and G and α_i are the modal gain and internal scattering loss respectively, the round trip condition can be expressed as

$$(R_1 R_2)^{\frac{1}{2}} \exp \left[2i \left[n \left(\frac{2\pi}{\lambda_0} \right) - i \left(\frac{G - \alpha_i}{2} \right) \right] L \right] = 1 \quad (1.10)$$

Simultaneously solving the real and imaginary parts of equation 1.10 yields the modal gain threshold requirement i.e. the modal gain needed for the device to achieve laser action:

$$G_{th} = \alpha_i + \frac{1}{2L} \ln \left(\frac{1}{R_1 R_2} \right) \quad (1.11)$$

where the second term on the right hand side represents the distributed mirror loss. The periodic solutions to equation 1.10 also provide the wavelengths of the resonant longitudinal cavity modes:

$$\lambda_m = \frac{2nL}{m} \quad (1.12)$$

where m is an integer.

1.3 Quantum well lasers

The experimental devices used in this project have been fabricated exclusively from a single quantum well (SQW) GaInP/AlGaInP material. This section provides a brief description of the quantum well laser and related double heterostructure.

1.3.1 The double heterostructure

The p-n junction device described in section 1.2.2 is constructed from two differently doped layers of the same material. This homostructure design is simple but inefficient; the carriers are not well confined within the active region and the small refractive index step between layers allows the optical mode to spread out far beyond the active layer, resulting in poor optical confinement. The double-heterostructure illustrated in figure 1.10 was designed to tackle these inefficiencies. A heterojunction is an interface between two different semiconductor materials with different band gap energies. The double-heterostructure is formed by growing an active layer of narrow band gap material between two cladding layers with wider band gaps and lower refractive indices.

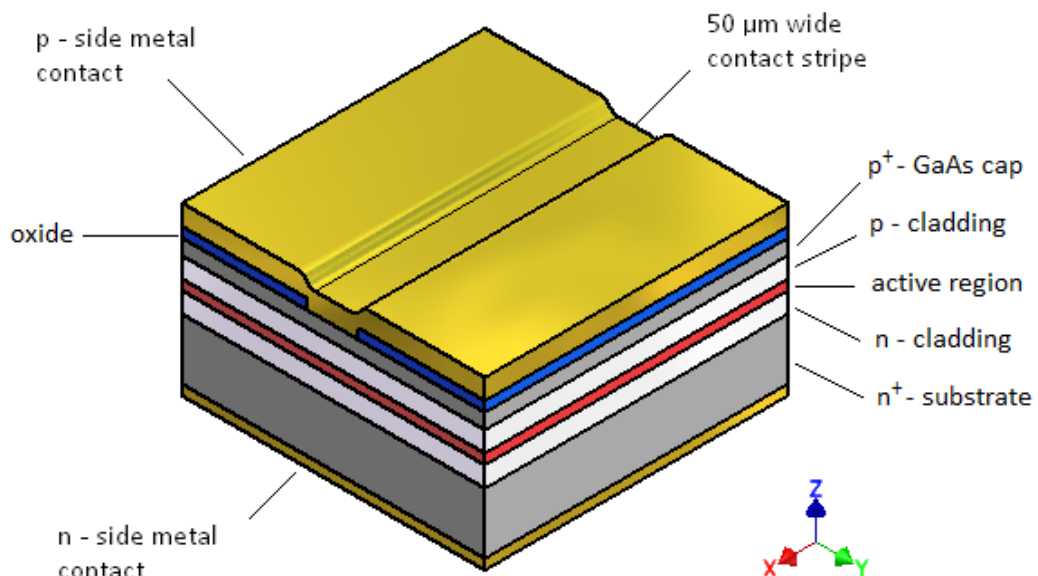


Fig 1.10 Illustration of the layer structure of a gain guided double-heterostructure laser diode.

The band gap energy difference between the layers of the double-heterostructure creates a potential energy barrier for electrons and holes in the active layer, helping to confine them to this region where they are more likely to recombine via the stimulated emission process, see figure 1.11. Simultaneously, the refractive index step created by the layer structure provides a degree of optical confinement between the layers in the z - direction. In the gain-guided device, illustrated in figure 1.10, the gain region is limited to a narrow area of electrical injection beneath the $50\mu\text{m}$ wide contact stripe. Any light propagating outside this region is readily absorbed due to the lack of gain which serves to confine the optical mode in the y - direction. Lateral confinement of the mode in both y and z directions effectively creates a slab waveguide within the device, increasing the overlap between the optical mode and the active region.

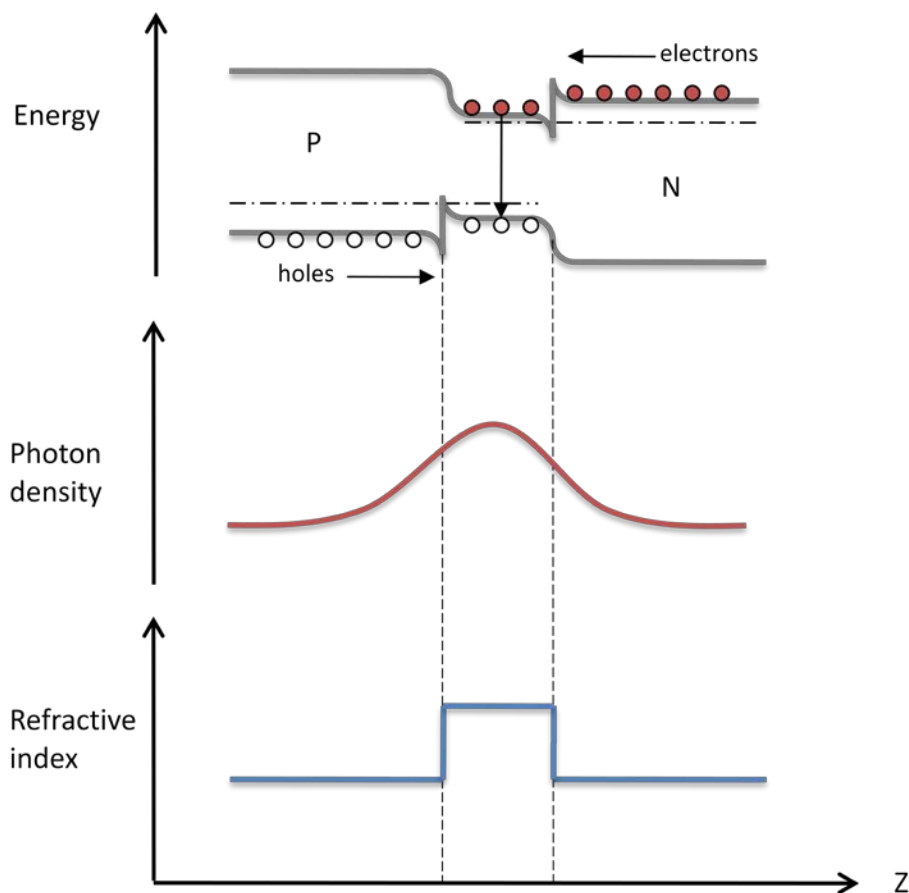


Figure 1.11 Schematic illustration of a forward biased double-heterostructure demonstrating the confinement of carriers due to the potential energy step between layers (top) and the confinement of light (middle) due to the refractive index step between layers (bottom).

1.3.2 Quantum confinement

A quantum well active region is formed when the thickness of the active layer is reduced to approximately the same scale as the de Broglie wavelength of the carriers in the material. Quantum confinement of the carriers in the z-direction then reduces the number of states available in the conduction and valence bands to a set of discrete energy levels (see figure 1.12).

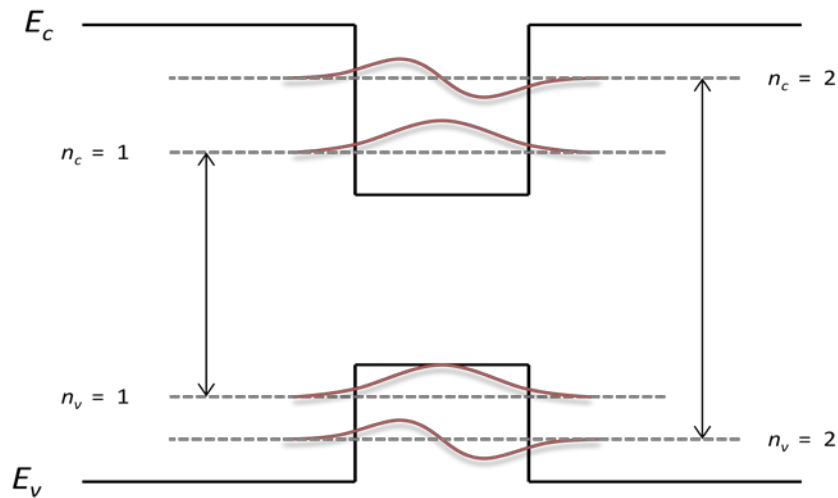


Figure 1.12 Discrete energy states in the conduction and valence bands of the quantum well illustrating the allowed transitions.

The energies of the confined states can be found by solving the time independent Schrödinger equation, which, for the limiting case of an infinite potential well, gives

$$E_n = \frac{\hbar^2}{2m_c^*} \left(\frac{n\pi}{L_z} \right)^2 \quad (1.13)$$

where \hbar is the reduced Planck constant, m_c^* is the effective mass of the electrons or holes confined within the well and L_z is the thickness of the well in the z-direction.

The energy difference between the allowed transitions, and hence the peak wavelength of the material, can be adjusted therefore (within a limited range) by selecting the appropriate well width.

Although the carriers are confined in the z-direction of the quantum well, they are still free to move in the x – y plane. The density of allowed energy states within the quantum well therefore depends on the number of solutions that satisfy Schrödinger’s equation for the boundary conditions imposed by the dimensions of the crystal in the x and y directions. This results in a density of states function corresponding to each of the confined energy states that is independent of energy

$$\rho_n(E) = n \frac{m_c^*}{\pi \hbar^2} \tag{1.14}$$

Summing the contributions from each of these sub-bands produces a step-like density of states function, $\rho(E)$, see figure 1.13.

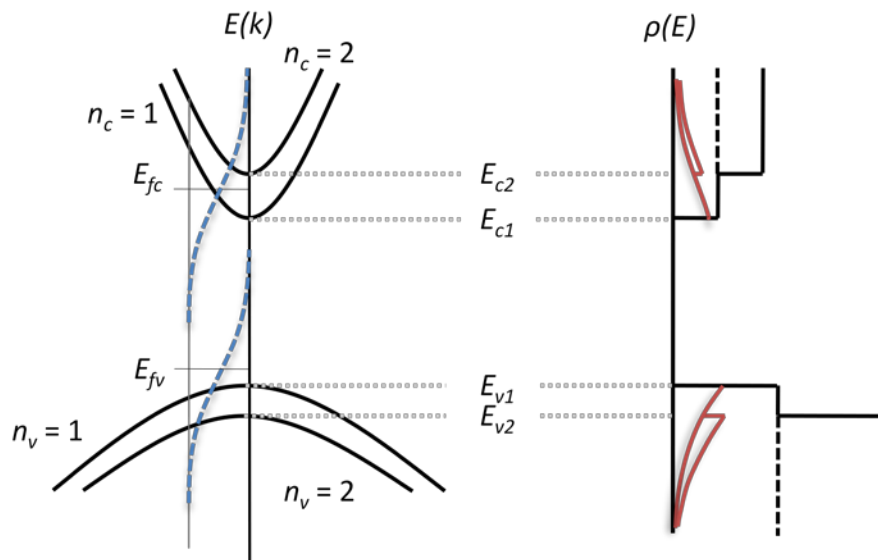


Figure 1.13 Parabolic sub-bands related to each of the quantum confined energy levels and the corresponding density of states, illustrating the relationship between the Fermi functions (dashed blue lines) and the carrier populations of the conduction and valence bands (red regions) (after [4]).

The density of states function represents the maximum number of energy states that can be occupied by carriers within a given energy range. The exact energy distribution of the carrier populations in each of the sub-bands therefore depends on how these available states are occupied, which, if the sample is in thermal equilibrium, can be determined using Fermi functions for conduction and valence bands (equations 1.5 and 1.6). In contrast to a bulk material, where the density of states function depends on the square root of the energy, in a quantum well the constant density of states results in carrier populations that are largest at the edges of the conduction and valence bands, see figure 1.13. The reduced occupation of higher lying energy states narrows the spontaneous emission spectrum of the quantum well in comparison to that of bulk semiconductors. Consequently, quantum well lasers are more efficient and have lower threshold current densities than devices made from bulk material.

1. 4 Semiconductor coupled-cavity lasers

Much of the early interest in coupled-cavity semiconductor lasers was generated by the potential offered for mode selectivity and wavelength tunability [5]. The defining theoretical work carried out at this time was therefore focused on optimising these properties [6, 7]. Henry et al developed a threshold gain model using the round trip condition for longitudinal modes in a coupled-cavity to define relationships between the wavelength tuning and mode selection behaviour of the device and key design parameters such as the laser cavity length ratios and the size of the gap coupler. In order to maximise coupling strength, gap coupler lengths are typically kept to a minimum (of the order of the lasing wavelength). For the micro-fluidic coupled-cavity (MFCC) device proposed in this project, a gap coupler length of 125 μm has been chosen to ensure that cells with diameters as large as 20 μm might easily be passed between the two laser sections of the device. Following the approach taken in this earlier work, a threshold gain model has been adapted to model the formation of coupled-cavity modes in devices with large gap couplers and etched laser facets.

The threshold gain requirement of the single cavity laser, described by equation 1.11, is, to first order, independent of wavelength. Each of the allowed cavity modes will therefore have the same value of threshold gain (in this case, mode discrimination is provided by the wavelength dependence of the gain medium i.e. the strongest lasing mode is the one that is closest to the peak of the material gain spectrum). For the coupled-cavity device, the threshold gain requirement of a given mode will depend, not only on the gain or loss that it experiences in each of the laser sections, but also on the mutual optical feedback that occurs within the gap coupler. The gap coupler is effectively a lossy optical resonator, light entering it from each of the active sections will be reflected back and forth multiple times. On each internal reflection, a fraction of the resonant light will leak back into the active sections of the device. As a result, the strength and phase of coupling between the two laser sections is wavelength dependent.

1.4.1 The gap coupler

The inter-cavity coupling of light between laser cavities with lengths L_1 and L_2 across a gap coupler with length L_g can be determined using a scattering matrix to describe the transmission and reflection of the electric fields E_1 and E_2 , see figure 1.14. Here r_1 and r_2 are the amplitude reflectivity coefficients for the facets of cavity 1 and cavity 2 respectively.

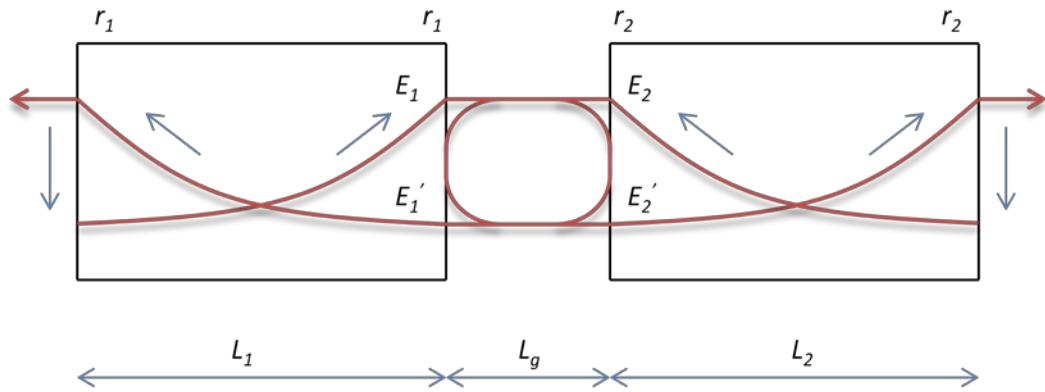


Figure 1.14 coupled-cavity laser geometry illustrating the coupling of two laser cavities via multiple round trips of the gap coupler.

E_1' and E_2' are the amplitudes of the electric fields that enter each of the laser cavities from the gap coupler. These amplitudes each result from the light reflected back from the gap into the cavity of origin, combined with the light transmitted across the gap from the cavity opposite, see equation 1.15.

$$\begin{pmatrix} E_1' \\ E_2' \end{pmatrix} = \begin{pmatrix} S_{11} & S_{12} \\ S_{21} & S_{22} \end{pmatrix} \begin{pmatrix} E_1 \\ E_2 \end{pmatrix} \quad (1.15)$$

Each of these components itself results from multiple internal reflections within the gap coupler. The matrix elements in equation 1.15 therefore represent complex transmission and reflection coefficients that are calculated by summing over each of the individual round trip contributions, see appendix 1. Assuming that the device

is symmetrical i.e. the refractive index is the same in each of the laser sections, then $r = r_1 = r_2$ and the reflection and transmission matrix elements can be written as

$$S_{11} = S_{22} = \sqrt{\eta} r - \frac{\sqrt{\eta} (1 - r^2)}{r} \sum_{p=1}^N F(2pL_g) [\eta r^2 t_g^2]^p \quad (1.16)$$

$$S_{12} = S_{21} = (1 - r^2) \sum_{p=1}^N F[2(p - 1)L_g] \eta^p (r^2)^{p-1} \cdot t_g^{2p-1} \quad (1.17)$$

respectively, where η is the efficiency of the gap coupler facets, $F(x)$ is the fraction of the electric field that is coupled into a laser section after travelling a distance x , see appendix 2 (this term accounts for the gap losses due to diffraction [8]) and t_g is a propagation coefficient that describes the phase dependence of the amplitude after a single pass of the gap coupler, see equation 1.18.

$$t_g = \exp\left(\frac{i2\pi L_g}{\lambda_g}\right) \quad (1.18)$$

where λ_g is the wavelength of light inside the gap coupler. The strength and phase dependence of the coupling can be expressed in the form of a complex coupling parameter which is defined as the ratio of the complex transmission and reflection coefficients:

$$\frac{S_{12}}{S_{11}} = C \exp(i\vartheta) \quad (1.19)$$

Where C is the magnitude and ϑ is the phase of the inter-cavity coupling.

The magnitude and phase of the coupling parameter have been plotted as a function of wavelength over a 10 nm range for the 125 μm gap coupler used in the MFCC design, see figure 1.15.

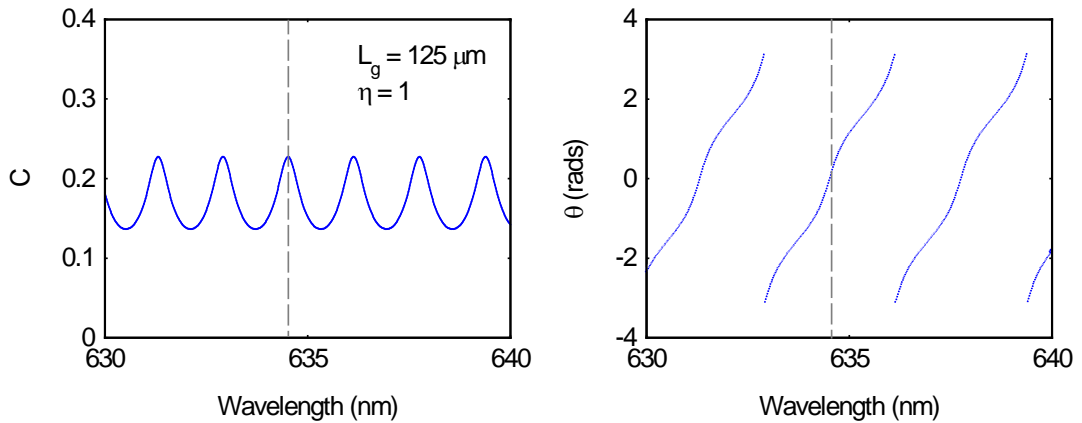


Figure 1.15 Magnitude C and phase ϑ of the coupling parameter plotted as a function of wavelength for a gap coupler length of $L_g = 125 \mu\text{m}$, a facet reflectivity of $r = 0.56$ and facet efficiency of $\eta = 1$. The dashed lines indicate an in-phase coupling maximum.

For gap couplers that are much larger than the wavelength of the laser sections, $L_g \gg \lambda_g$, resonance effects within the gap create a periodic spectral response in the coupling parameter. Strong in-phase coupling can only occur at wavelengths close to the peaks of the magnitude response that correspond to a phase shift of zero ($\vartheta = 0$), (see the example indicated by the dashed lines in figure 1.15). Thus, the gap coupler acts as a periodic band-pass filter that limits the allowed coupled-cavity modes to narrow wavelength bands close to the in-phase coupling maxima.

Due to the monolithic nature of the MFCC design, the gap coupler facets are fabricated using a plasma etching process (discussed in further detail in chapter 2). These etched facets have a lower efficiency than those of cleaved facets (assumed here to be 100% efficient i.e. $\eta = 1$). In chapter 3 the efficiency of etched facets has been measured to be $\eta = 0.48 \pm 0.13$. To model the effect of using etched facets in the MFCC gap coupler, the magnitude and phase of the coupling parameter have

been plotted as a function of wavelength for a gap coupler length of $L_g = 125 \mu\text{m}$ and a facet efficiency of $\eta = 0.5$, see figure 1.16.

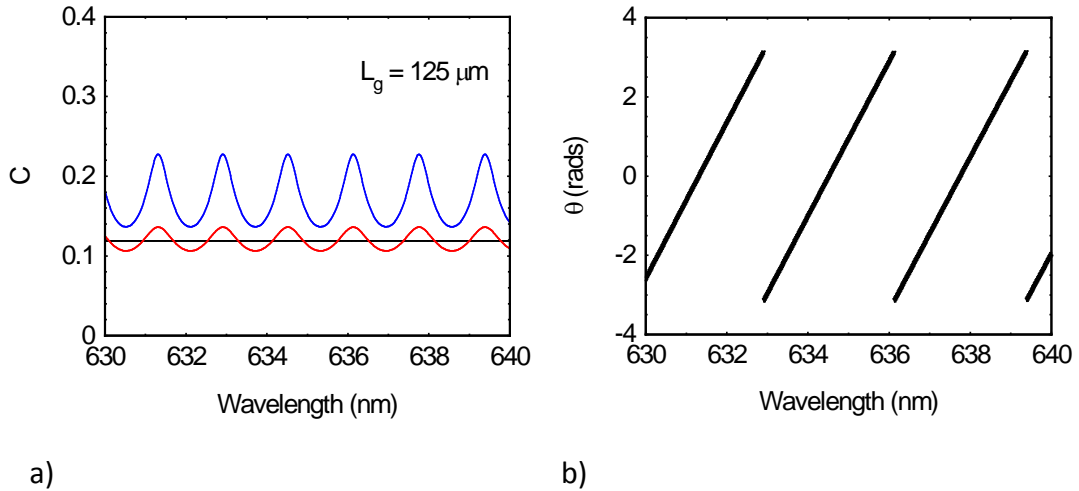


Figure 1.16 a) magnitude of the coupling parameter for a gap length of $L_g = 125 \mu\text{m}$ for facet efficiencies of efficiencies $\eta = 1$ (blue line) and $\eta = 0.5$ (red lines). The black lines represent the first order approximation of the coupling parameter a) magnitude and b) phase shift, for a facet efficiency of $\eta = 0.5$.

Reducing the facet efficiency by a half has the effect of lowering the Q-factor of the gap resonator. This not only reduces the magnitude of the coupling strength but also the amplitude of the periodic spectral response. The higher order round trip reflections and transmissions experience more interactions with the facets, so, as the facet efficiency is reduced they are more and more diminished. In this case, equations 1.16 and 1.17 can be reduced to their first order components with little effect on the magnitude of the gap coupler response (black line in figure 1.16 (a)). The first order reflection, reflected from the inner facet of each laser section, is constant, whereas the first order transmission component, the single pass transmission from one laser to the other, has a phase dependence, see figure 1.16 (b). For larger gap couplers with etched facets therefore, even though the interference effects inside the gap are less influential, there is still a phase condition imposed on the formation of coupled-cavity modes.

1.4.2 Coupled-cavity modes

In order for a coupled-cavity mode to dominate there must be resonant cavity modes available in each of the laser sections with the same wavelength. Furthermore, the wavelengths of these modes must correspond to the in-phase coupling condition imposed by the gap coupler. As was highlighted in the previous section, for larger gap couplers, this can only occur over a narrow band of wavelengths corresponding to the maxima of the coupling parameter response.

With reference to the coupled-cavity schematic illustrated in figure 1.14, a threshold gain condition can be derived for coupled-cavity modes by considering the gain and loss in each of the laser sections and the mutual optical feedback from the gap coupler [6, 7]. Applying the round trip condition that was used to derive the threshold gain condition for the longitudinal modes of the single cavity laser, i.e. at threshold the net round trip amplification of light within the device is approximately equal to one, yields an eigenvalue equation that can be used to calculate the wavelengths and threshold gains for sections 1 and 2 for each of the allowed coupled-cavity modes:

$$(1 - r t_1^2 S_{11}) (1 - r t_2^2 S_{22}) = r^2 t_1^2 t_2^2 S_{12} S_{21} \quad (1.20)$$

where the t_1 and t_2 are transmission coefficients that describe the phase shift and gain (or loss) experienced by an optical mode during a single pass of laser cavities one and two respectively

$$t_m = \exp\left(i \left(\frac{2\pi}{\lambda_0}\right) n_m L_m\right) \exp\left(\frac{g_m}{2} L_m\right) \quad (1.21)$$

where n_m , g_m and L_m are the refractive index, modal gain/loss and length of the m^{th} laser cavity respectively.

In contrast to an ideal single cavity laser, in which the carrier density and refractive index both pin at threshold, in the coupled-cavity device these quantities are not fixed. For a device lasing as a coupled-cavity, the carrier densities in each of the laser sections are linked through their mutual optical coupling. If the current injected into one section is increased, the rate at which photons pass into the second cavity will also increase. As a consequence the rate of stimulated emission in the second cavity goes up which effectively suppresses the gain in that section. In order to meet the net threshold gain condition for the coupled-cavity mode the carrier density in the first section must therefore increase. Because the carrier densities in the laser sections are not pinned, neither are the refractive indices. Consequently, the wavelengths of the laser cavity modes can be tuned with respect to one another, which, for devices with unequal laser cavity lengths, provides a facility for wavelength tuning and mode selectivity, see figure 1.17.

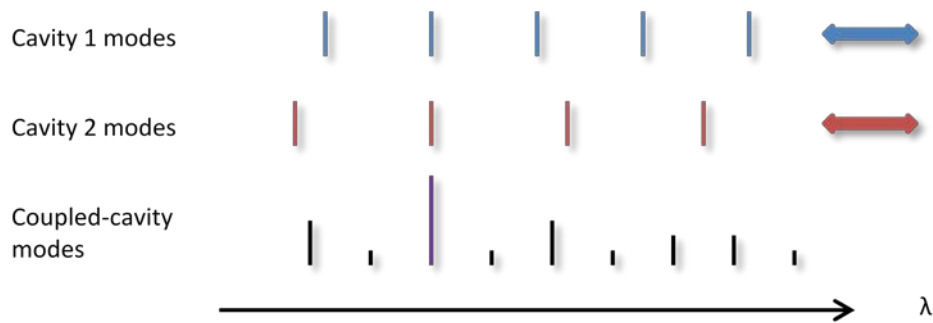


Figure 1.17 Schematic illustration of mode discrimination in a semiconductor coupled-cavity laser with unequal laser cavity lengths.

This mechanism is included in the threshold gain model by assuming a linear relationship between a change in the threshold gain, g_m , and a change in the refractive index:

$$n_m = n_0 - \frac{dn}{dg} \cdot g_m \tag{1.22}$$

where n_0 is the refractive index of the material at transparency and it is assumed that dn/dg is constant and also that the gain has no wavelength dependence.

By substituting equations 1.21 and 1.22 into equation 1.20, the allowed coupled-cavity modes can now be defined by only three parameters: (λ, g_1, g_2) . Starting from a set of known parameter values e.g. the mode solutions for either of the individual laser cavities, the coupled-cavity mode solutions can be mapped out by iteratively solving the real and imaginary parts of the eigenvalue equation simultaneously for the unknown parameters. This technique has been used to plot the laser cavity threshold gain solutions against one another for modes with wavelengths corresponding to a gap coupler maximum. Figure 1.18 demonstrates the mode discrimination mechanism that enables the mode selectivity and wavelength tuning properties of the coupled-cavity device.

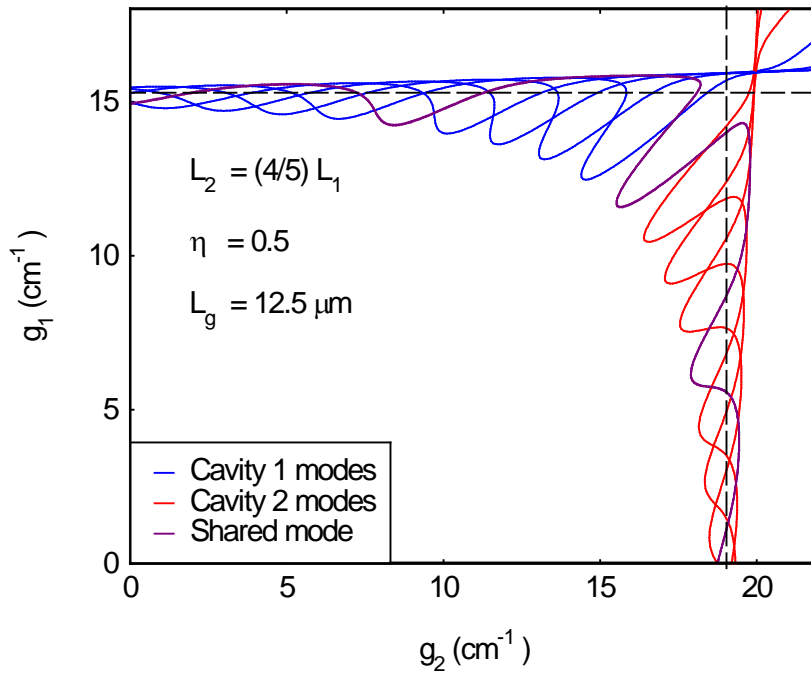


Figure 1.18 Threshold gain map for the coupled-cavity modes originating in cavity 1 (red lines) and cavity 2 (blue lines) for a device with laser cavity lengths: $L_1 = 100 \mu\text{m}$ and $L_2 = 800 \mu\text{m}$. The dashed lines indicate what the threshold values for each of the individual cavities would be in isolation.

As the gain in one section is increased, the individual cavity modes are tuned across one another, which modulates the threshold gain required from the other section. At a given operating point on the gain map, the difference between the net threshold gain loci for each of the coupled-cavity modes, as measured from the

origin, indicates the degree of mode discrimination that occurs at this point. By changing the input current to each of the laser sections, the device will move to a different point on the gain map. If at this point a different mode has the lowest threshold gain requirement then a wavelength shift will occur as the device switches to a different mode - a process known as mode hopping. To demonstrate how the length of the gap coupler affects the formation of coupled-cavity modes, gain maps have been plotted for devices with equal laser cavity length and gap coupler lengths of $L_g = 12.5 \mu\text{m}$ and $L_g = 125 \mu\text{m}$, see figure 1.19.

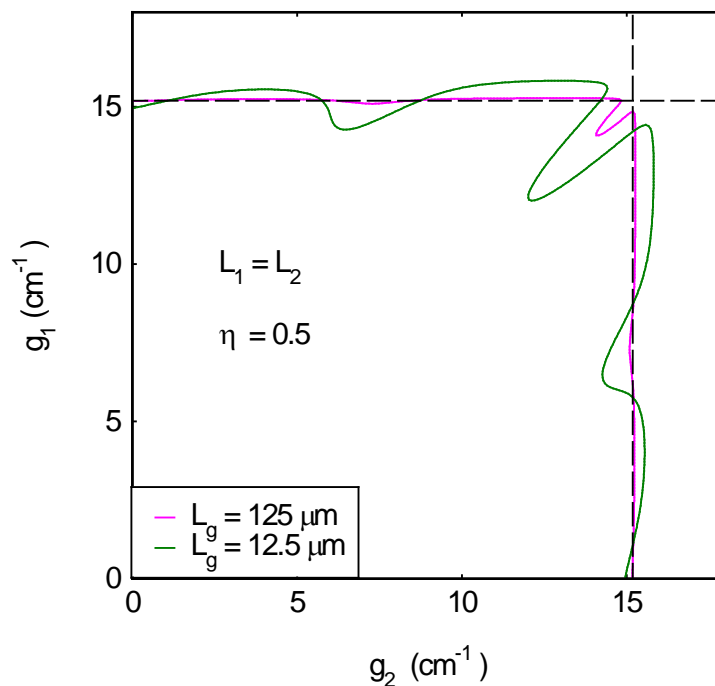


Figure 1.19 Threshold gain maps for devices with equal laser cavity lengths of $L = 1000 \mu\text{m}$ and gap coupler lengths $L_g = 12.5 \mu\text{m}$ (green line) and $L_g = 125 \mu\text{m}$ (pink line).

With equal length laser cavities, each of the allowed modes now follows the same path along the gain map. In this case then, the device offers no mode discrimination at any point. Nevertheless, the interference generated by the individual cavity modes tuning across one another, does modulate the threshold gain requirement. The point at which the threshold gain is equal in each laser corresponds to the point with the lowest net threshold gain requirement. The shorter gap length device has

the lowest net threshold gain requirement at this point, as would be expected due to the greater coupling strength, but an equivalent point also exists for the larger gap coupler. This indicates that even for devices with comparatively weak coupling, coupled-cavity modes can still exist that will lase in preference to the modes of the individual cavities the threshold gains of which are indicated by the dashed lines in figure 1.19. The size of this effect i.e. the difference between the threshold gain requirement of the coupled-cavity modes and those of the individual cavities scales with the length of the laser cavities, see fig 1.20.

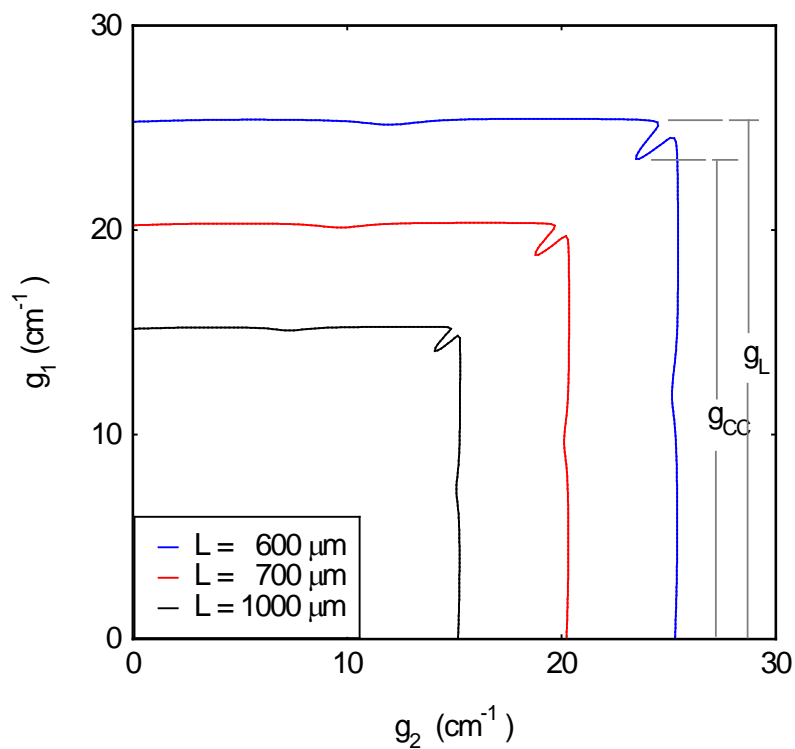


Figure 1.20 Threshold gain maps for equal laser section lengths $L = L_1 = L_2$ each for a gap length $L_g = 125 \mu\text{m}$ demonstrating that the ratio of the lowest threshold gain requirements of the coupled-cavity mode g_{CC} and the individual laser section modes g_L is independent of laser section length L .

1.5 Summary

In summary, this chapter has described the motivation, aims and structure of the thesis. The chapter has also included the background theory relevant to the discussions of experimental techniques and results that are presented in the chapters to follow. A simple threshold gain model has been described and used to model the behaviour of coupled-cavity devices with large etched facet gap couplers. The results of this model have been used to predict that coupled-cavity modes can exist with lower threshold gain requirements than the modes of either of the individual cavities.

References

- [1] A. Radbruch “Flow Cytometry & Cell Sorting”, 2nd Edition, Springer, 2000.
- [2] X. J. Liang, A. Q. Liu, C.S. Lim, T. C. Ayi and P. H. Yap “Determining refractive index of single living cell using an integrated microchip”, *Sensors and Actuators A*, 133, p. 349, 2007.
- [3] P. L Gourley “Biocavity laser for high-speed cell and tumour biology”, *Journal of Physics D: Applied Physics*, 36, p.228, 2003.
- [4] L. A. Coldren and S. W. Corzine, “Diode lasers and photonic integrated circuits”, *Wiley Series in Microwave and Optical Engineering*, 1995.
- [5] G. P. Agrawal and N. K. Dutta “Long-wavelength semiconductor lasers”, *Van Nostrand Reinhold Electrical/Computer Science and Engineering Series*, 1986.
- [6] C. H. Henry and R. F. Kazarinov “Stabilization of Single Frequency Operation of Coupled-Cavity Lasers”, *IEEE Journal of Quantum Electronics* Vol. QE-20, p.733, 1984.
- [7] L. A. Coldren and T. L. Koch “Analysis and Design of Coupled-Cavity Lasers – Part 1: Threshold Gain and design Guidelines”, *IEEE Journal of Quantum Electronics* Vol. 20, No. 6, p.659, 1984
- [8] L. A. Coldren, K. Furuya, B. I. Miller, and J. A. Rentschler “Etched Mirror and Groove-Coupled GaInAsP/InP Laser Devices for Integrated Optics” *IEEE Journal of Quantum Electronics* Vol. QE-18, p.1679, 1982.

Chapter 2:

Device fabrication

2.1 Introduction

One of the primary objectives of this study has been to develop a reliable, reproducible method for the fabrication of a novel micro-fluidic coupled-cavity (MFCC) laser device. Conceptually this device can be thought of as a “lab on an optically active chip”, that is, micro-fluidics are integrated into an optically active semiconductor substrate rather than the more typical approach of embedding lasers/detectors into a micro-fluidic chip on a glass or silicon substrate. This chapter describes the design and fabrication work that has been undertaken during the project to develop a prototype device that forms the basis of the experimental work presented in the later chapters.

To provide some context for the more detailed description that follows, section 2.2 establishes both the device design concept and its requisite functionality. Section 2.3 provides a brief description of the AlGaInP quantum well material that has been used during the project and from which all experimental devices have been fabricated. Section 2.4 presents the MFCC device design and a brief description of the key design features. The main content of the chapter is presented in section 2.5 which includes a detailed description of the process flow that has been developed to fabricate the prototype device.

2.2 Design concept

The purpose of the MFCC device is to provide an experimental platform with which to study the influence of fluids, and fluid borne particles, on the coupling between paired in-plane laser cavities. The functionality that this implies inevitably places certain constraints on the device configuration and, therefore, on its design.

Although these constraints are somewhat subjective, they are presented here as they constitute a set of self-imposed guidelines by which the device has been designed. These design criteria are illustrated in figure 2.1: an idealized device configuration.

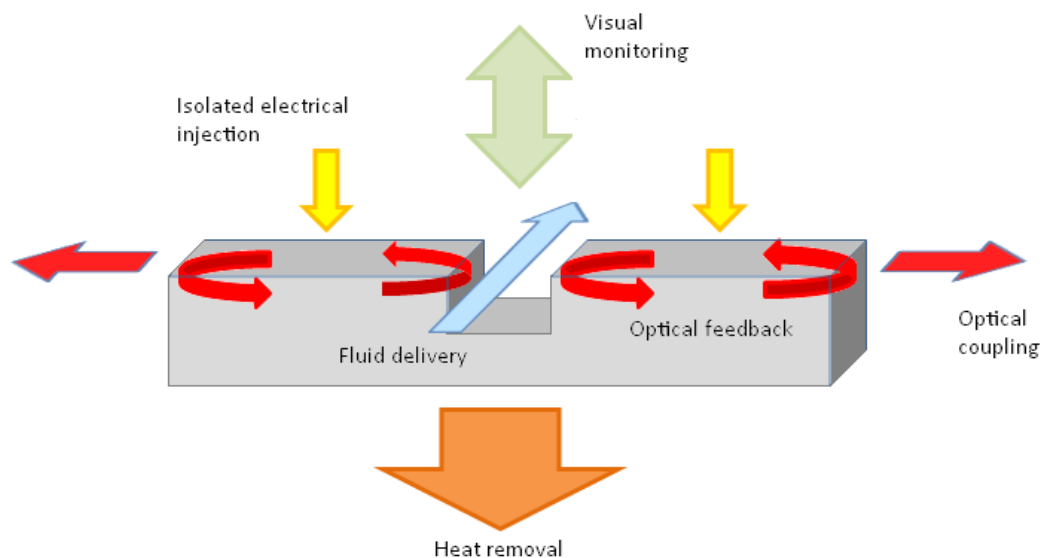


Figure 2.1 an ideal device configuration and requisite functionality.

Fluid delivery: One of the main requirements of the device is a facility to deliver a throughput of fluid at the interrogation region between the two laser sections. This may be from a reservoir incorporated somewhere on the chip or via an interface to the outside world.

Optical feedback: In order to achieve laser action in each of the separate laser sections, sufficient optical feedback must be generated at each of the cavity interfaces. This requires the fabrication of efficient laser facets.

Electrical isolation: So that each of the separate laser sections can be independently electrically biased, the sections need to be electrically isolated from one another and also from the fluid passing through the interrogation region.

Optical coupling: information from the analyte is encoded within the light output from the device. Access to this information therefore requires unencumbered coupling of the light output to external optical elements such as: optical fibers, spectrometers and lenses.

Heat removal: semiconductor lasers are prone to self-heating, it is necessary therefore to include a method of removing heat from the device in order to regulate its temperature.

Visual monitoring: A facility for independent monitoring of the interrogation region of the device via a microscope or camera is necessary to allow the device response to be correlated to individual interaction events (at least during the research phase).

2.3 Quantum well material

The devices used throughout this study have all been fabricated from a single quantum well (SQW) material of GaInP/AlGaInP on an n-type GaAs substrate emitting at around 635 nm. The wafer was commercially grown by IQE using metal-organic chemical vapour deposition (MOCVD). The exact layer structure of the wafer is proprietary information so cannot be included.

2.4 Device design

The device design that is presented in figure 2.2 has been developed to provide the functionality discussed above. The design is comprised of two key components, a monolithic coupled-cavity laser array and an integrated micro-fluidic delivery system.

An array of ten 50 μm stripe laser pairs are configured about a 20 μm deep channel patterned into the surface of a semiconductor crystal. The channel forms both the inner facets of the individual laser sections, as well as the foundation for the fluid delivery system. The rationale for the arrayed configuration of lasers is two-fold. Firstly, it provides a capacity for multiple measurements on a single chip. And secondly, because the fluid delivery system creates large regions at each end of the device that do not perform any active photonic function, increasing the number of lasers on each chip makes for a more efficient use of the semiconductor material.

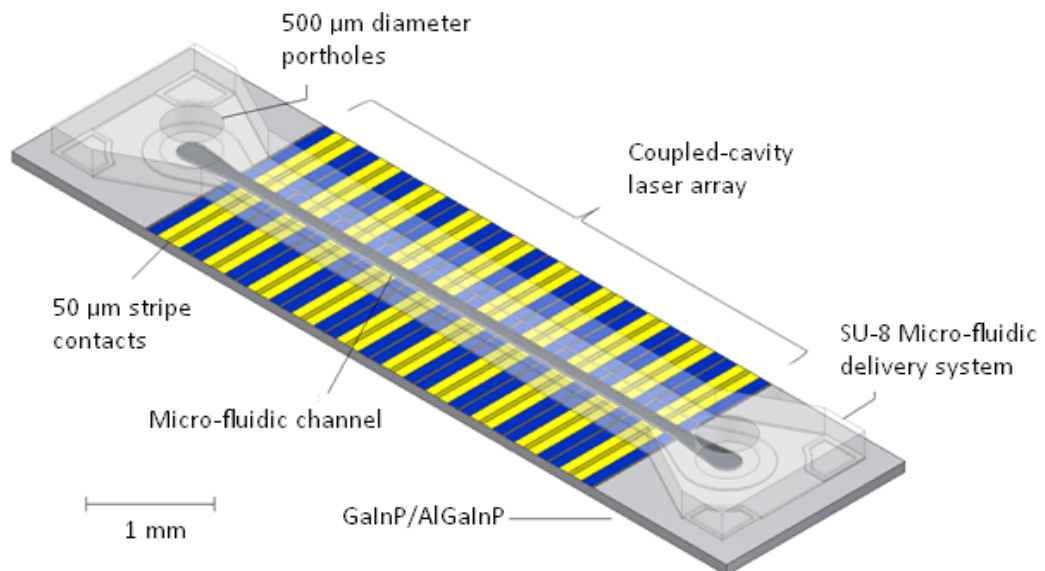


Figure 2.2 is a scaled illustration of an 8 x 2 mm MFCC chip showing its key components the coupled-cavity laser array and the integrated micro-fluidic delivery system.

The second component of the design is a multilayer micro-fluidic delivery system (the transparent “bow tie” shaped structure that can be seen partially covering the upper surface of the chip in figure 2.2). Apart from its main purpose of delivering fluids to the interrogation region, this component performs several other important functions. A 20 μm thick layer of SU-8 epoxy effectively builds the channel up half way out of the surface of the semiconductor, ensuring that the central axis of the channel intersects the optical axis of the coupled lasers, see the cross sectional cut through depicted in figure 2.3. Because SU-8 is transparent and electrically insulating, it also serves to isolate the fluid inside the channel from the laser contacts on either side without absorbing the laser light passing through it.

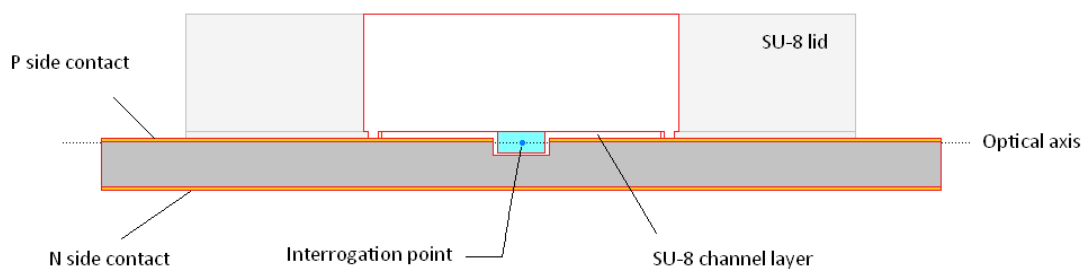


Figure 2.3 A device cross section showing a 100 x 40 μm micro-fluidic channel. The optical axis of the lasers intersects the central axis of the channel at the interrogation point.

A 200 μm thick SU-8 lid is then placed on top of the channel sealing it from all but the 500 μm diameter portholes positioned at each end. The portholes provide connection points for the input and output of fluids to the channel and, because the lid is transparent, interactions that occur inside the channel can be optically monitored.

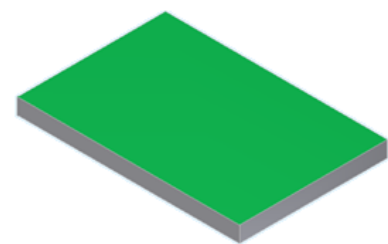
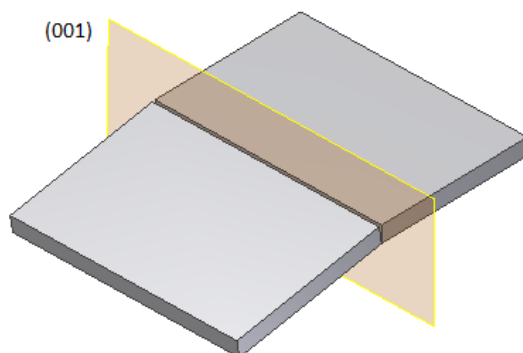
2.5 Fabrication

2.5.1 Etched laser facets

The monolithic integration of the laser sections called for in the MFCC design requires that the inner facets of the laser sections must be formed by etching material out from the surface of the semiconductor chip. Various etching techniques have been used for this purpose wet chemical etching [1], reactive ion etching [2], chemically assisted ion beam etching [3] and focused ion beam milling [4]. In this work the facets have been etched exclusively using an inductively coupled plasma (ICP) etching process, the details of which are described below. The aim is to produce laser facets that are vertical, nearly atomically flat and etched through the vertical extent of the epitaxial growth layers of the semiconductor crystal into the GaAs substrate.

1) Sample preparation: a rectangular 6 x 9 mm sample is cleaved from an AlGaInP semiconductor wafer. The longer dimension is cleaved along the (001) crystallographic plane in order to provide a reference edge for the alignment of the etched facet and the laser contact stripe patterns. Cleave debris and other contaminants are then removed from the surface of the sample with a multi-step solvent clean. This sample will eventually yield two MFCC devices.

Step1. Sample preparation



Step 2. Etch mask deposition

Figure 2.4 A reference edge is provided by cleaving the sample along the (001) crystal plane. After cleaning, a 300 nm SiO₂ mask layer is deposited onto the upper surface of the sample.

2) Etch mask preparation: Ni, Cr and SiO₂ were all tested for use as plasma etch masks. Both Ni and Cr were found to have a better selectivity than SiO₂ but, they were also found to partially anneal into the surface of the sample during the high temperature plasma etching process, making their subsequent removal difficult and reducing the quality of electrical contacts that could be achieved. SiO₂ on the other hand is easily removed using a dilute HF acid etch and the left over SiO₂ can be used as an insulating layer for the 50 μm stripe lasers contacts eliminating the need for a second oxide deposition. A 300 nm layer of SiO₂ is blanket deposited on to the upper surface of the sample using an Edwards electron beam evaporator. Moisture trapped in the SiO₂ layer is then removed by heating the sample to 400 °C for 30 minutes in an inert nitrogen atmosphere.

3) Etch mask patterning: a 200 nm thick layer of 4% 950K Polymethyl-methacrylate (PMMA) positive resist is spin coated on top of the SiO₂ mask layer. The facet pattern is then transferred into the resist by direct write exposure using a Raith 50 electron beam lithography (EBL) system. Exposure to the electron beam breaks the long polymer chains of the resist into smaller fragments which, when developed in a methyl isobutyl ketone : iso propyl alcohol (MIBK:IPA) solution, are more easily dissolved than the unexposed regions. The high resolution and sharp contrast that can be achieved with this system leaves a pattern with a relatively sharp edge and near vertical step profile in the resist. This profile is very important as any deviation from vertical will ultimately be transferred into the semiconductor etch, affecting the efficiency of the resulting facets.

Ni etch masks were also prepared using the image reversal resist AZ5214E in a photolithography/lift-off process, however, EBL was found to produce qualitatively better etch profiles than masks patterned in this way. A major disadvantage however of the EBL system is that the sequential nature of the pattern generation limits the size of the pattern that can be written before drift in the electron beam current causes the exposure dose to vary beyond tolerance. This ultimately limits the number of devices that can be patterned onto each sample using this technique.

4) Plasma etching: the pattern in the PMMA layer is transferred into the SiO₂ etch mask using a room temperature C₄F₈/Ar RIE plasma etching process. The remaining PMMA is then removed using acetone and the surface is de-contaminated with an oxygen plasma etch. The SiO₂ mask is then used to transfer the pattern once again, this time into the semiconductor crystal using a high temperature (200 °C) Ar /Cl₂ ICP plasma etch, see figure 2.5.

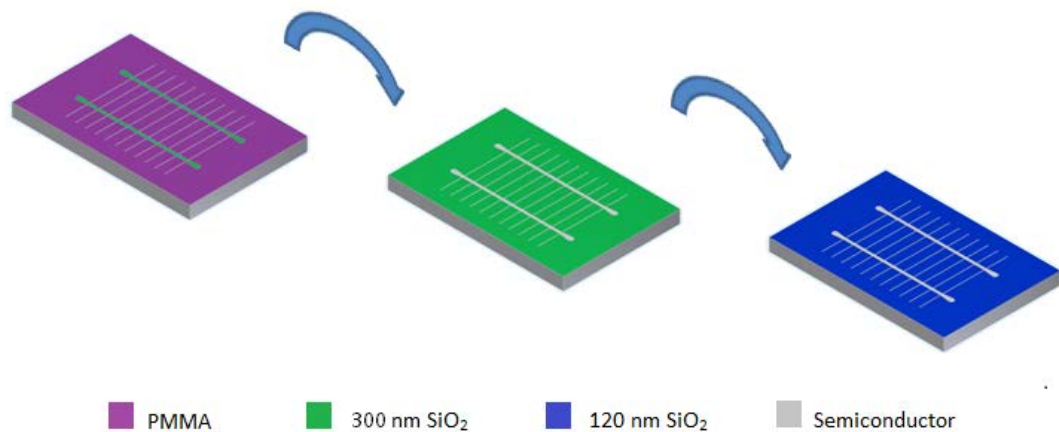


Figure 2.5 the facet pattern is transferred from the PMMA resist mask to the SiO₂ mask and then to the semiconductor in a two stage plasma etching process.

Figure 2.6 (a) is a scanning electron microscope (SEM) image of a 20 μm wide etched channel with near-vertical side walls, etched to a depth of 2.5 μm i.e. all the way through the epitaxial layers and into the GaAs substrate as required.

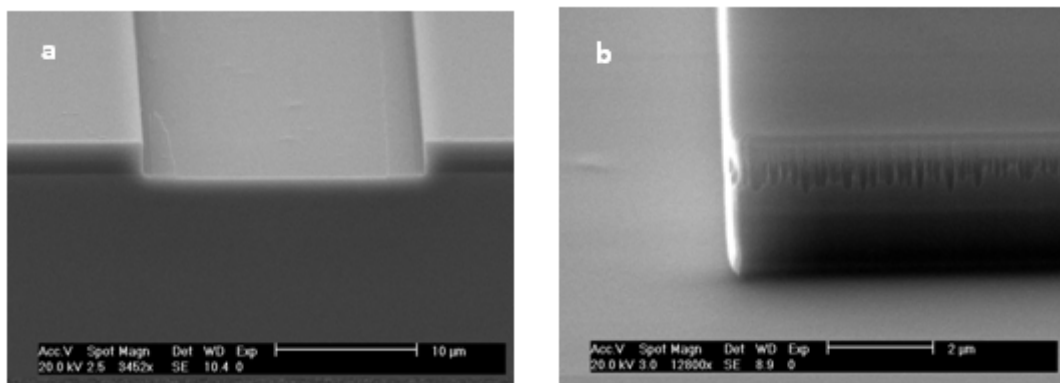


Figure 2.6 SEM images of **a)** A near-vertical etch profile that extends through the epitaxial growth layers and into the GaAs substrate. **b)** Evidence of faceting damage along the upper edge of the etched feature along with vertical striations that extend all the way to the bottom of the feature.

Figure 2.6 (b) reveals vertical striations on the surface of the etched facet extending down from the top to the bottom of the facet. The lateral pitch of these features corresponds roughly to the 100 nm EBL step size used during the patterning of the PMMA etch mask. It is probable that the un-even pattern edge created by the step wise nature of the EBL exposure procedure is transferred to the semiconductor etch resulting in these vertical features.

Figure 2.6 (b) also shows evidence of the well known phenomenon of “faceting” on the leading edge of the etched feature. Faceting results from the physical sputtering of mask material during the etching process. The amount of mask material that is removed per incident plasma ion is a function of the angle at which the ions strike the mask [5]. Non-vertical or rounded etch mask profiles can cause an angled plane to form at the leading edge of the mask during the etching process, see figure 2.7 (a). As the etch progresses the plane is reinforced and propagates through the mask material, as in figure 2.7 (b). If the mask layer is not sufficiently thick, then the plane will eventually expose the substrate to the plasma, allowing the leading edge of the semiconductor feature to begin etching, see figure 2.7 (c). For SiO₂ mask thicknesses greater than 300 nm the faceting damage was found to be limited to regions where it does not interfere with the laser cavity modes.

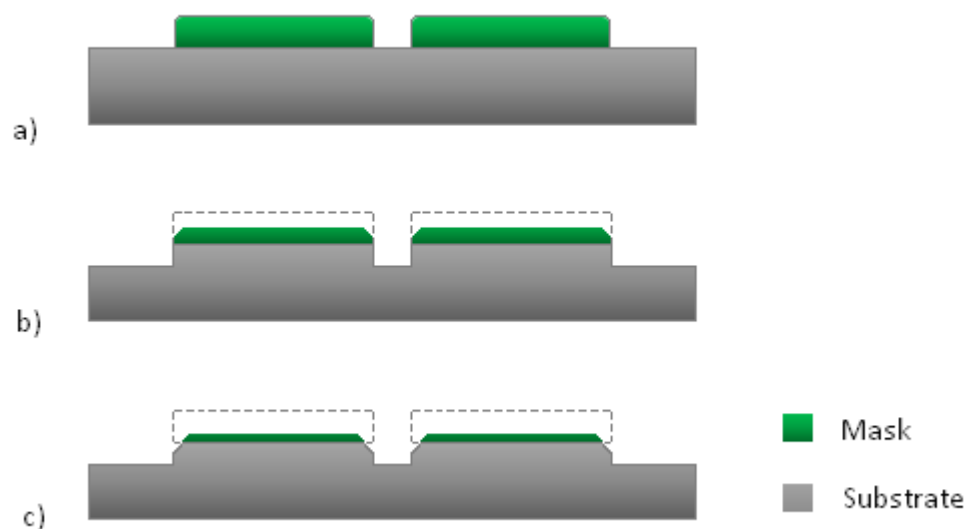


Figure 2.7 illustration of how rounded mask edges lead to faceting damage of etched features.

2.5.2 Electrical contacts

To provide electrical injection of the individual laser sections of the device, metal contacts are patterned on to both the p and n sides of the sample.

P side contacts: a 1.5 μm layer of Shipley S1813 S15 photo-resist is spin coated on to the remaining SiO_2 mask layer. The sample is exposed using a Karl Suss MJB3 UV400 mask aligner and a photo-mask[†] of the desired contact stripe pattern. The non-planar surface created by plasma etching causes the resist to thin at the edges of the etched features. To avoid loss of pattern definition due to over exposure of the thinner resist in these areas, the contact stripes are patterned 5 μm short of the facet edges. On development, the sample is left with resist covering all but the contact stripe pattern. The resist is hard baked and the sample is etched in a dilute HF acid removing all of the SiO_2 from the stripe pattern and exposing the P-GaAs cap layer of the semiconductor below.

The photo-resist is then stripped away and a AuZn metal contact is blanket deposited onto the upper surface of the sample by thermal evaporation. A second photolithography step has to be performed to pattern the metal into an array of contact pads using an I_2KI solution to back etch the AuZn between sections, see figure 2.8.

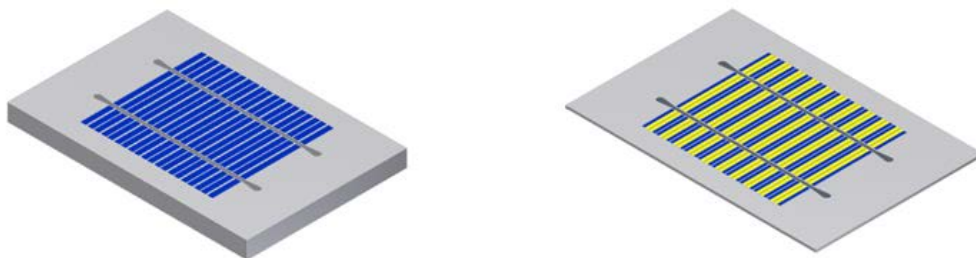


Figure 2.8 The SiO_2 insulator layer is patterned with an array of 50 μm stripes. AuZn contact pads are deposited and patterned. The sample is lapped at this point to a thickness of (100 ± 5) μm .

[†]Each of the photomasks used in this work were designed and fabricated in house by the author using EBL to pattern a 100 nm layers of Cr deposited on a 37mm² soda lime glass plates.

The photo-resist mask is once again stripped and the sample is annealed in a Jetfirst rapid thermal annealer (RTA) where the Zn atoms in the metal contact layer inter-diffuse with Ga atoms in the P-GaAs semiconductor cap forming a low resistance Ohmic contact.

N side contact: as it is common to all sections the n side contact does not require any patterning. However, before the metal contact can be deposited onto the N-GaAs substrate, the sample is first thinned to facilitate cleaving of the individual devices from the sample at a later stage. The sample is lapped from 650 μm to around 100 μm using a Buehler lapping machine and an AuGe/Ni/Au metal contact system is thermally evaporated on to the back surface. As with the top contact, the sample is annealed in the RTA which promotes the inter-diffusion of the Ge and Ga atoms.

2.5.3 Deep-etched channels

In order to provide a foundation for the integrated micro-fluidics, a 15 μm deep channel needs to be etched into the surface of the semiconductor between the etched facets of the coupled-cavity lasers. Unlike the etched facet side wall profile the verticality of this feature is not crucial as the micro-fluidic channel walls are re-defined inside this foundation channel at a later point. An isotropic wet etch is adequate to achieve the required depth and avoids the need for further exposure to a potentially damaging plasma etch.

A photo resist mask is patterned onto the sample leaving a 115 μm wide channel pattern inside the etched facet pattern. The sample is then etched for roughly 30 minutes in a dilute $\text{NH}_3/\text{H}_2\text{O}_2$ solution to a depth of 15 μm . The depth that can be achieved with this method is ultimately limited by the quality of the mask adhesion. At around 15 μm depth the photo resist mask typically begins to de-laminate exposing the etched facets to the etchant which can undercut the metal contacts and roughen the etched laser facets.

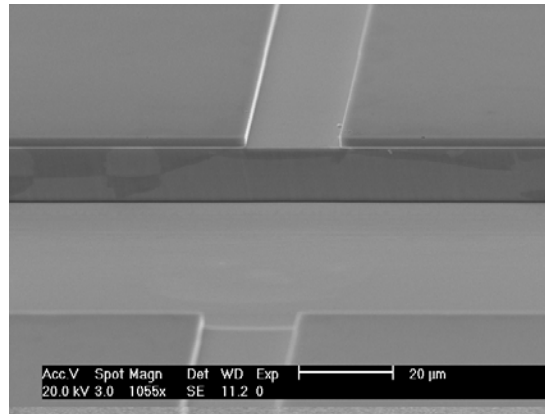


Figure 2.9 SEM image of a 15 μm deep foundation channel running left to right. The 2.5 μm deep stripe that can be seen running across the channel from top to bottom is a laser section isolation break.

2.5.4 Integrated SU-8 Micro-fluidics

The integrated micro-fluidic delivery system of the device has been fabricated using multiple layers of the photosensitive epoxy SU-8. SU-8 has many desirable properties for micro-fluidics applications; it is biocompatible, chemical resistant, electrically insulating and transparent at visible wavelengths. Furthermore, single layers of SU-8 can be patterned into near vertical features up to 200 μm thick using standard photolithographic techniques. SU-8 also has some less desirable properties however. It is hydrophobic, which increases the amount of pressure required to generate a fluid flow through the channel and it does not adhere well to many commonly used micro processing materials [6]. The adhesion of SU-8 to both Au and SiO₂, the two materials covering the majority of the surface of the MFCC device, is particularly poor. Thinner formulations of SU-8, however, were found to provide better adhesion than thicker ones. Also, hard baking the epoxy after developing was found to significantly improve its adhesion to most surfaces.

To overcome this inherent adhesion problem, a thin 2 μm adhesion layer of SU-8 2002 is spun onto the sample and patterned using photolithography. This layer not only serves as an adhesion promoter for subsequent layers, but also coats the base of the channel sealing it from the GaAs substrate. The walls of the channel are then re-defined in SU-8 and its height is increased by spinning on and patterning a 20 μm

thick layer of SU-8 2025, see figure 2.10a. Both layers are then hard baked at 180°C for 20 minutes to improve adhesion. The hard bake also improves the chemical resistance of the epoxy by ensuring that it is fully cross-linked and is therefore no longer soluble. This step is essential as it is necessary to expose the sample to boiling trichloroethylene when the individual devices are cleaved from the sample in a later step.

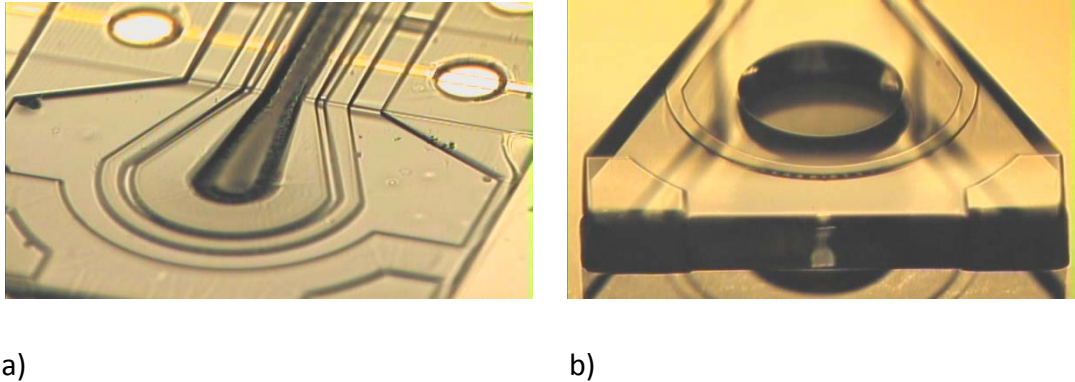


Figure 2.10 a) A 20 µm thick SU-8 channel layer patterned onto the laser array after post lithography bake. b) Near vertical side walls of a 200 µm thick SU-8 lid suitable for capping the structure shown in (a), patterned with 18 µm thick alignment guides and showing one of the fluid delivery inlet holes.

SU-8 is susceptible to a phenomenon known as T-topping [7] which occurs due to absorption of the mercury lamp emission lines below 350 nm. The upper portion of the epoxy becomes over exposed forming a ‘crust’ at the surface which results in a T shaped feature profile. To achieve the near vertical feature profiles that can be seen in figure 2.10 (b) it was necessary to reduce the T-topping effect by exposing the sample through a long pass Schott glass filter with a 360 nm cut-off wavelength.

The SU-8 channel lids are fabricated on a sacrificial glass substrate in a two layer exposure. Firstly, the lid pattern is defined in a 200 µm thick layer of SU-8 2100. Then, before this layer is developed a second 18 µm thick layer of SU-8 2025 is patterned on top to form the alignment guides that can be seen in figure 2.10b. These alignment guides are designed to fit into slots patterned into the 20 µm deep channel layer, see figure 2.10 (a). After development, the lids are carefully removed from the substrate using a scalpel. If more encouragement is needed, stubborn lids can be delaminated by thermal shock in a bath of liquid nitrogen.

2.5.5 Cleaving and packaging

Before the SU-8 lids can be stuck to the channel pattern, cleaves are made along the (001) crystallographic plane yielding the individual devices from the sample and creating the outer facets of each device at the same time. Cleaving along the crystal plane optimizes the reflectivity efficiency of the cleaved facets and ensures that they are parallel to the inner etched facets that have already been aligned to this plane. The samples are then mounted into a bespoke package (see figure 2.11) using silver loaded epoxy to make an electrical connection from the bottom contact to the laser header and then to the heat sink. Electrical connections are made to the individual laser sections using a K&S model 4523 wire bonder to bond 25 μm diameter Al wires from the AuZn top contacts to a printed circuit package that houses macroscopic electrical connectors. The lids are then aligned and stuck into place with additional SU-8 as a bonding agent.

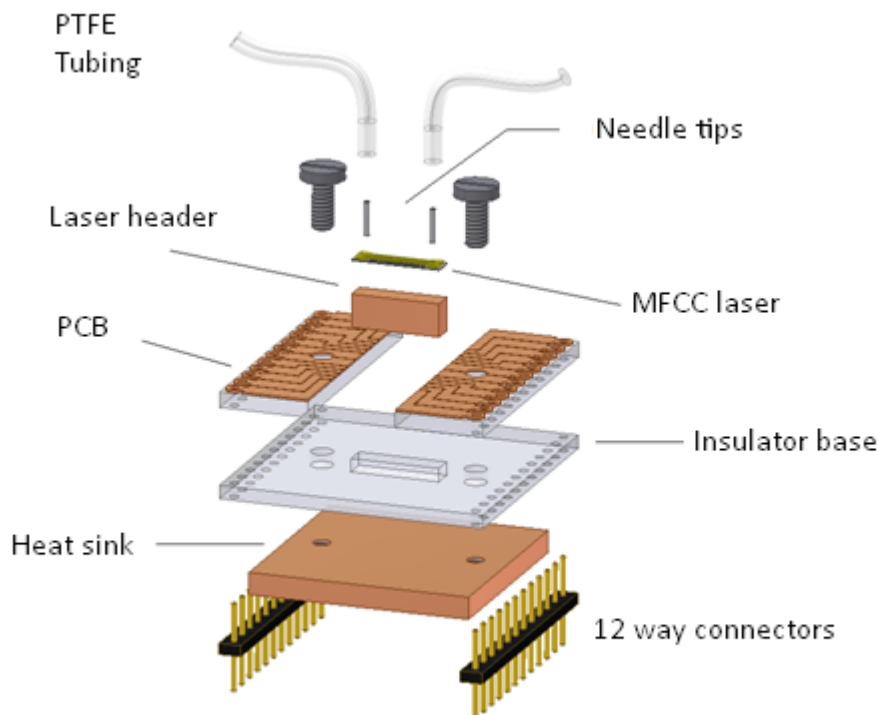
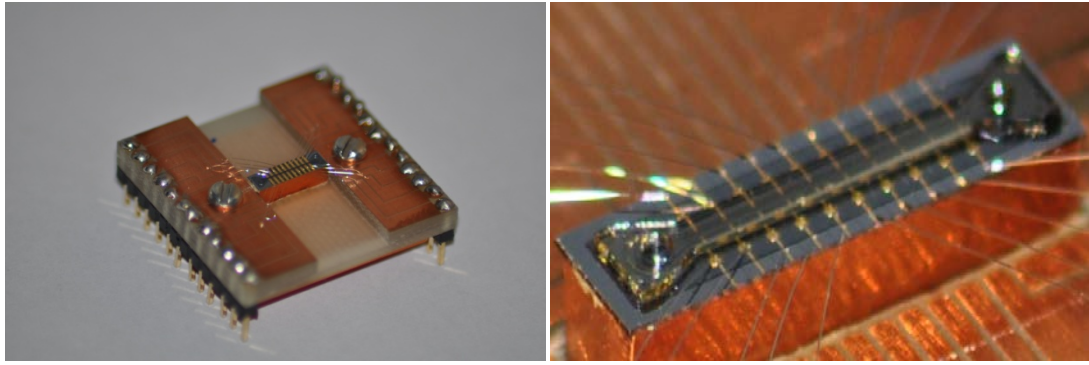


Figure 2.11 An exploded diagram of the micro-fluidic coupled-cavity device, contact arrangement, and packaging.



a)

b)

Figure 2.12 a) A packaged device showing the completed integrated chip concept, b) A close up of a packaged device with an SU-8 lid attached and an integrated micro-fluidic channel defined.

The packaged device pictured in figure 2.12 (a) represents the most advanced version of the MFCC device that I have produced to date. The device features a fully operational coupled-cavity laser array and an SU-8 micro-fluidic channel. However, due to time constraints, the SU-8 lid that completes the micro-fluidic delivery system has not yet been attached. Figure 2.12 (b) features an earlier iteration of the device that does include the micro-fluidic lid, however, due to the poor quality of the top contacts, none of the laser sections of this device were operational. Nevertheless, test samples of the SU-8 micro-fluidic delivery system, patterned on glass substrates, have been used to generate a fluid flow (needle tips inserted into the lid portholes were used to make the micro-fluidic inter-connects necessary to connect to a manual syringe via short lengths of PTFE micro-bore tubing). In principle, therefore, once a lid has been attached to the device pictured in figure 2.12 (a), there is no reason to believe that the fluid delivery system will not work as intended.

2.6 Summary

This chapter has described the design concept and design rationale for the microfluidic coupled-cavity device along with the details of the fabrication process flow that has been developed to create a working prototype. This discussion has highlighted some of the key processing issues that were encountered. Critically these have been: the use of SiO_2 etch mask to improve the quality of the p side Ohmic contacts, minimization of faceting damage by using mask thicknesses of no less than 300 nm and improvement of the SU-8 adhesion by using a thin SU-8 adhesion layer with a post development hard bake.

References

- [1] J. L. Merz, R. A. Logan and A. M. Sergent "GaAs integrated optical circuits by wet chemical etching", IEEE Journal of Quantum Electronics, Vol. QE-15, No. 2, p.72, 1979.
- [2] L. A. Coldren, K. Iga, B. I. Miller and J. A. Rentschler "GaInAsP/InP stripe-geometry laser with a reactive-ion-etched facet" Applied Physics Letters 37(8) p. 681, 1980.
- [3] S. J. Cran-McGreehin, K. Dholakia and T. F. Krauss "Monolithic integration of microfluidic channels and semiconductor lasers" Optics Express Vol. 14, No. 17, p. 7723, 2006.
- [4] I. M. Ross, W. H. Ng, L. R. Wilson, I. J. Luxmoore, J. W. Cockburn, A. Krysa, A. G. Cullis and J. S. Roberts "Fabrication of novel quantum cascade lasers using focused ion beam (FIB) processing" Journal of physics: conference series 26, p. 215, 2006.
- [5] J. L. Vossen "The preparation of substrates for film deposition using glow discharge techniques" Journal of Physics E: Scientific Instrumentation, Vol. 12, p. 159, 1979.
- [6] M. Nordström, A. Johansson, E. S. Noguérón, B. Clausen, M. Calleja and A. Boisen "Investigation of the bond strength between the photo-sensitive polymer SU-8 and gold" Microelectronic Engineering 78-79, p. 152, 2005.
- [7] S. J. Lee, W. Shi, P. Maciel, and S. W. Cha, "Top-edge profile control for SU-8 photoresist," in Proceedings of the 15th Biennial University/Government/Industry Microelectronics Symposium, p. 389, 2003.

Chapter 3:

Characterisation of etched laser facets

3.1 Introduction

While the verticality of the etched laser facets described in chapter 2 is comparable to that which can be obtained by cleaving, the faceting and patterning effects inherent in this particular fabrication process result in a considerable roughening of the etched facet surface. Theoretical modelling of light reflected from rough laser facets indicates that surface features with dimensions less than $\lambda/10$ can cause a significant reduction in facet reflectivity [1, 2], where λ here is the wavelength of light inside the semiconductor material. Experimentally, the reflectivity of etched facets can be measured by comparing either: the external differential efficiency [3] or the threshold current density [4] of lasers with cleaved facets to those of lasers with at least one etched facet.

This chapter describes how the relationship between facet reflectivity and the threshold gain of a laser, as described by equation 1.11, has been used to quantify etched facet efficiency - defined here as the ratio of the reflectivity of an etched facet to that of a cleaved facet. The threshold current densities of lasers with two cleaved facets (C-C) and with one cleaved and one etched facet (C-E) have been extracted from light-current measurements for each of these devices. A corresponding threshold gain value has been calculated using net modal gain-current density data measured for a similar device using the multi-section technique [5] (described in section 3.2).

Ion bombardment sustained during the plasma etching process can damage a semiconductor crystal by introducing electron traps [6]. These traps serve to increase the non-radiative recombination rate of charge carriers inside the crystal, altering the gain – current characteristics of the material. Etched facet lasers that have incurred this type of damage will exhibit higher threshold current values as a result. This effect could be interpreted as a reduction in facet efficiency which is also manifest as a higher threshold current. To account for this, the devices used for gain characterisation have been subjected to the same plasma etching conditions as the laser devices that have been used to measure threshold current density. Any damage caused by ion bombardment should therefore be common to both types of device.

The results of this chapter have been organised into three distinct sections. Section 3.2 presents the multi-section results for net modal gain and absorption spectra as a function of current density for an AlGaInP device. In section 3.3, the etched facet efficiency is calculated by comparing the measured threshold current densities of both the C-C and C-E lasers with the multi-section gain data of section 3.2. In Section 3.4 a simple phase broadening model [2] has been adapted and used to numerically calculate a theoretical value for etched facet efficiency using atomic force microscopy (AFM) measurements of etched facet surface roughness.

3.2 Multi-section technique

The multi-section gain characterisation technique is a method of analysing the single-pass amplified spontaneous emission (ASE) of an edge-emitting semiconductor device to extract its modal gain, modal absorption and unamplified spontaneous emission spectra. Analysis of the unamplified spontaneous emission is not necessary for the purpose of this work so has been omitted.

3.2.1 Multi-section device

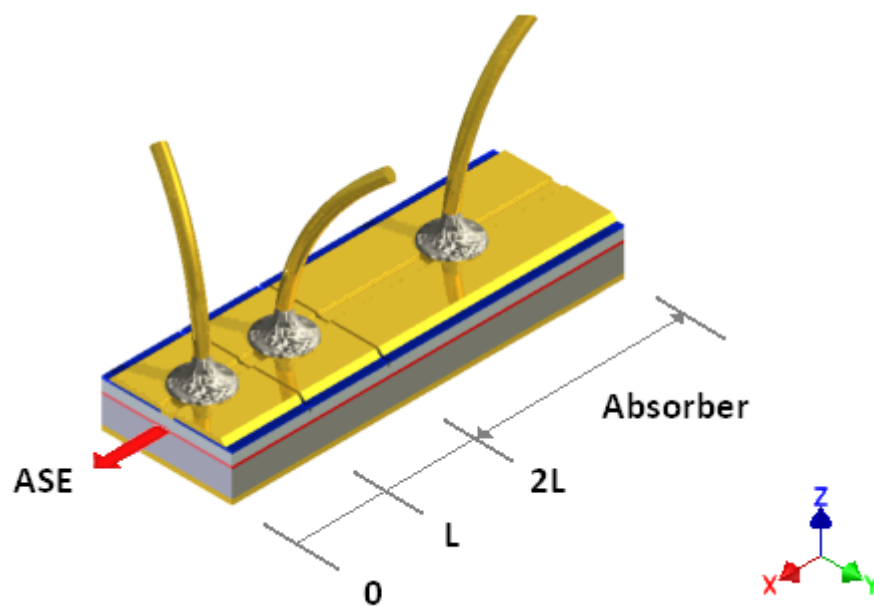


Figure 3.1 is a schematic illustration of a 50 μm stripe multi-section device (not to scale).

Figure 3.1 is a schematic illustration of a multi-section device structure. A 50 μm oxide stripe p-side contact is patterned with two 300 μm long front sections and a 900 μm long rear absorber section. To maximise electrical isolation and minimise current spreading between sections, the contact pattern is etched all the way through the highly conductive p doped GaAs cap of the semiconductor. Independent electrical connections are made to each of the p-side contacts with the n-side contact common to all. The axis of the waveguide is defined here to be in the x-direction with the epitaxial growth direction along the z axis meaning the active quantum well layer lies in the (x – y) plane.

3.2.2 Measurement principle

If the spontaneous emission rate that occurs within the active region of the device is I_{spon} , then the emission from a finite element Δx a distance x from the end of the front facet, results in an amplified spontaneous emission rate at the facet of

$$I(x) = \beta I_{\text{spon}} e^{(G-\alpha_i)x} \Delta x \quad (3.1)$$

where β is the fraction of spontaneous emission that is coupled into the waveguide and G and α_i are the modal gain and internal optical loss respectively. Assuming that I_{spon} is uniform along the axis of the waveguide then the total ASE per unit stripe width resulting from all such elements over a length l is given by

$$I(l) = \int_0^l \beta I_{\text{spon}} e^{(G-\alpha_i)x} dx = \beta I_{\text{spon}} \frac{e^{(G-\alpha_i)l} - 1}{G - \alpha_i} \quad (3.2)$$

Equation 3.2 gives the internal ASE at the facet. The externally observed ASE is given by $I_{\text{meas}}(l) = C.I(l)$ where C is an extraction factor that accounts for transmission across the semiconductor – air boundary, light collection geometry and the overall calibration of the measurement system. An expression for net modal gain can be derived from equation 3.2 by solving it analytically for lengths $l = L$ and $l = 2L$.

$$G - \alpha_i = \frac{1}{L} \ln \left[\frac{I_{\text{meas}}(2L)}{I_{\text{meas}}(L)} - 1 \right] \quad (3.3)$$

Similar arguments can be used to form an expression for net modal absorption ($A + \alpha_i$) where A is a positive value defined as the modal absorption. The total ASE rate at L resulting from emission from section 2 (the region between L to $2L$) is given by equation 3.2. If section 1 (the region between 0 and L) is left un-pumped, the ASE

from section 2 will be absorbed as it passes through. The resulting externally measured ASE will then be given by

$$I_{2(meas)} = C e^{(-A-\alpha_i)L} I_2(L) \quad (3.4)$$

If section 1 is pumped alone, and assuming that the ASE for a given injection current is the same for both sections 1 and 2, the externally observed ASE from section 1 can be expressed in terms of $I_2(L)$ as $I_{1(meas)} = C I_2(L)$. Comparing this expression to equation 3.4 allows the net modal absorption to be expressed as

$$A + \alpha_i = \frac{1}{L} \ln \left[\frac{I_{1(meas)}}{I_{2(meas)}} \right] \quad (3.5)$$

Figure 3.2 is an example of a typical ASE data set for a given current density, in this case 1538 A cm^{-2} . Equations 3.3 and 3.5 can be fitted with these ASE data to give the spectral net modal gain and absorption of a device respectively.

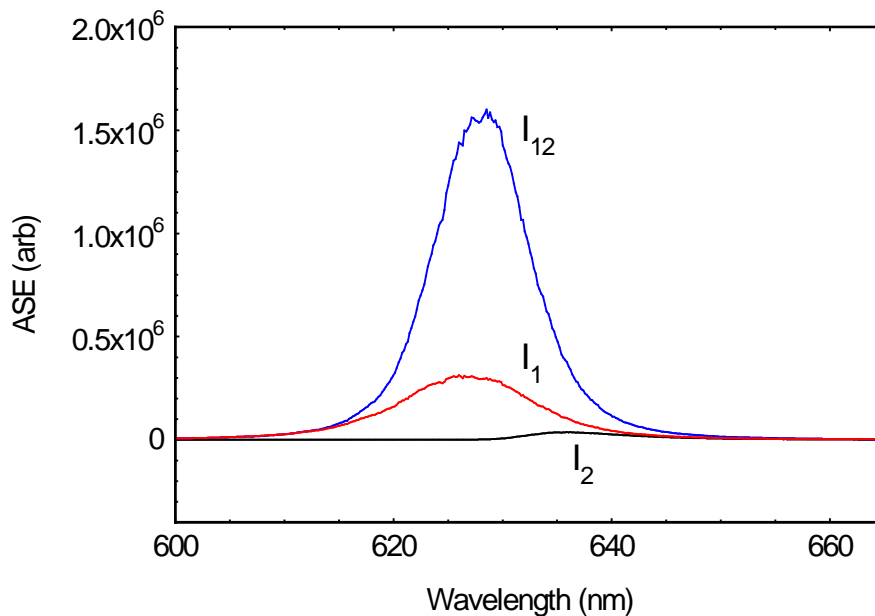


Figure 3.2 Example ASE spectra obtained by pumping; section 1 (red), section 2 (black) and sections 1 and 2 together (blue) at a current density of 1538 A cm^{-2} .

3.2.3 Experimental procedure

The ASE spectra are measured using the experimental set-up illustrated in figure 3.3 which was originally assembled by Dr G. M. Lewis [7]. A multi-section device, such as the one in figure 3.1, is packaged onto a transistor header and mounted on an x-y-z translation stage for optical alignment.

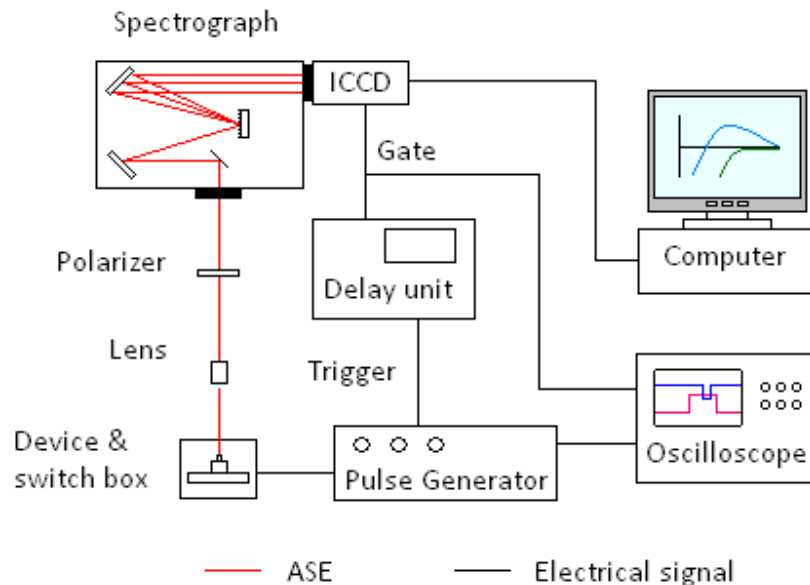


Figure 3.3 Experimental set-up used to measure ASE spectra as a function of current density for multi-section devices.

The device is connected to a pulse generator via a switch box that allows each separate section to be either driven by the pulse generator or grounded (the device is driven with a pulsed current to avoid self-heating). The 900 μm long absorber section at the rear of the device is left grounded throughout the experiment in order to suppress round trip amplification of light that would otherwise invalidate the analytical procedure described above. A microscope objective lens focused on the front facet of the device, collects single-pass ASE generated by forward biasing either, or both, of the front two sections. The light passes through a polarizer and is focused onto the entrance slit of a $\frac{1}{4}$ m spectrograph. The slit allows a finite vertical slice of light from the device to pass into the spectrograph where its spectral components are spatially dispersed onto the photocathode of an Intensified Charge Coupled Device (ICCD) array. The image intensifier of this detector is electronically

shuttered by switching its accelerating voltage on and off to effect a gated measurement of the light by the CCD array. The measurement gate is triggered by the pulse generator via a delay unit ensuring that it is synchronized to the drive frequency (typically no more than 1 KHz). The charge accumulated over an exposure time of 0.2 s is readout from the CCD array and recorded by a computer. Each of the ASE spectra is accumulated over 250 such exposures.

3.2.4 Multi-section results

The net modal gain and absorption for the TM polarisation computed from measured ASE, such as those presented in figure 3.2, for an AlGaInP SQW multi-section device are presented in figure 3.4.

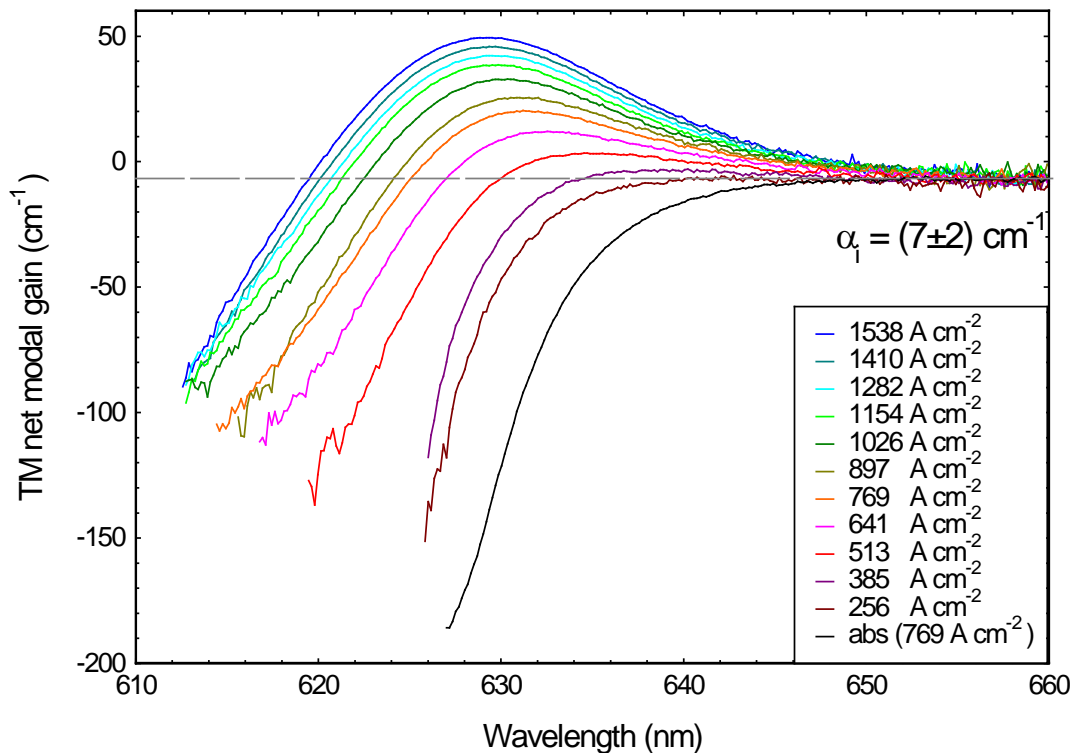


Figure 3.4 TM net modal gain and absorption spectra for the GaInP/AlGaInP SQW multi-section device at a room temperature of $(22 \pm 1)^\circ\text{C}$.

At longer wavelengths the gain and absorption curves tend towards one another at a net modal gain value of $(-7 \pm 2) \text{ cm}^{-1}$. This negative value of net modal gain in a region where the semiconductor is no longer absorbing light, is due to α_i the internal optical loss. The peak wavelength shift to higher energies as the current

density increases is a consequence of band filling and the inhomogeneous broadening of states that occurs due to variations in quantum well width through the sample[8].

The emission wavelength of a steady-state laser will correspond to that of the allowed cavity mode that experiences the most round-trip amplification i.e. the one closest to the peak of the modal gain spectrum for the given threshold current density. In order to make a comparison between the multi-section net modal gain spectra and the threshold current density data therefore, it is appropriate to plot the peak modal gain values from figure 3.4 as a function of current density, see figure 3.5.

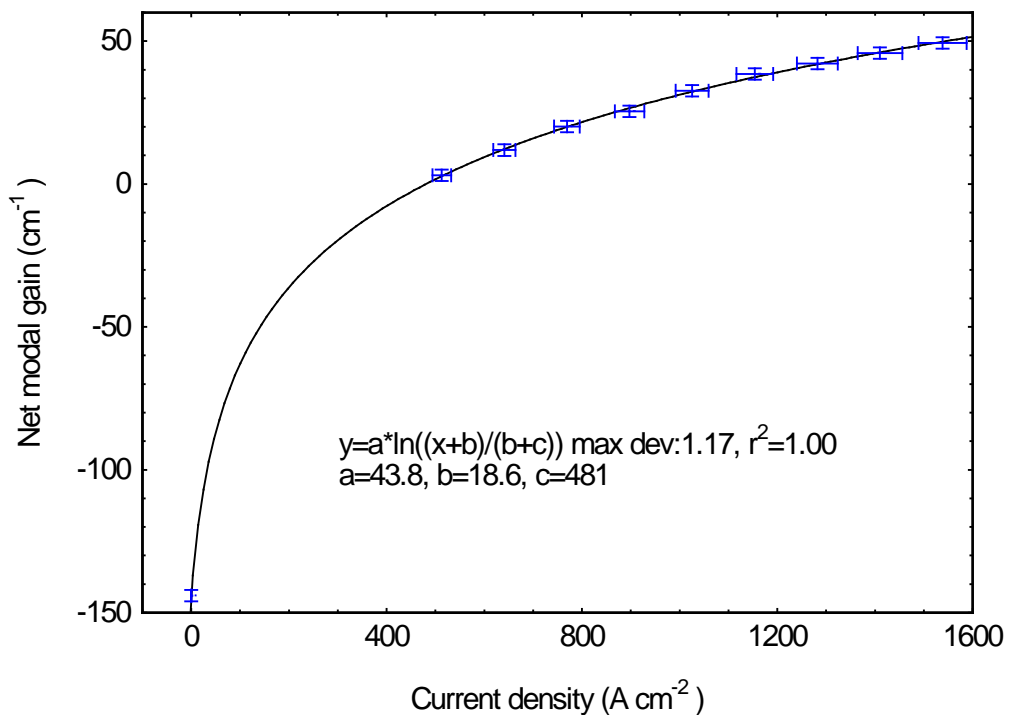


Figure 3.5 Peak net modal gain as a function of current density (blue circles) fitted with a three parameter logarithmic curve fitting function (black line).

The error associated with the net modal gain measurement is dominated by the accuracy with which the input currents can be controlled (± 2 mA) rather than the random noise in the ASE. This error has been quantified by calculating the standard deviation in the absorption spectra as a function of current. The errors quoted with current density result from the combined uncertainties associated with the input current (± 2 mA), the section length (± 2 μm) and the mode width (± 2 μm).

3.3 Cleaved and etched facet laser threshold measurements

The light – current (L-I) characteristics of lasers with two cleaved facets (C-C) and with one cleaved and one etched facet (C-E), have been measured for various cavity lengths. Neglecting the small contribution to the optical mode made by spontaneous emission, the threshold current of a laser can be defined as the point at which the active material provides sufficient optical gain to equal all of the optical losses from the laser cavity. A small increase in the injected current at this point leads to the onset of laser action and a sharp increase in the output of light. Measuring this abrupt change in the gradient of the L-I curve therefore provides a means of determining the threshold current of a laser device.

3.3.1 Laser devices

The C-C and C-E laser devices used to measure threshold currents are illustrated in figure 3.6. Like the multi-section device of figure 3.1 the lasers also have a 50 μm oxide stripe p-side contact, although for these devices the contact is not segmented, and, in the case of the C-E lasers, the p-side contact is patterned 5 μm short of the edge of the etched facet for reasons that were discussed in section 2.4.2. The lasers have been taken from the same wafer as the multi-section devices and exposed to similar processing conditions throughout fabrication.

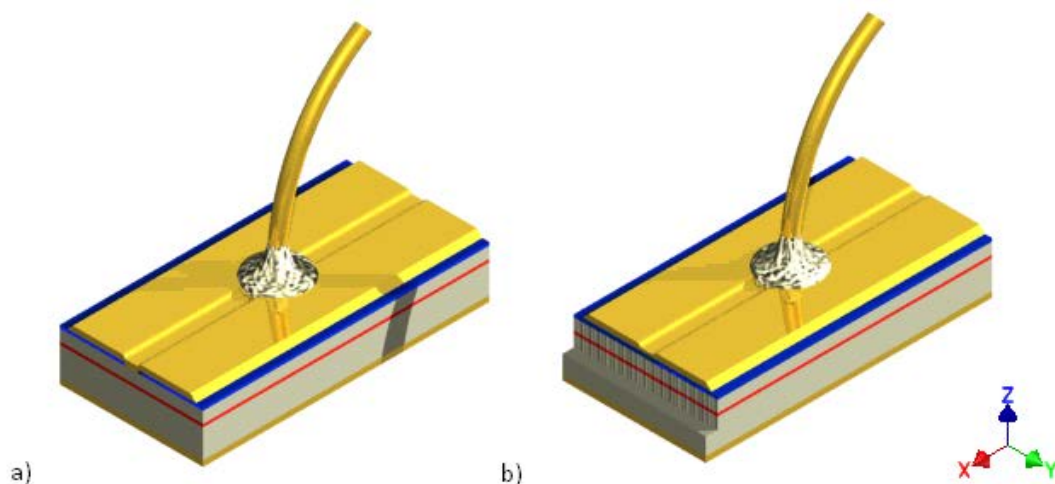


Figure 3.6 is a schematic illustration of a) a cleaved-cleaved facet laser and, b) a cleaved-etched facet laser, (not to scale).

3.3.2 Experimental procedure

The light - current characteristics of the C-C and C-E lasers have been measured using the experimental set up illustrated in fig 3.7, originally assembled by K. Griffiths [9]. A device mounted on a transistor header is aligned to a broad area silicon photo-detector (reverse biased at -10V). A pulse generator is used to apply a current to the device via a computer controlled constant current source. The resulting light, current and voltage are all measured at a boxcar integrator that provides a gated measurement triggered by the pulse generator. These measured values are recorded by a computer which increments the current supplied to the device via the current controller and the measurements are all repeated. This measurement loop is repeated until the light measurement reaches a preset limit.

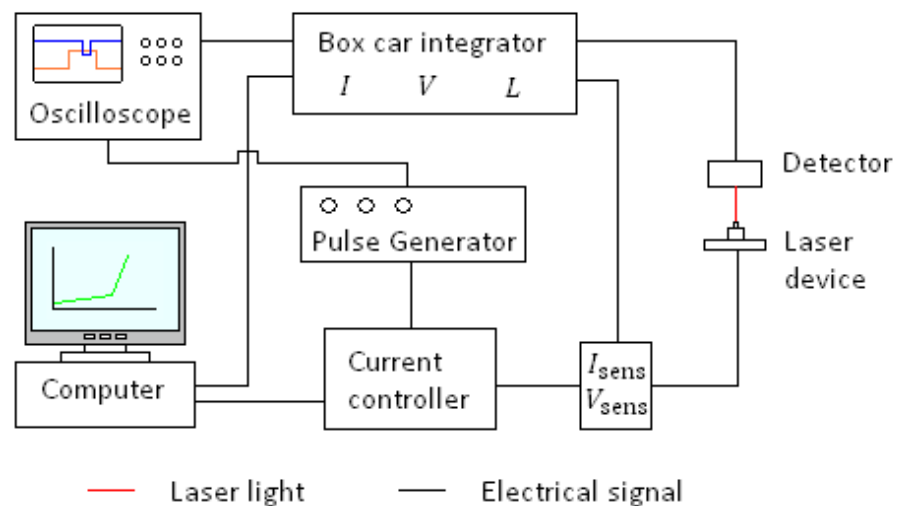


Figure 3.7 Experimental set up for measuring the current, voltage and light characteristics of laser devices.

3.3.3 Results

Both C-C and C-E devices have been processed from two different samples, namely S1 and S2, both of which originated from the same wafer. The L-I curves for these devices are presented in figure 3.8. A threshold current value has been extracted from each of the L-I curves by fitting straight line functions to both the above and

below threshold regions of the curve. The threshold current of a device, I_{th} , is taken to be the point of intersection of these two straight lines, see figure 3.8.

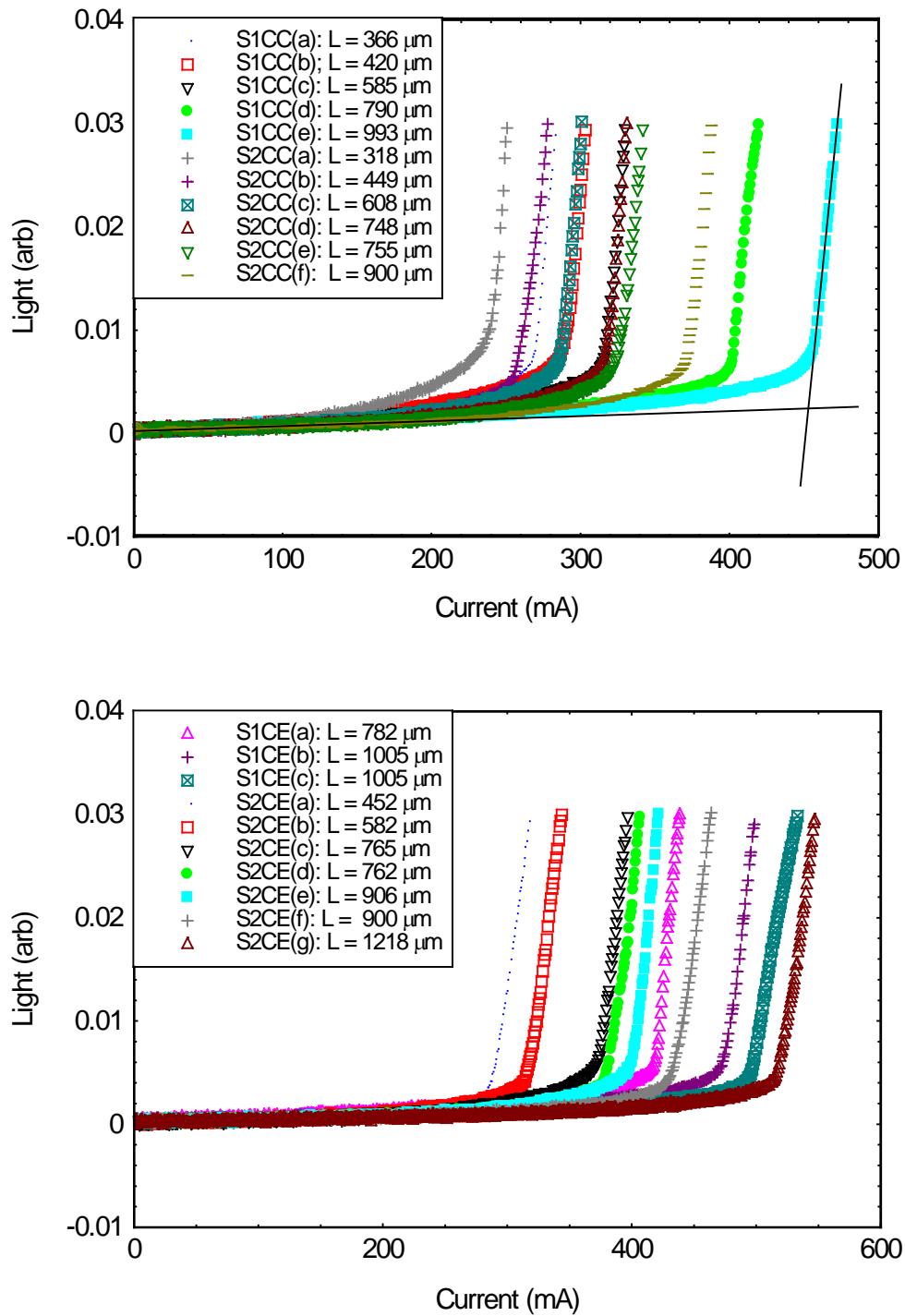


Figure 3.8 L-I curves for; C-C lasers (**above**), and C-E lasers (**below**) of various lengths at a temperature of $(23 \pm 1)^\circ\text{C}$. The two straight lines fitted to the S1CC (e) data in the upper plot demonstrate how the threshold current value is taken from the L-I curve.

The mode width, w , of each of the devices has been calculated by measuring the full width half maximum values of the near-field intensity distributions (distributed across the facet in the y -direction, as defined in figure 3.6). The length, L , of each device has been measured using a calibrated optical microscope. This allows the threshold current density, J_{th} , to be calculated by dividing the measured threshold current by the product of the device length and the mode width. This information has been summarised in appendix 3.

The C-C laser threshold current densities have been plotted in figure 3.9 against theoretical net modal gain values calculated using the measured device length and a cleaved facet reflectivity of $R_c = 0.31$ in equation 1.11. This data agrees, within experimental errors, with the peak net modal gain versus current density from figure 3.5, which has also been plotted in figure 3.9 for comparison.

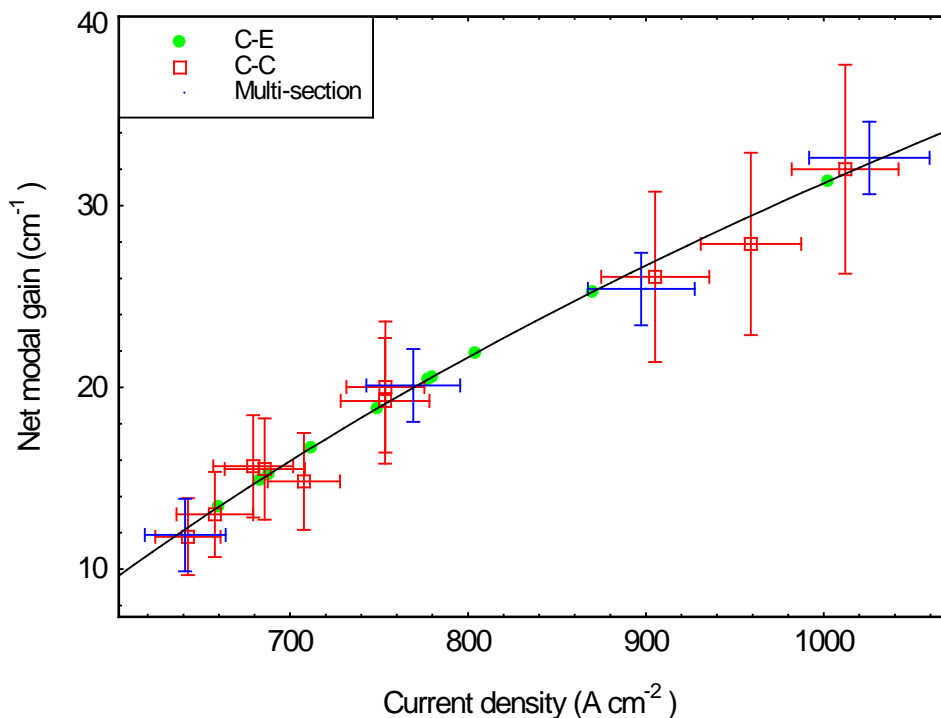


Figure 3.9 Plots of the net modal gain versus threshold current density for C-E laser (green circles) and C-C lasers (red squares). The peak net modal gain versus current density data for the multi-section device from figure 3.5 has been repeated here (blue circles) along with the logarithmic curve-fit (black line).

The threshold current densities for the C-E lasers have been plotted in figure 3.9 at the point at which they intersect the multi-section logarithmic curve-fit. The net modal gain value that corresponds to this point of intersection is used in equation 1.11 to calculate a value for etched facet reflectivity for each of the C-E lasers. This analysis results in a mean value for etched-facet reflectivity of $R_e = 0.15$ with a standard deviation of 0.04. The corresponding etched-facet efficiency value for the fabrication process described in chapter 2 is therefore $R_e/R_c = \eta = 0.48 \pm 0.13$.

3.4 Surface roughness phase broadening model

The reduced efficiency of etched laser facets has been described as a phase broadening effect [2]. In this model, the reflected wave front is treated as a superposition of Huygens elementary wavelets generated at all points along the facet surface. The optical path length difference experienced by each wavelet as it is reflected from the un-even surface, introduces a corresponding phase difference with respect to the rest. Considering only the specular reflection of normally incident light at a vertically uniform facet and assuming that the surface has a Gaussian height distribution, an analytical expression is derived for etched facet efficiency:

$$\eta_e(\Delta d) = e^{-16\left(\frac{\pi\Delta d}{\lambda}\right)^2} \quad (3.6)$$

where λ is the wavelength of the laser light inside the semiconductor and Δd is the root mean square (rms) roughness of the surface.

Following a similar approach here, but without assuming a Gaussian height distribution, direct measurement of an etched facet surface has been used to calculate numerically the reduced facet efficiency caused by phase broadening at the rough surface using equation 3.7.

$$\eta_e = \left| \sum_{j=0}^N \frac{e^{i\frac{4\pi d_j}{\lambda}}}{N} \right|^2 \quad (3.7)$$

where d_j is the relative surface height of the j^{th} data point with respect to the mean surface height.

3.4.1 AFM surface roughness measurements

The surface roughness of the etched laser facet has been measured using atomic force microscopy (AFM), a form of scanning probe microscopy commonly used to measure surface topography [10]. For the measurements presented here, the AFM has been operated in air using an alternating contact (A.C.) mode.

A silicon cantilever with a sharp tetrahedral tip is subjected to a forced oscillation above the surface of the sample using a piezoelectric oscillator. The cantilever is driven at its resonant frequency of about 70 kHz with an amplitude of around 100 nm. The amplitude is measured by a photodiode array that detects the deflection of a laser beam reflected from the back of the cantilever. The AFM scan is performed by moving the sample back and forth over a scan area in the $x - y$ plane using a piezoelectric stage. As the tip comes into contact with the surface, interactions between the two cause the amplitude of the tip to decrease. A feedback loop between the photo-detector and the stage adjusts the height of the sample in the z -direction in order to maintain constant tip amplitude. This height adjustment is recorded at each of the (x, y) scan co-ordinates thus generating a three dimensional map of the surface topography.

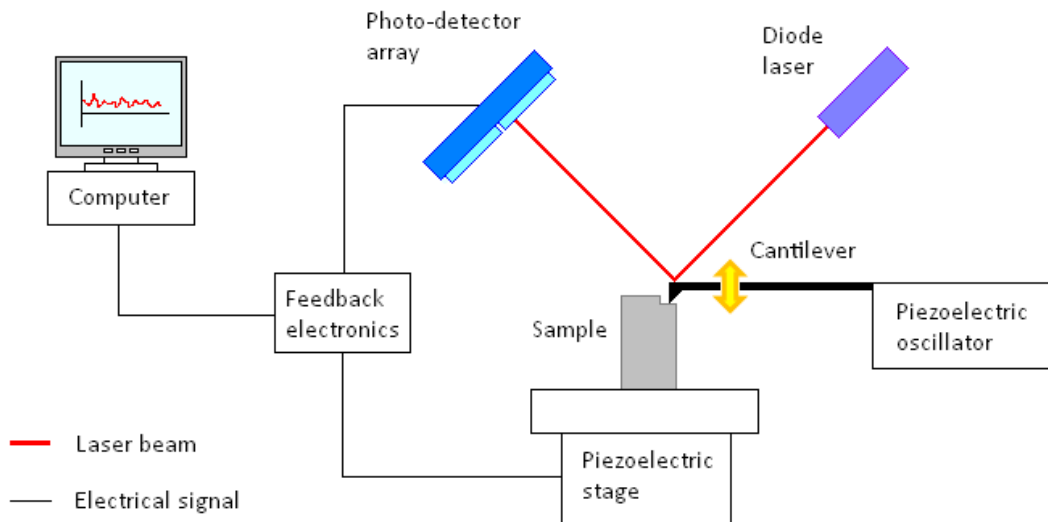


Figure 3.10 schematic of the AFM set-up used to measure facet surface topography.

3.4.2 Results

Figure 3.11 presents AFM scans of a cleaved and an etched facet surface. These samples have been taken from the S1 sample batch that was used to produce the threshold current data in section 3.3. Scanning electron microscope (SEM) images of similar surfaces have also been included in this figure for comparison with the AFM scans. However, it should be made clear at this point that the SEM images and AFM scans relate to different samples albeit each of the samples having been exposed to similar plasma etching conditions.

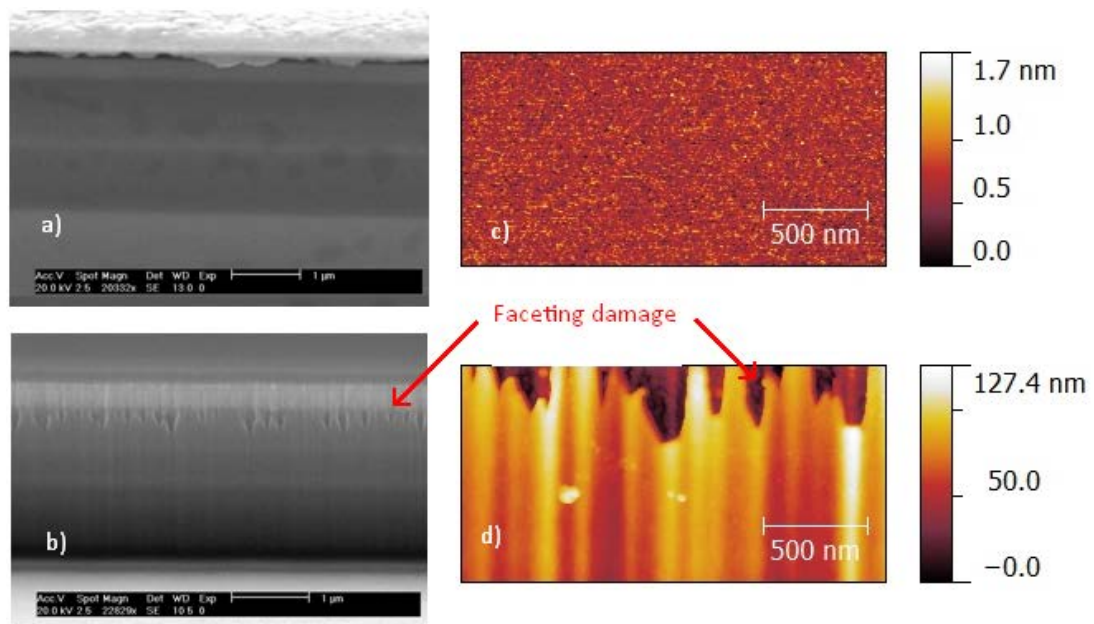


Figure 3.11 SEM images of a) a cleaved facet and, b) an etched facet, and, AFM colour maps of c) a cleaved facet and d) an etched facet.

Comparing the SEM and AFM images for the etched facet a clear correlation can be made between the facet features which appear in both. The characteristic damage caused by the faceting effect, which was highlighted in section 2.5 is apparent in the upper regions of both images. For the purposes of the analysis used here however, it has been assumed that vertical extent of this damage is sufficiently limited so that it does not interfere with the optical cavity mode. For the particular etching process used in this work, this assumption is considered reasonable as long as the SiO_2 etch mask used is no less than 300 nm thick.

This leaves the regular vertical striations, assumed to be transferred from the patterning process, which are also present in both images. The AFM image reveals however, that the peak amplitude of these features is rather varied, a fact that is not immediately obvious from inspection of the SEM image alone. From the bottom edge of the faceting damaged region down through the full extent of the AFM image, the vertical striations are approximately uniform. A single horizontal row of the etched facet AFM data, marked by the scale bar on figure 3.11 (d), has therefore been taken as representative of the vertical facet features for the sample. Similarly, a single line of the cleaved facet AFM data has been taken from figure 3.11 (c) for comparison. These single line data are presented in figure 3.12.

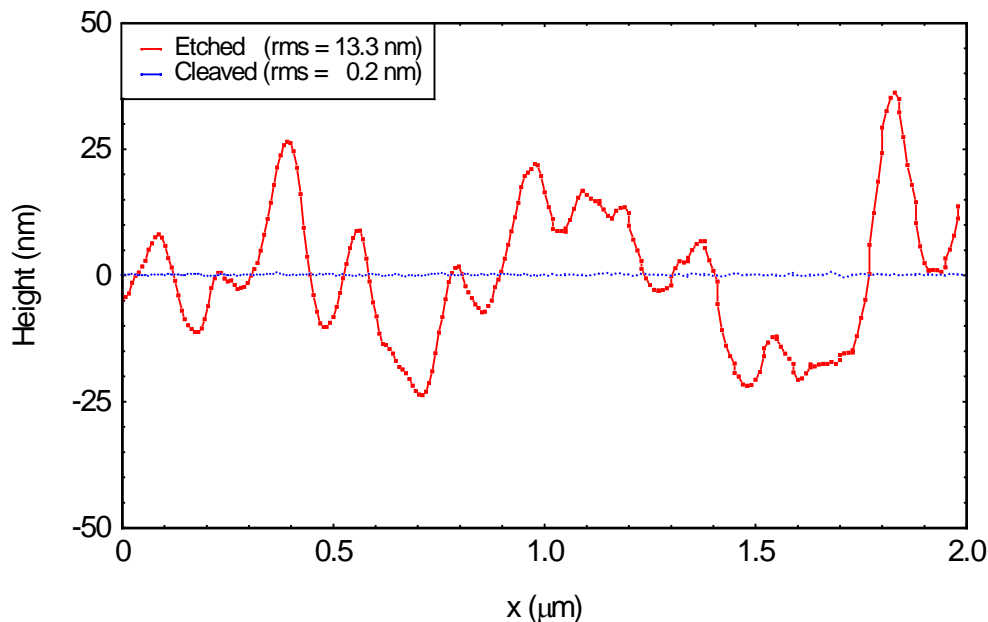


Figure 3.12 is plot of the surface height of the cleaved facet (blue line) and etched facet (red line) taken along a single horizontal line of the figure 3.11 AFM data.

The mean surface height of the data presented in figure 3.12 has been set to zero so that the standard deviation of the data is equal to the root mean square roughness for each of the curves. The rms roughness value for the etched facet is more than an order of magnitude greater than that of the cleaved facet and corresponds to a value of $\lambda/14$ for the particular AlGaInP material that has been used. Using equation 3.7 to analyse the etched facet height data from figure 3.12 gives a facet efficiency value of 0.41.

In figure 3.13 the etched facet height distribution has been plotted against the Gaussian probability function for the same data.

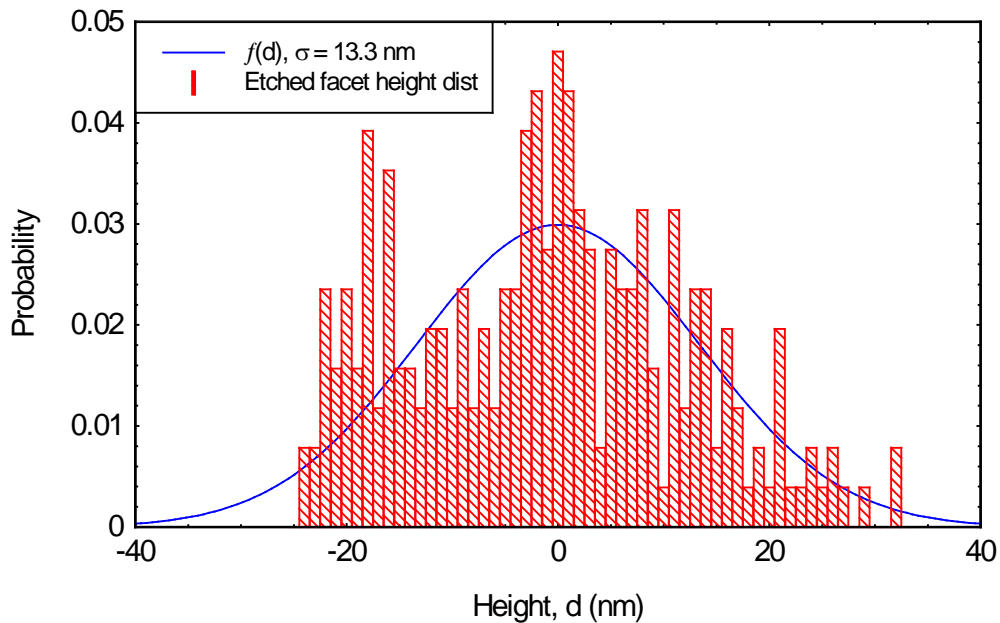


Figure 3.13 Etched facet height probability distribution (red bars) plotted for the single AFM line scan presented in figure 3.12, and, the Gaussian probability distribution for the same data (blue curve).

In spite of the fact that the Gaussian probability function is a poor fit to the etched facet data, the standard deviation, σ , has been used in equation 3.6 in place of Δd , the rms surface roughness, to yield an etched facet efficiency value of 0.43.

The theoretical values calculated using equations 3.6 and 3.7 both agree, within errors, with the measured value of 0.48 ± 0.13 presented in section 3.3. This close agreement between theory and experiment suggests that the phase broadening mechanism is a reasonable explanation for the loss of facet efficiency caused by sub-wavelength features.

In figure 3.14 a Fast Fourier Transform (FFT) of the etched facet line scan data from figure 3.12 reveals dominant Fourier components corresponding to spatial features with periods of 140 nm, 200 nm and 250 nm.

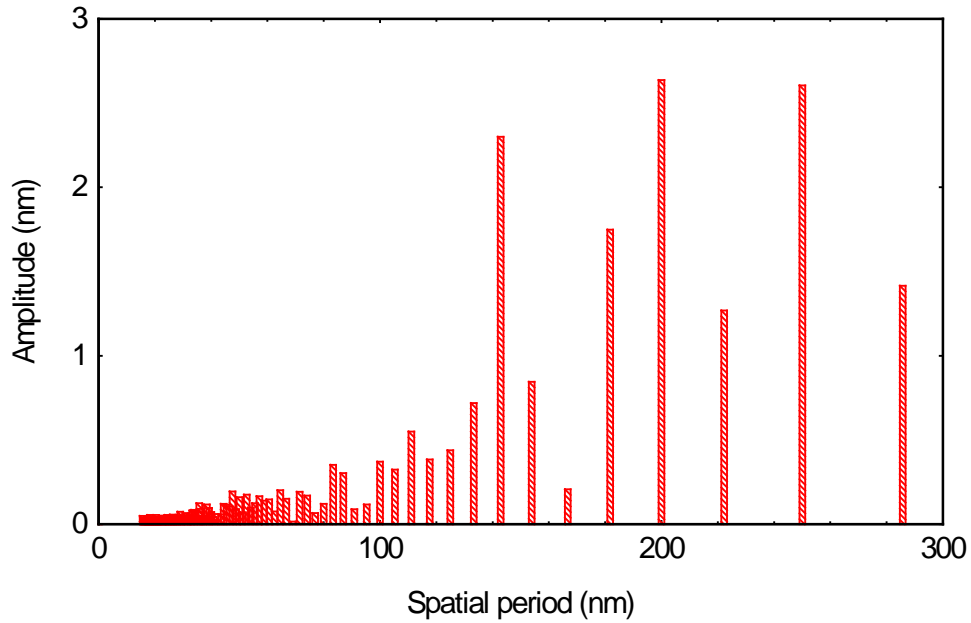


Figure 3.14 Is a Fast Fourier transform (FFT) of the etched facet AFM single line scan data presented in figure 3.12. The FFT reveals that the three main spatial components have periods of 140 nm, 200 nm and 250 nm.

There is little evidence of the expected correlation between the periodicity of the etched facet striations and the 100 nm electron beam lithography (EBL) step size that was suggested in section 2.5.1. Nevertheless, these features do, in all probability, arise from the combined lithographic/dry etching process steps that have been used to produce the etched facets. It is therefore expected that optimisation of these steps would result in a reduction in facet roughness and a corresponding improvement in etched facet efficiency.

3.5 Summary

A methodology for the characterisation of etched-facet lasers has been presented. The net modal gain and absorption of an AlGaInP segmented contact device have been measured as a function of current density. The light – current characteristics of both cleaved -cleaved (C-C) and cleaved - etched (C-E) facet lasers have been measured and used to calculate the threshold current densities for these devices. The net modal gain versus threshold current density data for the C-C lasers shows good agreement with the multi-section net modal gain data demonstrating that, if any damage was sustained by these devices during plasma etching, then it is reasonable to assume that it is common to both. A logarithmic function, fitted to the multi-section peak net modal gain data, has been used to calculate the threshold gain corresponding to each of the C – E laser threshold current densities. Relating the threshold gain values to facet reflectivity using equation 1.11 gives a mean value for etched facet efficiency of 0.48 ± 0.13 .

The surface topography of an etched laser facet has been characterised using atomic force microscopy (AFM). The facet features that arise from the processing techniques used, as highlighted in chapter 2, can also be identified in the AFM results. Surface height data taken from a single AFM scan line has been used in a simple phase broadening model to calculate a value for the etched-facet efficiency of 0.41 which agrees, within errors, with the experimental value of 0.48 ± 0.13 .

References

- [1] D. A. Francis, C. J. Chang-Hasnain and K. Eason "Effect of roughness on etched-facet semiconductor laser diodes", *Applied Physics Letters*, 68 (12), p.1598, 1996.
- [2] D. A. Stocker, E. F. Schubert, W. Grieshaber, K. S. Boutros and J. M. Redwing "Facet roughness analysis for InGaN/GaN lasers with cleaved facets", *Applied Physics Letters*, 73 (14), p.1925, 1998.
- [3] J. L. Merz and R. A. Logan "GaAs double heterostructure lasers fabricated by wet chemical etching", *Journal of Applied Physics*, 47 (8), p.3503, 1976.
- [4] L. A. Coldren, K. Furuya, B. I. Miller and J. A. Rentschler "Etched mirror and Groove-Coupled GaInAs/InP Laser Devices for Integrated Optics", *IEEE journal of Quantum Electronics*, 18 (10), p.1679, 1982.
- [5] P. Blood, G. M. Lewis, P. M. Snowton, H. Summers, J. Thomson, and J. Lutti "Characterization of Semiconductor Laser Gain Media by the Segmented Contact Method", *IEEE Journal of Selected Topics in Quantum Electronics*, 9 (5), p.1275 2003.
- [6] J. W. Lee, S. J. Pearton, C. R. Abernathy, W. S. Hobson and F. Ren "Damage introduction in InGaP by electron cyclotron resonance Ar plasmas", *Applied Physics Letters*, 67 (21), p.3129, 1995.
- [7] G. M. Lewis "Study of Spontaneous Emission and Gain from Strained $(Al_yGa_{1-y})_xIn_{1-x}P$ Quantum Well Laser Diodes" PhD Thesis, Cardiff University, 2003.
- [8] P. M. Snowton, H. D. Summers, P. Rees and P. Blood "Optimisation of 670 nm strained-quantum-well laser diodes for high-temperature operation", *IEE Proc.- Optoelectronics*, Vol. 141, No. 2, p.136, 1994.
- [9] K. Griffiths "Automated Laser Diode Measurements", MPhil Thesis, UWCC, 1992
- [10] R. Wiesendanger "Scanning Probe Microscopy and Spectroscopy Method and Applications", Cambridge University Press, 1994.

Chapter 4:

The coupled-cavity sensor

4.1 Introduction

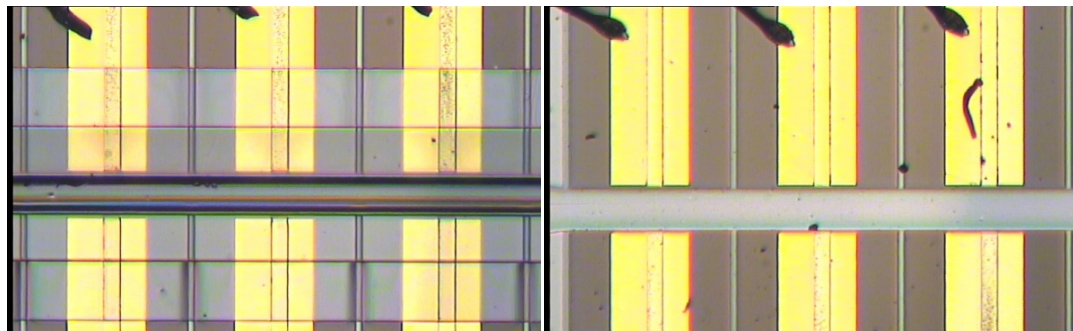
The threshold gain model presented in section 1.4 was used to demonstrate how coupled-cavity modes can have lower threshold gain values than modes formed in either of the individual laser sections of the coupled-cavity device. A perturbation of the gap section loss, caused by a passing cell, could therefore be used to initiate a change in the device from it lasing as a coupled-cavity, to lasing as two individual lasers or not lasing at all. Evidence of the interaction between the analyte and the optical mode in this case would be contained within the light output measured from the device.

This chapter presents the results of an investigation into the nature of the coupling between the laser sections of the coupled-cavity device. The aim of this investigation has been to find out whether coupled-cavity modes can be established in a device with 125 μm wide gap coupler and, if so, can a perturbation to the gap loss be detected in the device output. In section 4.2 the coupling between the laser sections of the prototype device has been investigated by measuring the photo-current generated in one section due to optical input from another. In section 4.3, evidence for the formation of coupled-cavity modes is presented in the interpretation of the light versus current characteristics (L- I) and lasing spectra of a coupled-cavity device.

The sensitivity of the device to a gap loss perturbation has also been explored in section 4.4 by measuring the spectral output of the device with and without a scattering object positioned inside the gap coupler. Section 4.5 presents a multi-mode travelling wave rate equation model that has been developed to simulate the behaviour of a coupled-cavity device in order to provide further understanding of the coupling mechanism.

4.2 Light source/photo-detector configuration

In its simplest form the coupled-cavity device can be operated as a combined light source and photo-detector. By forward biasing one section, the resulting light that is transmitted across the gap and coupled into the active region of the opposing section, can be detected by measuring the photo-current generated in that section. To test whether the SU-8 electrical isolation layers (described in chapter 2) have any effect on the coupling between laser sections, the L-I characteristics of a forward biased 'source' section have been measured using the photo-current generated in the opposing 'detector' section for a device with SU-8 channel layers and one without, see figure 4.1.



a)

b)

Figure 4.1 Plan view images (taken through a X10 optical microscope) of a coupled-cavity device array (a) with a 115 μm wide SU-8 channel and (b) with the bare 125 μm wide foundation channel etched in to the semiconductor crystal.

The section lengths for each of the devices are presented in table 4.1.

Table 4.1 Section lengths of the devices used to measure photo-current versus input current.

Device	Source length $\pm 2 \mu\text{m}$	Detector length $\pm 2 \mu\text{m}$
T1 (with SU-8)	1035	1077
T2 (without SU-8)	1028	1005

The photo current has been measured using the experimental set up that was illustrated in figure 3.5, only here, the detector section of the coupled-cavity device (as opposed to the reverse biased silicon photo detector) is connected directly to the input terminal of the boxcar generator, see figure 4.2.

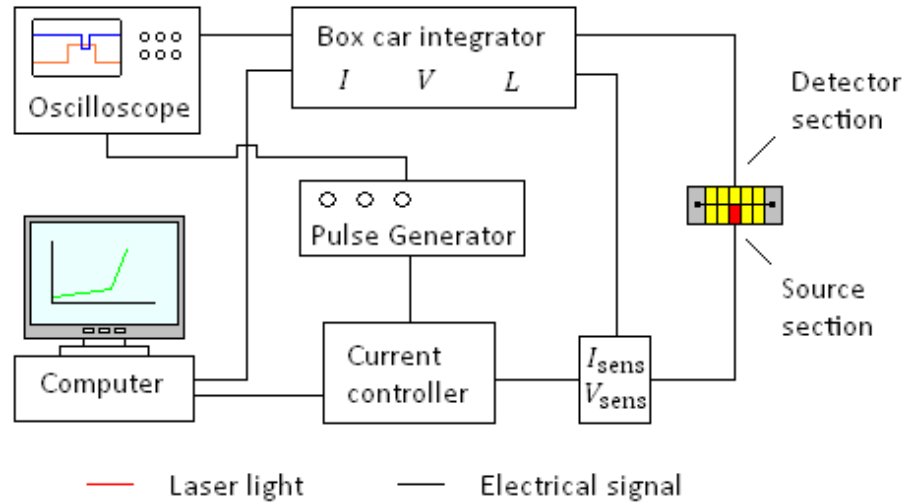


Figure 4.2 Experimental set up used to measure the photo current generated in a coupled-cavity detector section as a function of the forward bias current injected into an opposing source section.

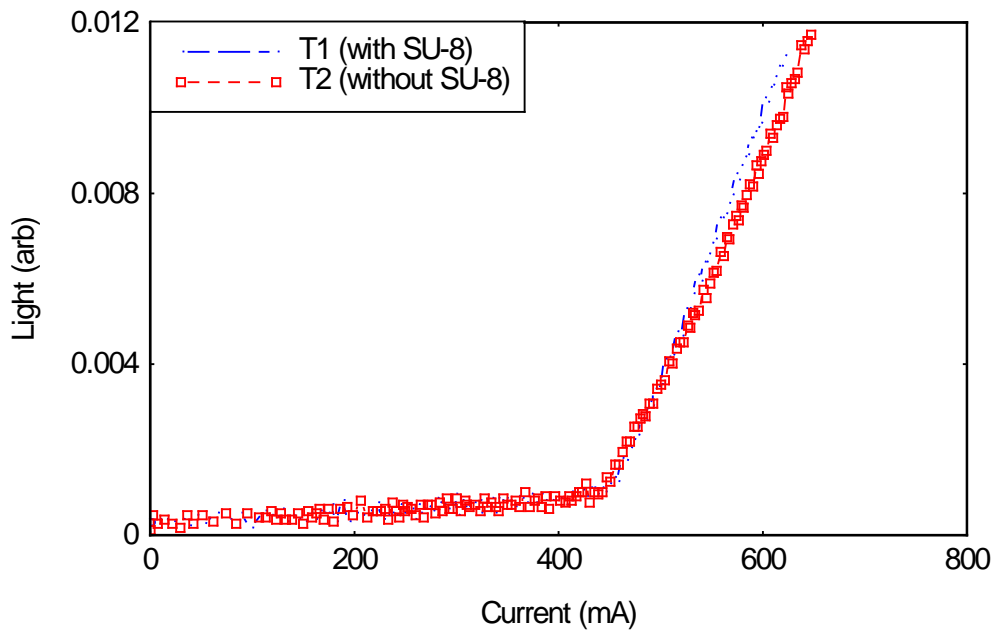


Figure 4.3 L-I curves for a coupled-cavity device with an SU-8 micro-fluidic channel (blue circles) and one without (red squares) measured using one section as a source and the other as a detector.

The $L - I$ curves that result from using the device in the source/detector configuration are presented in figure 4.3. The sharp change in gradient associated with the transition from below threshold spontaneous emission to above threshold lasing is well defined for both T1 and T2. The ability to measure such well defined $L - I$ curves, demonstrates that light must be coupled across the gap from one section to the other. Furthermore, the threshold current values and above threshold gradients of the $L - I$ curves for each of the devices are very similar, indicating that the presence of the SU-8 channel layer has very little influence on the behaviour of either the individual laser sections or the coupling between them.

The advantages of proximity and alignment that are inherent in the monolithic source/detector configuration are somewhat negated by the limited area of the active region available when using a quantum well device as an in-plane detector. Nevertheless, the level of sensitivity demonstrated in these measurements, combined with the self-contained nature of the monolithic source/detector configuration, highlights the potential of the MFCC device for micro total analysis systems (μ TAS) bio-sensing applications.

4.3 Coupled-cavity modes

In spite of the large gap coupler used in the MFCC design ($L_g = 125 \mu\text{m}$) the results presented in section 4.2 demonstrated that light can be coupled from one of the laser sections of the device to the other. In order for coupled-cavity modes to form within the device however, not only does there need to be a significant coupling of optical power, but, the light that is resonant in each of the individual laser sections must also be wavelength matched. Evidence for coupled modes exists within both the power and spectral content of the device output. In order to establish whether coupled-cavity modes can be formed within such a device, the L- I characteristics and lasing spectra of coupled-cavity sections T2 (4 + 14) have been measured (the parenthetical part of the device designation refers to section numbers assigned to each of the lasers of the device array. One side of the channel being numbered 1 – 10 and the other 11 – 20 so that there is always a difference of 10 between coupled sections).

The L – I curves for the individual laser sections have been measured using the experimental set up described in section 3.3.2. When measuring the L – I characteristics for the coupled-cavity, it is necessary to drive each section independently with a separate current source so that the current density throughout the device is well matched. A second pulse generator is therefore used to drive one section with a fixed input current while the L – I characteristics of the opposing section are measured using a computer controlled pulse generator. This process is repeated at 20 mA increments, for the fixed current section, over a range extending above and below threshold. The cavity lengths and mode widths of each section (measured using the techniques described in section 3.3.3) are used to equate the current densities in each section so that the light measurement value corresponding to each of the fixed input currents can be taken from each of the L – I curves generated from the computer controlled section.

To compare the $L - I$ characteristics of the individual sections to those of the coupled-cavity, the data has been plotted as light versus current density ($L - J$) in each case, see figure 4.4.

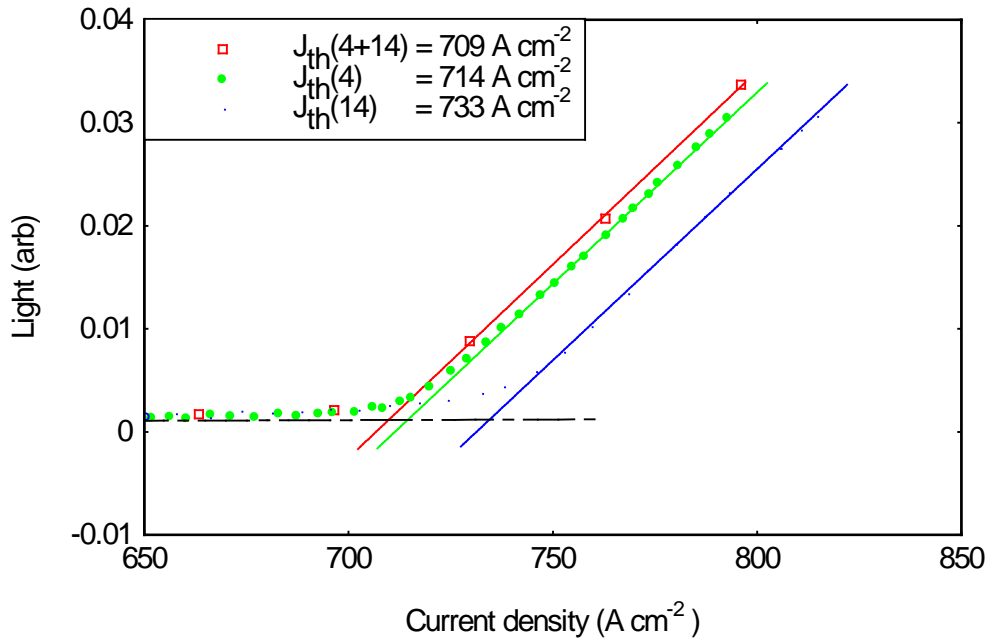


Figure 4.4 Comparison of the light versus current density of the coupled-cavity T2 (4+14) and the individual laser sections T2 (4) (green circles) and T2 (14) (blue circles).

Due to the differences in the cavity lengths and mode widths of the individual laser sections, the threshold current densities of each are quite different. Each laser section therefore, will operate at a slightly different wavelength due to the current density dependence of the peak modal gain, see figure 3.4. Nevertheless, the $L - J$ curve for the coupled-cavity does yield a lower threshold current density than either of the individual sections on their own, which implies a degree of coupling between them. However, because of the spectral misalignment of the individual laser sections, it is not clear whether the coupling occurs via a single coupled-cavity

mode or whether the threshold current density is reduced due to the shorter wavelength section optically pumping the longer wavelength section.

In order to determine the cause of the reduced coupled-cavity threshold current density, the spectral output of the device, when each of the laser sections is operated individually and when both sections are operated together, has been measured using an optical spectrum analyser. In each case the device has been operated with a current density just above the threshold values given in figure 4.4. The spectra have been measured using the experimental set up illustrated in figure 4.5. Again, two separate pulse generators are used to drive the individual laser sections independently. The emission from the device is coupled into a multimode fibre optic cable using an objective lens. The fibre then couples the light into an optical spectrum analyser which measures the optical power as a function of wavelength with a resolution of 0.5 nm.

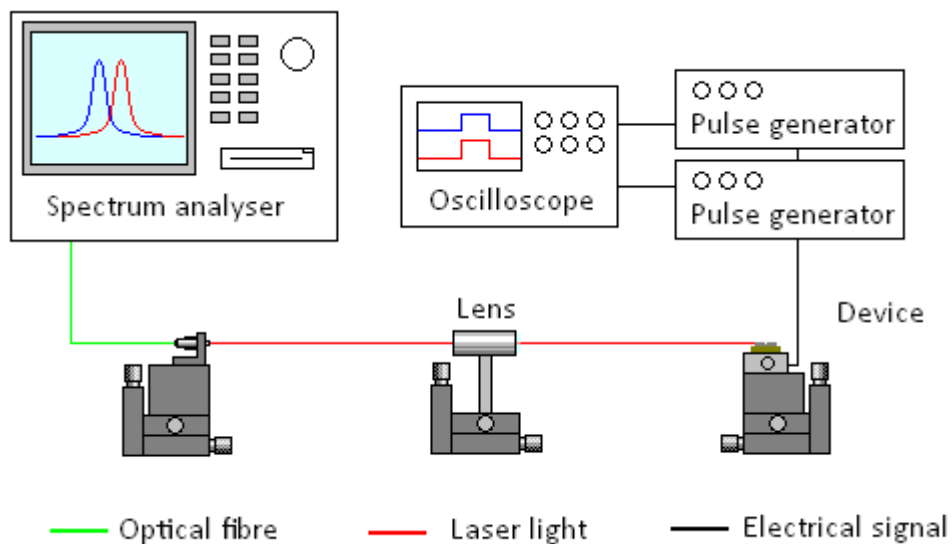


Figure 4.5 Experimental set up used to measure the spectral output of the coupled-cavity device.

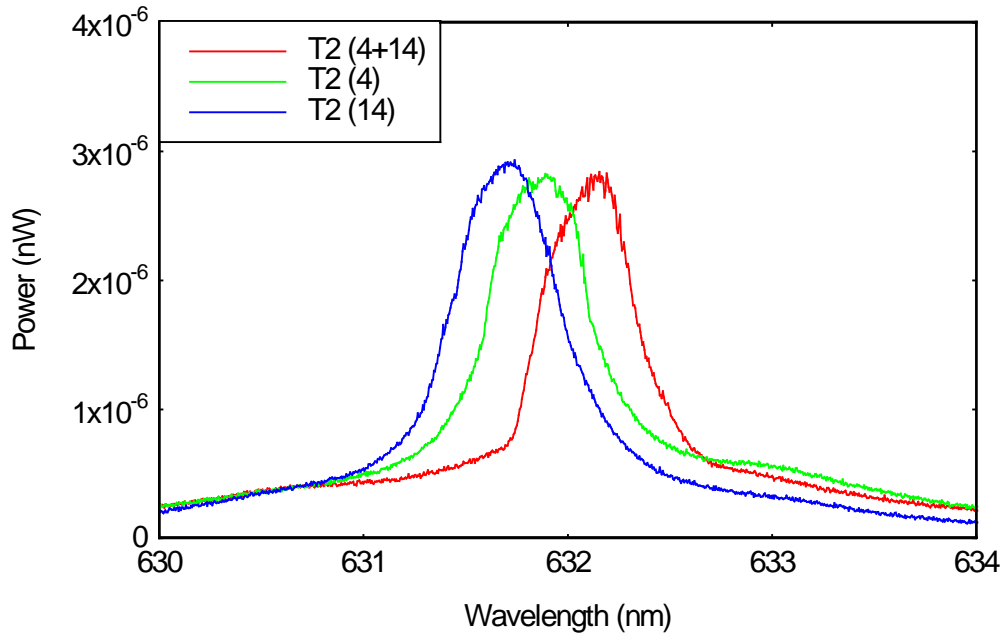
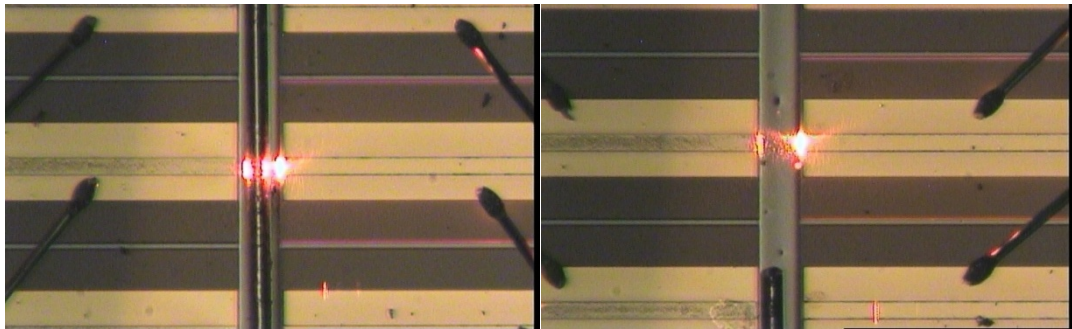


Figure 4.6 Lasing spectra for the coupled-cavity, T2 (4+14), (red line) and for the individual sections T2 (4) (green line) and T (14) (blue line) driven independently.

The lasing spectra of the individual sections presented in figure 4.6 confirm that the two sections are not well aligned spectrally; the section with the higher threshold current density operates at shorter wavelength and the section with lower threshold current density has a longer wavelength, which is consistent with the carrier density dependence of the spectral gain peak, see figure 3.4. When both sections are operated together, the output shifts to a longer wavelength than that of either of the individual sections on their own. Furthermore, the peak wavelength of the coupled-cavity output is the same when collected from either end of the device. Even though this spectral shift is not large, the fact that it is to a longer wavelength than either of the individual sections implies that it is due to a change in the threshold gain requirement of the lasing mode. This is a strong indication that the device is lasing as a coupled-cavity. If the reduction in threshold current density of the device demonstrated in figure 4.4 was due to optical pumping, rather than the formation of coupled-cavity modes, the output wavelength should correspond to that of the individual laser sections.

4.4 Coupled-cavity sensing mechanism

Having established evidence for coupled-cavity mode formation in the spectral output of the coupled-cavity device T2 (4 + 14), the gap loss dependence of these modes has been investigated by placing a scattering object inside the gap coupler of the device. A fibre glass rod with a diameter of approximately 50 μm has been positioned in the deep etched channel between the coupled laser sections, see figure 4.7 (a). The rod only extends along half of the channel length, see figure 4.7 (b), allowing the output from obstructed and unobstructed sections to be compared.



a)

b)

Figure 4.7 Plan view photographs (taken through a X10 optical microscope) of device T2 (a) with a fibreglass rod placed between the laser sections of the coupled-cavity and (b) an unobstructed coupled-cavity pair. In each case the right hand section is lasing.

Using the experimental set up illustrated in figure 4.5, the lasing spectra of the section T2 (4) and the coupled-cavity sections T2 (4 + 14) have been measured with the glass rod inside the gap coupler, see figure 4.8. In each case, the same input currents that were used to generate the spectra for the same device without the glass rod (figure 4.6), have been used here again. The peak wavelength values of the resulting spectra are almost identical for the individual section and for the coupled-cavity sections. This implies that, with the glass rod in place, the optical coupling between the two sections is reduced, which suppresses the coupled-cavity modes so that the output no longer shifts to longer wavelength when operating both sections together. This corresponds to a difference in wavelength for the

device with the rod and without the rod of $\Delta\lambda = 20 \pm 5 \text{ \AA}$. The output from an adjacent, unobstructed device, T2 (9 + 19), has also been measured for comparison, see figure 4.9.

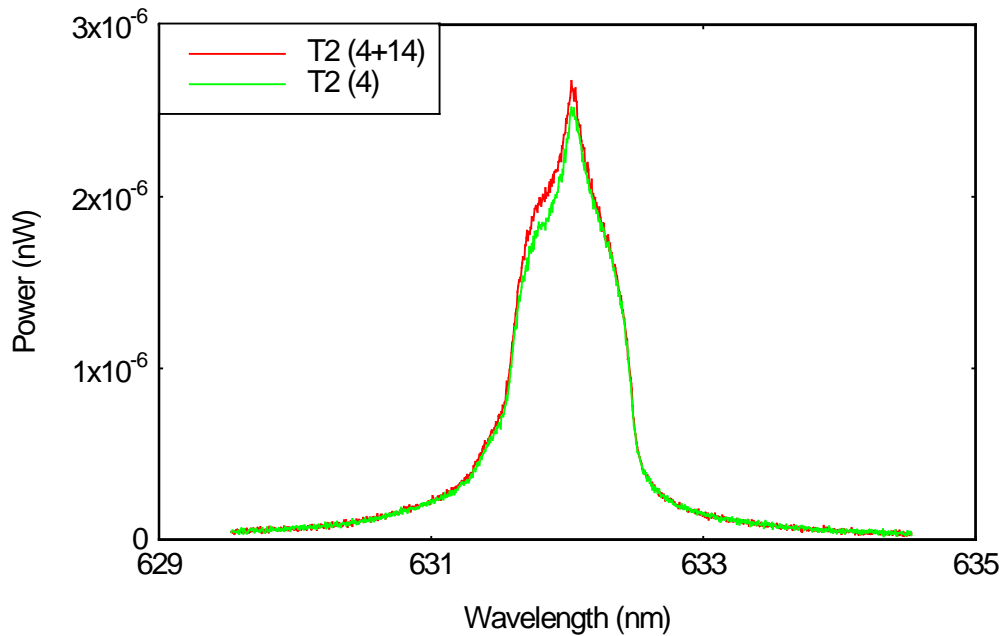


Figure 4.8 Lasing spectra for section T2 (4) (green line) alone and for both sections T2 (4+14) driven at the same time (red line) i.e. the coupled-cavity.

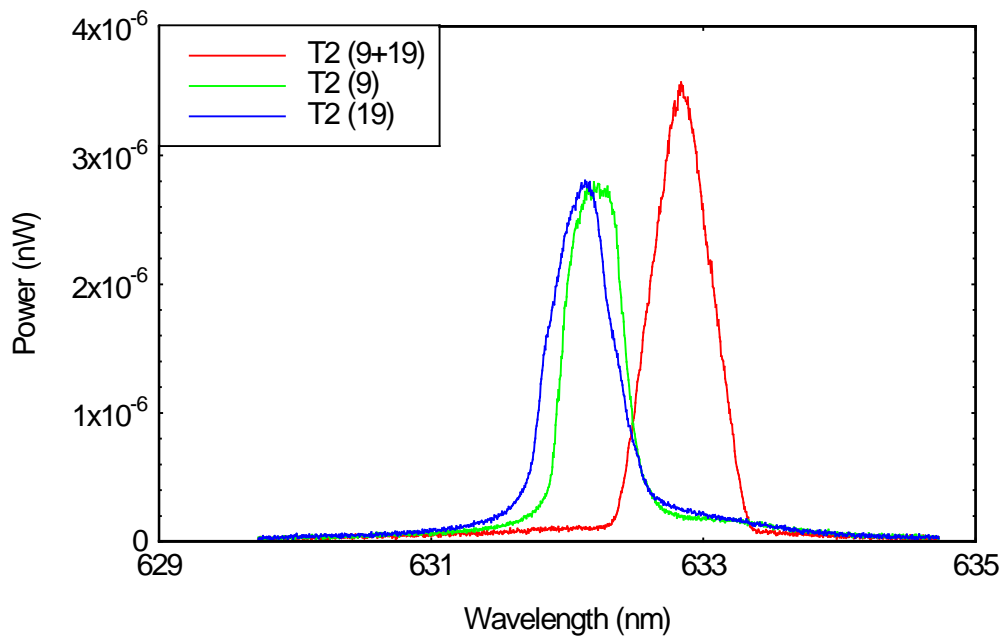


Figure 4.9 Lasing spectra for sections T2 (19) (blue line) and T2 (9) (green line) operated individually and for both sections T2 (9+19) operated together (red line).

The spectra measured for the unobstructed device (see figure 4.9), exhibit much the same behaviour as was interpreted as evidence for coupling in section 4.3. This indicates that these sections are lasing as a coupled-cavity and so the suppression of the coupled-cavity mode in the sections with the obstruction is indeed due to the obstruction rather than any other influence.

4.5 Multi-mode travelling wave rate equation model

To provide further analysis of the experimental results presented in the preceding sections, a multi-mode travelling wave rate equation model has been developed to simulate the behaviour of the coupled-cavity device. In contrast to the simple threshold gain model introduced in section 1.4, where the coupled-cavity output was inferred by interpreting threshold gain maps, the rate equation approach allows the output of the simulated device to be related directly to control parameters that would be used in the 'real world' device i.e. the input currents of the two laser sections. Furthermore, using the travelling wave approach to solving the rate equations [1, 2] allows spatial variations in the gain medium, caused by the non-uniform photon density, to be accounted for while, simultaneously solving over multiple modes includes the spectral dependence of the gain medium [2, 3].

4.5.1 Rate equations

The exchange of energy between the carrier density and the left and right travelling photon densities within the device can be described using the multi-mode travelling wave rate equations, see equation 4.1 - 4.3.

$$\left. \frac{dPr}{dt} \right|_{i,s} = \beta B n_s^2 + c_g G(n_s, \lambda_i) Pr_{i,s-1} \quad (4.1)$$

$$\left. \frac{dPl}{dt} \right|_{i,s} = \beta B n_s^2 + c_g G(n_s, \lambda_i) Pl_{i,s+1} \quad (4.2)$$

$$\left. \frac{dn}{dt} \right|_s = \frac{J_s}{eh} - \frac{n_s}{\tau(n_s)} - c_g \sum_{i=i_{min}}^{i_{max}} G(n_s, \lambda_i) (Pr_{i,s} + Pl_{i,s}) \quad (4.3)$$

Equation 4.1 is the generation/recombination rate for the right travelling photon density, Pr , associated with the i_{th} mode and equation 4.2 is the equivalent for the left travelling photon density, Pl , and equation 4.3 is the generation/recombination rate for the carrier density that is common to all modes. The carrier density dependent carrier lifetime that appears in equation 4.3 is calculated using equation 4.4.

$$\tau(n_s) = \frac{1}{A + Bn_s} \quad (4.4)$$

where A is the nonradiative recombination rate and B is the spontaneous emission rate and all other rate equation parameters used in the model have been summarised in table 4.2. The subscript, s , in equations 4.1 – 4.4 is an integer that denotes the cavity segment to which each set of rate equations applies. The gain function $G(n_s, \lambda_i)$ is discussed in further detail in section 4.5.2.

Table 4.2 Rate equation parameters used to model the GaInP/AlGaInP SQW MFCC device.

Parameter	Symbol	Value
Spontaneous emission factor [3]	β	1×10^{-4}
Nonradiative recombination rate	A	$2.5 \times 10^9 \text{ s}^{-1}$
Radiative recombination rate [†]	B	$1 \times 10^{-10} \text{ cm}^3 \text{ s}^{-1}$
Electronic charge	e	$1.6 \times 10^{-19} \text{ C}$
Group velocity [†]	c_g	$8.5 \times 10^9 \text{ cm s}^{-1}$
Quantum well thickness	h	$1 \times 10^{-6} \text{ cm}$
Facet reflectivity coefficient [3]	R	0.3
Etched facet efficiency (chapter 3)	η	0.5

[†] Values taken from www.ioffe.rssi.ru/SVA/NSM/Semicond/GaInP/index.html on 08/06/12.

To implement the travelling wave rate equation scheme, the coupled-cavity geometry illustrated in figure 1.14 is divided into spatially discrete segments along the length of the optical axis of the device, see figure 4.10.

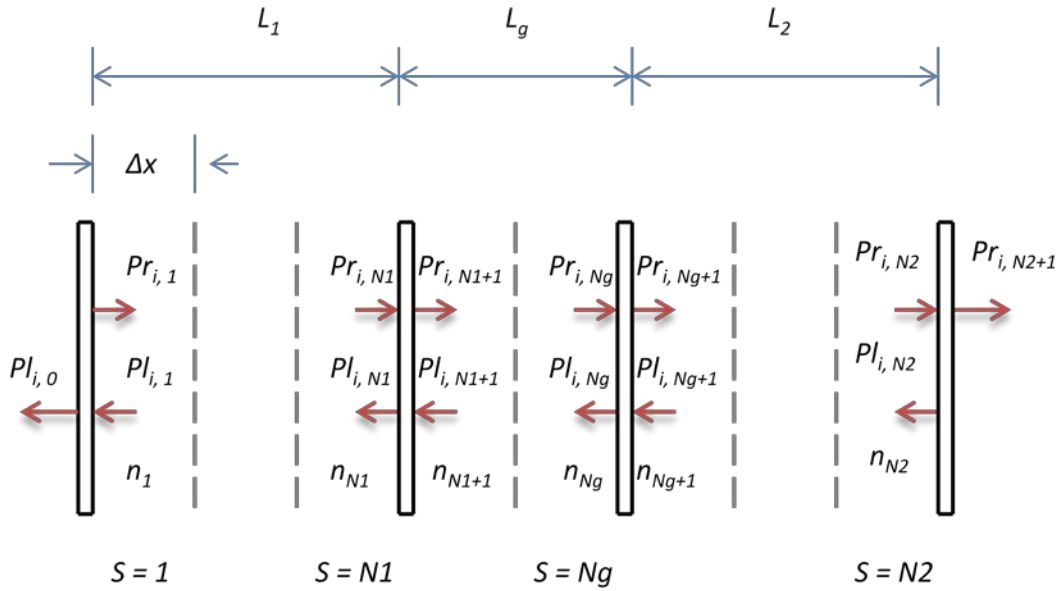


Figure 4.10 Schematic illustration of the coupled-cavity travelling wave scheme. Each segment contains a photon density for the i^{th} mode travelling to the right, Pr , and to the left, Pl , and a common carrier density n .

For a given set of input parameters, the time evolution of the carrier and photon densities throughout the device can be calculated from a known set of initial values, by iteratively solving equations 4.1 - 4.4 for each of the cavity segments using a finite time step, Δt . The typical time step required for numerical stability is around 10^{-13} s. By relating the time increment used to the length of the cavity segments, Δx , via the group velocity (see equation 4.5) each of the photon densities is stepped forward by exactly one segment on each iteration of the calculation. As the photon densities evolve in time they also travel, segment by segment, across the device.

$$\Delta t = \frac{1}{c_g} \Delta x \quad (4.5)$$

Diffusion of carriers is not accounted for in this model so the carrier densities do not cross segment boundaries.

The reflection and transmission of the travelling photon densities at the inner and outer facets is dealt with by applying the appropriate boundary conditions, see equations 4.6 – 4.11. Gap losses are included by defining a distributed gap loss (appendix 2), α_g , that is used in place of the gain functions $G(n_s, \lambda_i)$ in the photon density rate equations when applied to each of the gap coupler segments.

$$Pr_{i,1} = \eta R \cdot Pl_{i,1} \quad (4.6)$$

$$Pr_{i,N1+1} = \eta(1 - R) \cdot Pr_{i,N1} \quad (4.7)$$

$$Pl_{i,N1} = \eta R \cdot Pr_{i,N1} + \eta(1 - R) \cdot Pl_{i,N1+1} \quad (4.8)$$

$$Pl_{i,N2} = \eta R \cdot Pr_{i,N2} \quad (4.9)$$

$$Pl_{i,Ng} = \eta(1 - R) \cdot Pl_{i,Ng+1} \quad (4.10)$$

$$Pr_{i,Ng+1} = \eta R \cdot Pl_{i,Ng+1} + \eta(1 - R) \cdot Pr_{i,Ng} \quad (4.11)$$

Due to the large size of the gap coupler, the transmission and reflection coefficients used to model the gap coupler section have been reduced to their first order components (based on the approximation that was discussed in section 1.4.1). This allows the transmission of photons across the gap to be modelled as a function of time rather than using the scattering matrix approximation where multiple round trips of the gap are assumed to occur instantaneously [2, 3] which, for the larger gaps, is clearly no longer a valid approximation.

4.5.2 Gain functions

The effects of the non-linear gain medium have been included in the rate equation model by fitting a series of gain functions to the current density dependency of the net modal gain spectra (presented in figure 3.4) - one gain function for each of the measured wavelengths. In order to achieve an accurate fit over the full range of data, two separate logarithmic functions are required for each of the gain functions, see figure 4.11. Each of the resulting gain function pairs is used to describe the gain/loss experienced by a different mode in the multi-mode rate equations.

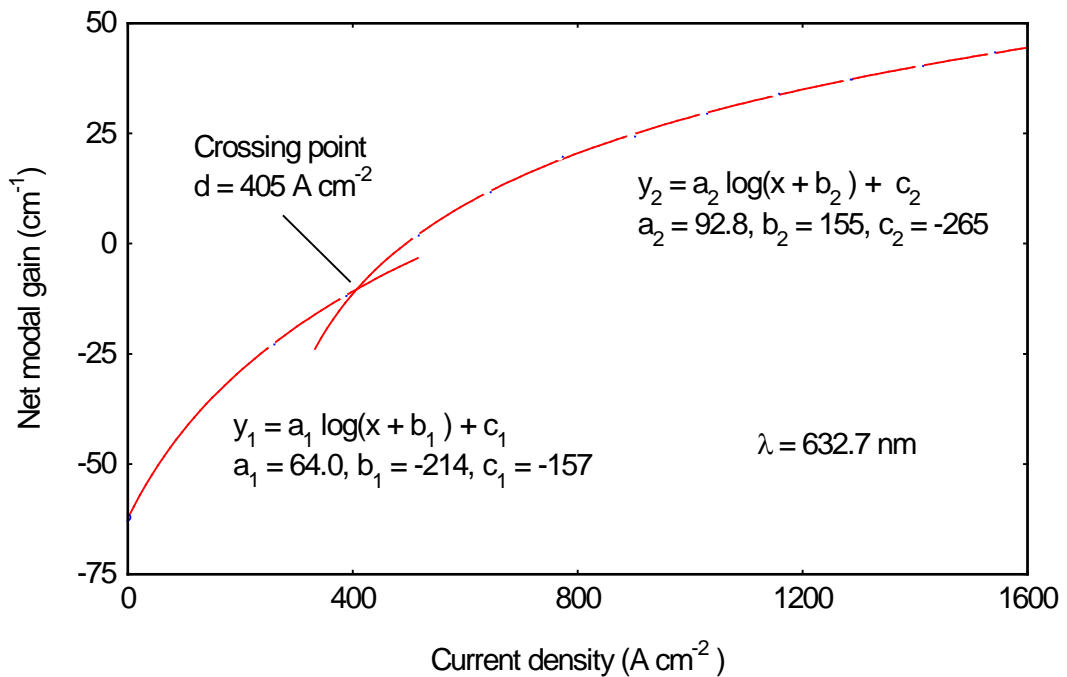


Figure 4.11 Logarithmic gain fitting functions used to model the modal gain/loss of the optical mode corresponding to a wavelength of $\lambda = 632.7$ nm in the multi-mode rate equations.

The two separate log functions are fitted to the raw data using a Mathcad V.14 logarithmic regression function. The resulting set of fitting parameters is passed into a FORTRAN 95 program that is used to numerically solve the rate equations. The crossing point of each of the paired log functions is also needed in order for the programme to decide which function to use for a given carrier density.

The current density dependency of the gain functions is converted to a carrier density dependency using equation 4.12 (this equation is derived from the steady-state solution of the carrier density rate equation (equation 4.3) i.e. $dn/dt = 0$, and by assuming that, for the multi-section device used to measure the gain data, the photon density is low enough that the stimulated emission/absorption term can be neglected i.e. the third term on the left hand side of equation 4.3 is also set to zero).

$$J = \frac{e\hbar n}{\tau(n)} \tag{4.12}$$

where J is the current density (A cm^{-2}) and all the other parameters have been described above.

The term 'mode' has been used here to denote finite wavelength ranges, $\Delta\lambda$, that represent the photon densities associated with the allowed cavity modes that lie within these ranges. The phase dependence of these modes is not incorporated in this model, so it is implicit therefore, that within each of the wavelength ranges there is always an allowed cavity mode available for both the individual laser sections and the coupled-cavity.

4.6 Coupled-cavity simulations

The rate equation model described in the previous section has been used to simulate the behaviour of the coupled-cavity device to provide further analysis of the experimental results and also investigate how the coupled-cavity sensing effect can be optimised.

4.6.1 Coupling of spectrally misaligned laser sections

The nature of the coupling that occurs between two spectrally misaligned laser sections (as in sample T2 in figures 4.6 and 4.9) has been investigated by modelling a coupled-cavity device with unequal laser section lengths of $L_1 = 1000 \mu\text{m}$ and $L_2 = 600 \mu\text{m}$, see figure 4.11.

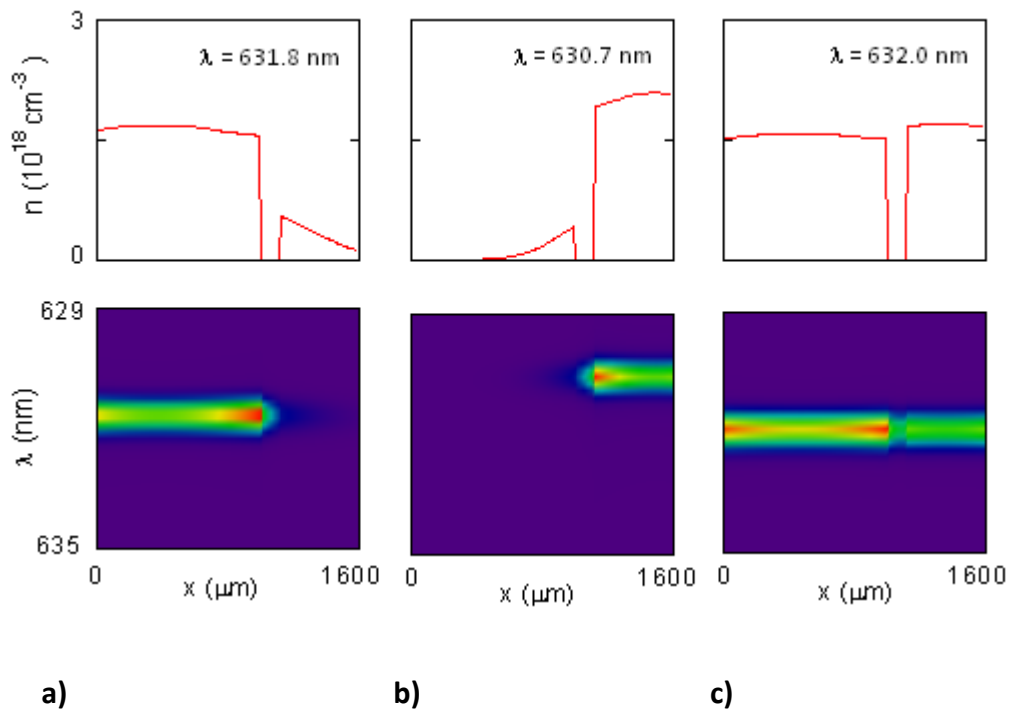


Figure 4.11 (top) Spatial carrier density distributions **(bottom)** spectral versus spatial photon density distributions for a simulated coupled-cavity device with $L_1 = 1000 \mu\text{m}$, $L_2 = 600 \mu\text{m}$ and $L_g = 120 \mu\text{m}$ for: **a)** $J_1 = 1230 \text{ Acm}^{-2}$, **b)** $J_2 = 1230 \text{ Acm}^{-2}$ and **c)** $J_1 = J_2 = 1230 \text{ Acm}^{-2}$. **Inset top** Peak wavelengths. The spectral resolution of the colour maps is 0.167 nm and the colours are auto scaled for each different plot so that red corresponds to the largest value of photon density and purple to the smallest value.

Comparing the carrier density distributions for each of the individual laser sections driven alone (figures 4.11 (a) and (b) top), it is clear that the shorter section requires a higher carrier density to achieve laser action and therefore lases at a shorter wavelength due to the carrier density dependence of the spectral gain peak. Optical pumping effects are also evident here in the finite carrier densities that accumulate in each of the opposing electrically un-pumped sections.

When both sections are driven together with the same current density (figure 4.11 (c)), the higher carrier density in section 2 provides positive gain to the longer wavelength light injected into it from section 1, whereas, the shorter wavelength light from section 2 is absorbed on passing into section 1. The longer wavelength modes experience greater net round trip gain therefore and the carrier density in section 2 is reduced due to the photons injected from section 1. Section 2 no longer provides enough gain to support individual cavity modes, but does provide enough gain for the longer wavelength light from section 1 to pass through section 2 and reflect from the outer cleaved facet and back into section 1. This additional optical feedback effectively lowers the threshold requirement of the coupled-cavity allowed modes and the device shifts to an even longer wavelength as a result (this behaviour is evident in the laser spectra of the device T2 (4 + 14), see figure 4.6).

The lasing modes of a spectrally misaligned coupled-cavity device therefore behave somewhere between 'true' coupled-cavity modes, where the lasing mode is resonant in each of the laser sections and phase matched between them and an external feedback coupled-cavity laser where the shorter section is operated below threshold [3, 4]. In both of these cases however, a shift to longer wavelength signifies a lowering of the threshold requirement of the lasing mode. This implies that, for the purposes of coupled-cavity sensing, because the lasing mode is defined across the full length of the coupled-cavity it will still be sensitive to the degree of coupling between the two laser sections. The size of the wavelength shift however, does depend on the degree of spectral misalignment (the laser spectra of the more closely aligned laser sections of T2 (9 + 19) (see figure 4.9) exhibit a much larger wavelength shift than T2 (4 + 14)).

4.6.2 Optimisation of cavity lengths

The change of the threshold gain requirement that results from operating the device as a coupled-cavity, changes both the operating wavelength and output power for a given input current density. The rate equation model has been used to investigate how, for the symmetrical device i.e. equal laser section lengths, the sensitivity of the coupling mechanism can be maximised by optimising the length of the individual laser sections.

In section 1.4.2 the threshold gain model was used to demonstrate that, the ratio of the threshold gain requirements of the coupled-cavity, and those of the individual cavities, is independent of cavity length. This interpretation however, does not account for the effects of a non-linear gain medium. The ratio of the output power of the coupled-cavity device, with the finite gap loss, compared to that of the individual laser sections (infinite gap loss), for equal current density, has been plotted over a range of different cavity lengths, see figure 4.12.

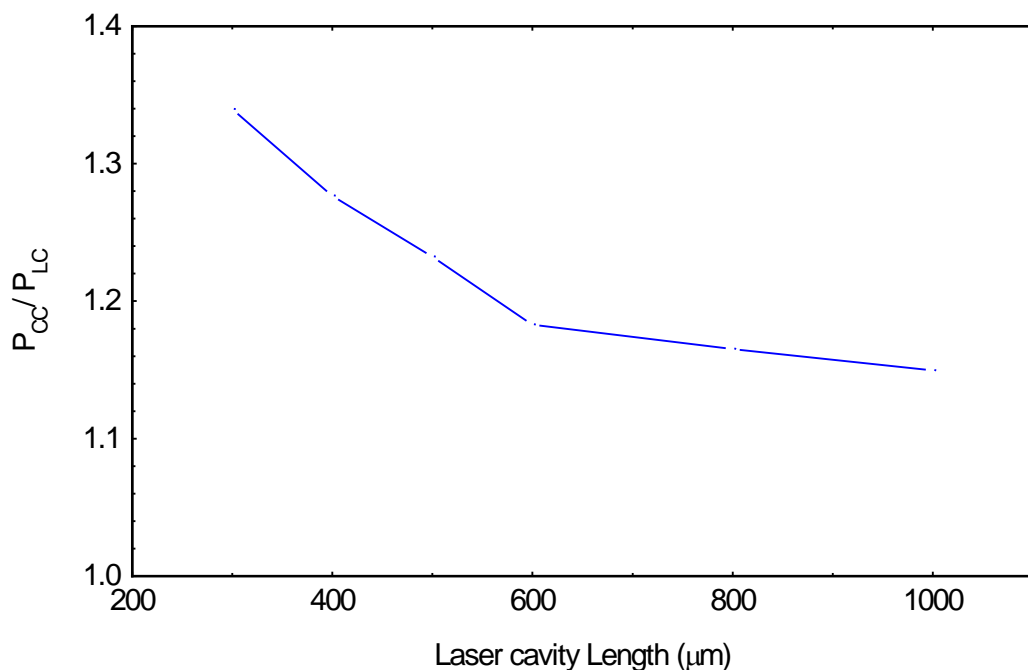


Figure 4.12 The ratio of the power output from the coupled-cavity P_{cc} and the individual laser cavities P_{Lc} each operated at the same current density equivalent to 1.1 times the individual cavity threshold value for a range of different laser cavity lengths.

Figure 4.12 demonstrates that the difference between the output power of the coupled-cavity and that of the individual laser sections increases as the cavity length is reduced, until eventually the gain medium can no longer provide enough gain for the individual cavities to lase on their own. Due to the non-linearity of the gain medium, an optimum cavity length for the individual laser sections can be calculated (assuming fixed cavity losses) [6]. Using the gain data presented in figure 4.11 the optimum cavity length has been calculated for a device with one cleaved and one etched facet as $L_c = 460 \pm 10 \mu\text{m}$, see figure 4.13

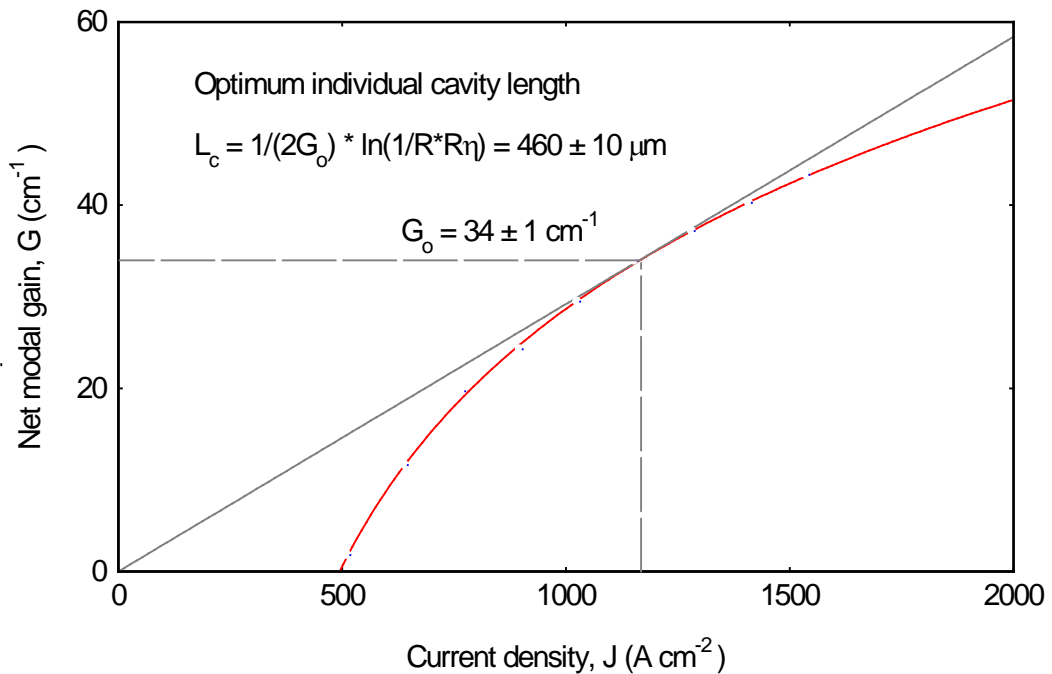


Figure 4.13 The optimum cavity length for the individual laser sections corresponding to the point on the gain current curve where the gain is maximised for the minimal threshold current [6].

For cavity lengths that are shorter than this optimum value, the gradient of the gain - current density curve becomes increasingly small due to gain saturation. A small difference in the threshold gain requirements of the coupled-cavity and individual cavity modes in this region produces a relatively large change in the threshold current density of the device. For a fixed input current this results in a large change

in output power (1.34 times more power for the device with cavity lengths of $L_c = 300 \mu\text{m}$, see figure 4.12). As the cavity length is increased, the device begins to operate in the region below the optimum point, the reduction in threshold gain requirement of the coupled-cavity modes has less of an effect here and the power ratio tends towards unity. For optimal performance as a sensor therefore, the laser cavities of the device should be kept as short as possible while still maintaining the capacity to lase as individuals. Alternatively, the device could be optimised by using a material with a more saturated gain spectrum e.g. quantum dots, or, by reducing the optical confinement factor.

4.7 Summary

When operating the MFCC device in source/detector mode the photocurrent generated in the detector section can be used to measure the light – current characteristics of the source section, indicating the coupling of optical power between the two. When operating both laser sections together the threshold current density of the device is lower than when each of the independent laser sections is driven alone. The device output also shifts to longer wavelength in this case which indicates that the reduction in threshold current density is due to a lowering of the threshold gain requirement of the lasing mode and demonstrates therefore that the device is lasing as a coupled-cavity. A spectral shift of $\Delta\lambda = 20 \pm 5$ Å can be induced in the output of the coupled-cavity by placing a scattering object between the two laser sections demonstrating the potential of the coupled-cavity sensing mechanism.

A multi-mode travelling wave rate equation model has been introduced and used to demonstrate that, in a spectrally misaligned device, coupled-cavity modes can still form that have lower threshold gain requirements than the modes of the individual laser sections of the device. The model has also been used to predict that, for symmetrical devices, the coupled-cavity sensing mechanism can be optimised by reducing the individual laser cavity lengths to the minimum necessary in order to achieve laser action. For a simulated device with 300 µm long laser sections the coupled-cavity output power is 1.34 times larger than the individual laser cavity output power for the same input current density.

References

- [1] Y. L. Wong and J. E. Carroll "A Travelling-wave Rate Equation Analysis for Semiconductor Lasers", *Solid-State Electronics* Vol. 30, No. 1, p. 13, 1987.
- [2] L. A. Coldren and T. L. Koch "Analysis and Design of Coupled-Cavity Lasers – Part II: Transient Analysis", *IEEE Journal of Quantum Electronics*, Vol. 20, No. 6, p.671, 1984.
- [3] G. P. Agrawal and N. K. Dutta "Long-wavelength semiconductor lasers", Van Nostrand Reinhold Electrical/Computer Science and Engineering Series, 1986.
- [4] L. A. Coldren and T. L. Koch "Analysis and Design of Coupled-Cavity Lasers – Part 1: Threshold Gain and design Guidelines", *IEEE Journal of Quantum Electronics* Vol. 20, No. 6, p.659, 1984.
- [5] A. P. Agrawal "Coupled-Cavity Semiconductor Laser under Current Modulation: Small- Signal Analysis", *IEEE Journal of Quantum Electronics*, Vol. 21, No.3, p.255, 1985.
- [6] P. W. A Mc Ilroy, A Kurobe and Y. Uematsu "Analysis and Application of Theoretical Gain Curves to the Design of Multi-Quantum-Well Lasers", *IEEE Journal of Quantum Electronics*, Vol. 21, No. 12, p.1958, 1985.

Chapter 5:

Wavelength tuning and self-pulsation

5.1 Introduction

The micro-fluidic coupled-cavity device described in chapter 2 is ultimately intended for use as a biological cell sensor. This requires that the gap coupler, the “sensing section” of the device, must be wide enough to accommodate the free passage of cells with diameters as large as 10 - 20 μm . The need for such a large gap coupler restricts the coupling strength that can be achieved between the two laser sections which ultimately limits the potential sensitivity of the device. Furthermore, the results presented in chapter 4 demonstrated that a relatively small difference in the threshold carrier densities of the two laser sections can further reduce the sensitivity of the coupled-cavity sensing mechanism due to spectral misalignment.

This chapter presents the results of an investigation into the utility of including a segmented electrical contact to one of the laser sections of the coupled-cavity design. This modification would allow the wavelength of this section to be tuned with respect to that of its neighbour, establishing an extra degree of control over the coupling between them. Wavelength tuning has been demonstrated in segmented contact quantum well lasers using the “gain leveraging” effect [1, 2]: differential forward bias is employed to manipulate the average carrier density inside the device influencing the lasing wavelength. A further advantage of the segmented contact design is that non-uniform current injection can be used to

induce self-pulsation by passive Q-switching [3]. Self-pulsed lasers are of interest as stroboscopic excitation sources for cell imaging [4].

Section 5.2 presents lasing spectra and light – current (L - I) curves measured for a segmented contact quantum well laser with a total tuning range of 1.2 ± 0.2 nm. Although this tuning range is not large, it is sufficient to demonstrate the general tuning behaviour of the device and establish the input parameter combinations that represent the limits of the tuning range. Analysis of the experimental results has been carried out using the multimode travelling wave rate equation model that was introduced in chapter 4. In section 5.3 the self-pulsation behaviour of the segmented contact device has been investigated as a function of gain section injection current and of absorber section reverse bias. The reverse bias net modal absorption spectra have been measured using the multi-section technique that was described in section 3.2. These spectra have been used to modify the gain functions of the rate equation model so that it can be used to simulate the self-pulsation behaviour of segmented contact devices as a function of reverse bias.

5.2 Wavelength tuning in segmented contact quantum well lasers

Like the multi-section device used for gain characterisation in section 3.2, the tuneable wavelength device illustrated in figure 5.1 also features a 50 μm oxide stripe contact system that has been patterned into electrically isolated segments. In this case however, the device has only two segments, the inter-contact resistance of which is $(450 \pm 10) \Omega$. The overall device length, L , is $(1000 \pm 2) \mu\text{m}$ and the individual sections S_1 and S_2 have a length ratio of 4:1. The left hand facet, with reflectivity R_1 , is formed by cleaving and the right hand facet, with reflectivity R_2 , has been etched using the process described in section 2.4.1. In all experiments the light output has been collected from the cleaved facet.

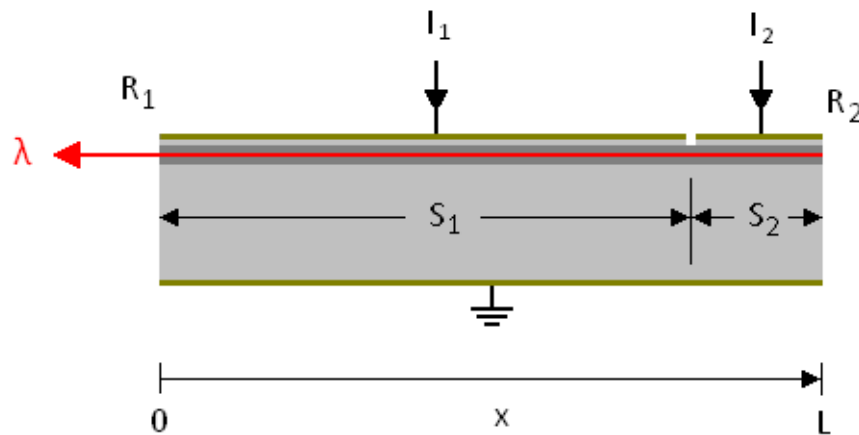


Figure 5.1 Device geometry of the segmented contact laser used for wavelength tuning.

In previous work on wavelength tuning in gain-levered quantum well lasers, the tuning behaviour has been attributed to the carrier density dependence of the refractive index [5]. In an evenly pumped laser, the average carrier density pins once the device reaches threshold and so, therefore, does the lasing wavelength. In a gain-levered device however, the average carrier density above threshold can be varied by changing the relative proportions of the forward bias across each of the device segments (this is a consequence of the fact that the gain in a quantum well laser is a non-linear function of the carrier density). A change in the level of forward bias in either section therefore, alters the average carrier density of the device

which, due to the carrier density dependence of the refractive index, produces a corresponding shift in the longitudinal mode spectrum, see equation 1.12.

While the manipulation of the average carrier density does undoubtedly shift the longitudinal mode spectrum in this way, the experimental and simulated device results presented in this chapter demonstrate that, for the AlGaInP quantum well devices used in this work, the majority of the wavelength tuning behaviour can be accounted for by the carrier dependence of the peak modal gain spectrum. In the steady-state, the wavelength of a laser corresponds to the longitudinal mode that experiences the highest net round-trip gain. In an evenly pumped laser this means that the wavelength of the device is approximately coincident with the peak of the gain spectrum. In the gain-levered device however, because the carrier density distribution along the length of the cavity is highly non-uniform, the average single pass gain experienced by a mode with wavelength λ , must be summed over the full length of the cavity:

$$g_{\lambda} = \frac{1}{L} \int_{x=0}^{x=L} g(n_x, \lambda) dx \quad (5.1)$$

Assuming that the carrier density through each of the sub-sections is approximately uniform, then equation 5.1 can be expressed as

$$g_{\lambda} \cong \frac{1}{L} [g(n_1, \lambda)S_1 + g(n_2, \lambda)S_2] \quad (5.2)$$

where n_1 and n_2 are the average carrier densities of sections 1 and 2 respectively. The wavelength of the mode that experiences the greatest net round trip gain therefore, will correspond to the maximum value of equation 5.2, giving the condition

$$\frac{S_2}{L} \cdot \frac{d}{d\lambda} g(n_2, \lambda) = - \frac{S_1}{L} \cdot \frac{d}{d\lambda} g(n_1, \lambda) \quad (5.3)$$

In other words, the wavelength of the lasing mode in the gain-levered device can be approximated as the point where the gradients of the section-length weighted gain spectra of each section are equal in magnitude i.e. not at the peak of either of the sections individually.

The gain in a quantum well laser is a non-trivial function of both wavelength and carrier density. Nevertheless, it can be measured experimentally and treated phenomenologically. However, to solve equations 5.1 - 5.3 requires knowledge of the average carrier density in each section. The carrier density is not simply proportional to the current injection in each section, it is fundamentally coupled to the photon density throughout the device; as photons generated in one section travel into to the other energy is exchanged between the two via the generation and recombination of the charge carriers. In order to model the wavelength tuning behaviour of the twin segment device therefore, the coupled carrier and photon densities must be solved for simultaneously at all points along the length of the cavity. This has been done numerically using the multi-mode travelling wave rate-equation model that was introduced in section 4.5.

The wavelength tuning behaviour of the segmented contact device has been characterised by measuring both the L - I characteristics and lasing spectra as a function of differential forward bias. In each case, the two sections of the device are driven individually with an independent current source, generating current densities in the range $J_1 \geq J_2 \geq 0$. Analysis of the experimental results has been carried out by simulating the experimental data using the rate equation model. The same model parameters have been used for these simulations as were introduced in section 4.5 and the section lengths have been chosen to approximate the device illustrated in figure 5.1. Having achieved a good qualitative agreement between the experimental and simulated devices, the model has been used to demonstrate how the wavelength tuning range can be optimised.

5.2.1 Wavelength tuning results

Figures 5.2 and 5.3 are the lasing spectra for the experimental and simulated segmented contact devices respectively.

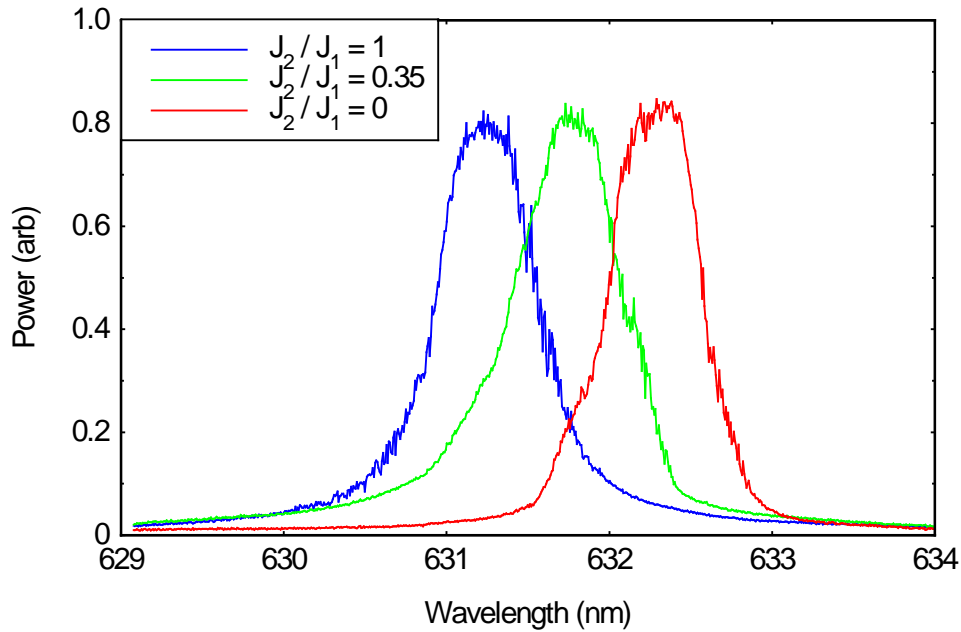


Figure 5.2 Lasing spectra of the experimental segmented contact device for section 1 current densities: 970 A cm^{-2} (blue line), 1077 A cm^{-2} (green line) and 1346 A cm^{-2} (red line).

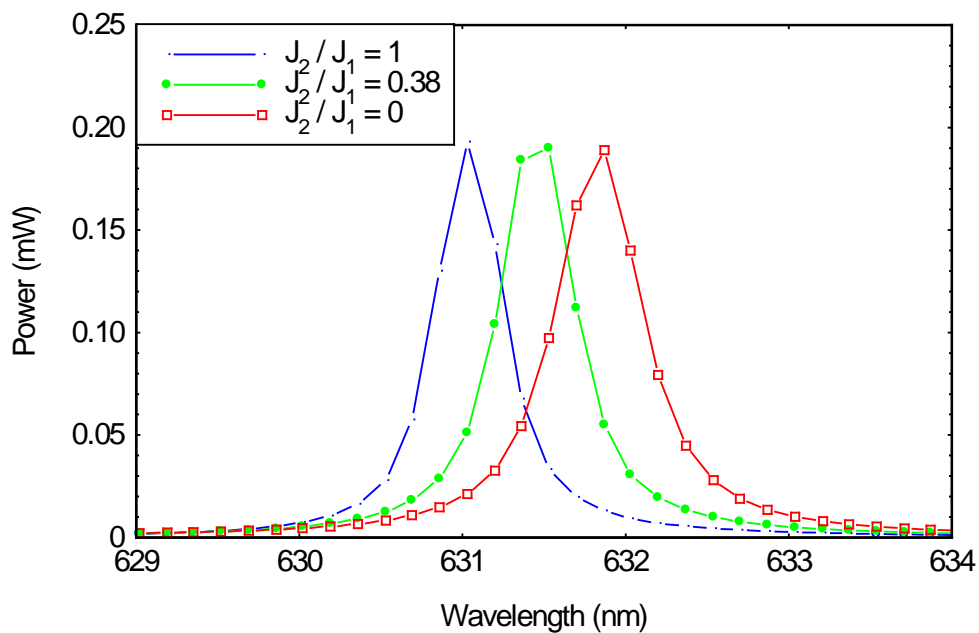


Figure 5.3 Lasing spectra of the simulated segmented contact device with section 1 current densities of: 907 A cm^{-2} (blue circles), 1115 A cm^{-2} (green circles) and 1298 A cm^{-2} (red squares).

Figures 5.4 and 5.5 are the L – I characteristics for the experimental and simulated segmented contact devices respectively.

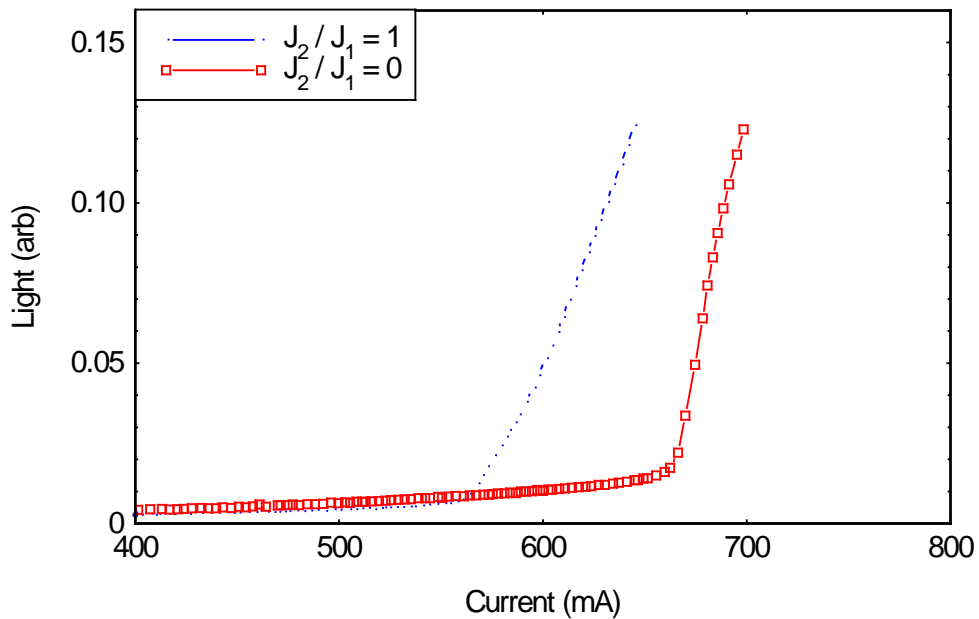


Figure 5.4 L - I characteristics of the experimental segmented contact device for section 2: forward biased (blue circles) and floating (red squares).

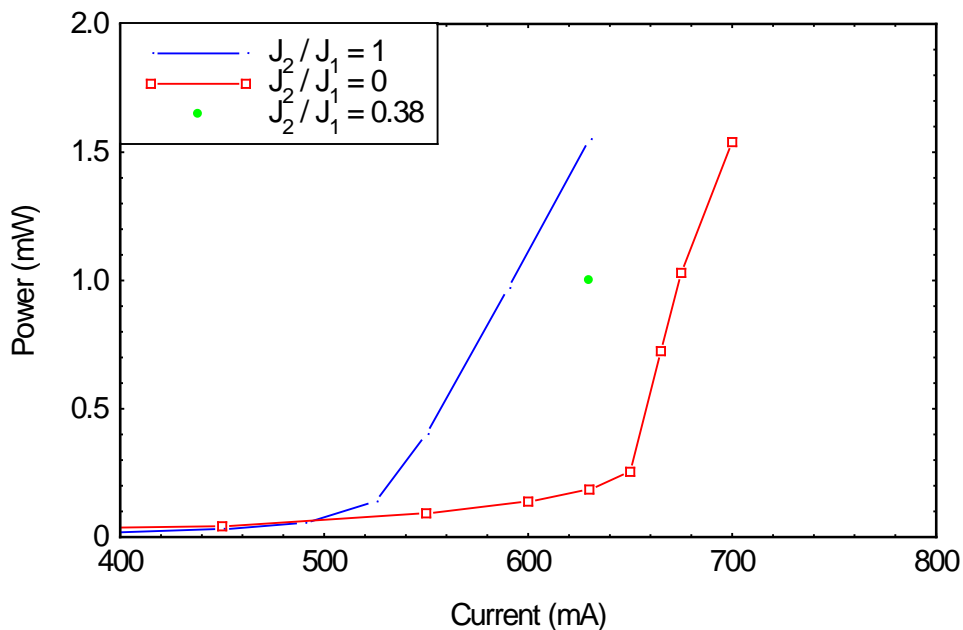


Figure 5.5 L - I characteristics of the simulated segmented contact device for section 2: forward biased (blue circles) and floating (red squares). The total current used to plot the intermediate lasing spectrum in figure 5.3 (current density ratio of 0.38), has also been plotted for comparison (green circle).

The wavelength tuning ranges demonstrated in the lasing spectra in figures 5.2 and 5.3 for the experimental and simulated devices are (1.1 ± 0.2) nm and (0.9 ± 0.2) nm respectively. Although the simulated tuning range is slightly shorter than that of the experimental device, they agree within errors.

The $L - I$ characteristics of the experimental and simulated devices show good qualitative agreement. The threshold currents of the experimental device are slightly higher than those of the simulated device however. When section 2 is left floating the threshold current and the above threshold gradient are both larger than when the device is evenly pumped. When the device initially turns on, the unpumped section is still operating as an absorber which increases the round trip cavity loss. As the current in section 1 is increased the additional optical power that results effectively reduces the cavity losses by optically pumping section 2. By comparison with the evenly pumped laser, where the cavity losses remain constant, a small increase in input current now yields a much larger increase in output power.

5.2.2 Wavelength tuning analysis

Analysis of the wavelength tuning behaviour has been carried out using the carrier density distributions generated for the simulated lasing spectra, see figure 5.6.

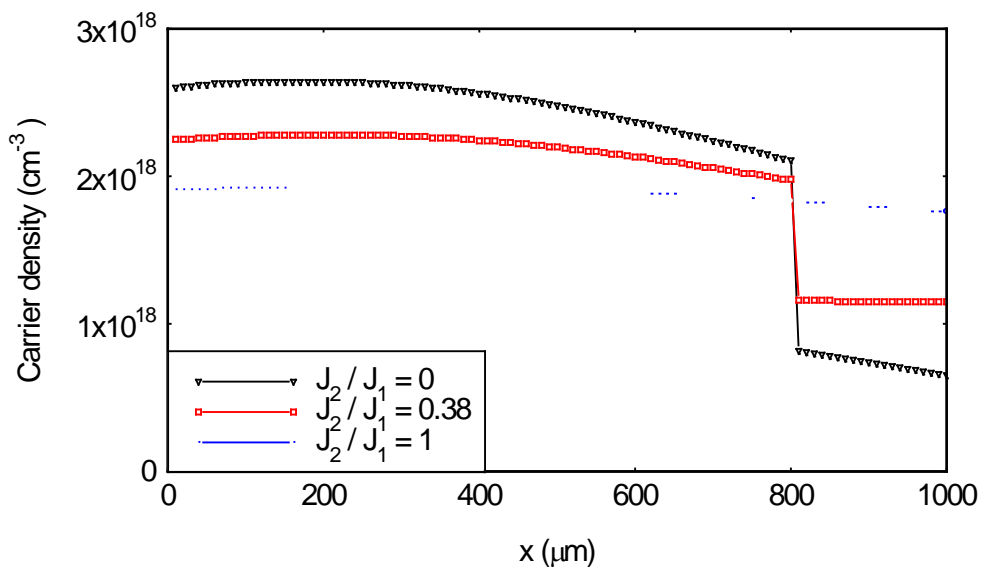


Figure 5.6 Spatial carrier density distributions along the length of the simulated device cavity corresponding to the lasing spectra presented in figure 5.3.

For each of the carrier density distributions plotted in figure 5.6, an average value for sections 1 and 2 has been used to calculate an associated “average” net modal gain spectrum for that section. These gain spectra have been plotted against one another along with the corresponding peak net round trip gain value (calculated using equation 5.2) to demonstrate the behaviour of the device for each case.

Case 1 ($J_1 = J_2$) the short wavelength tuning limit

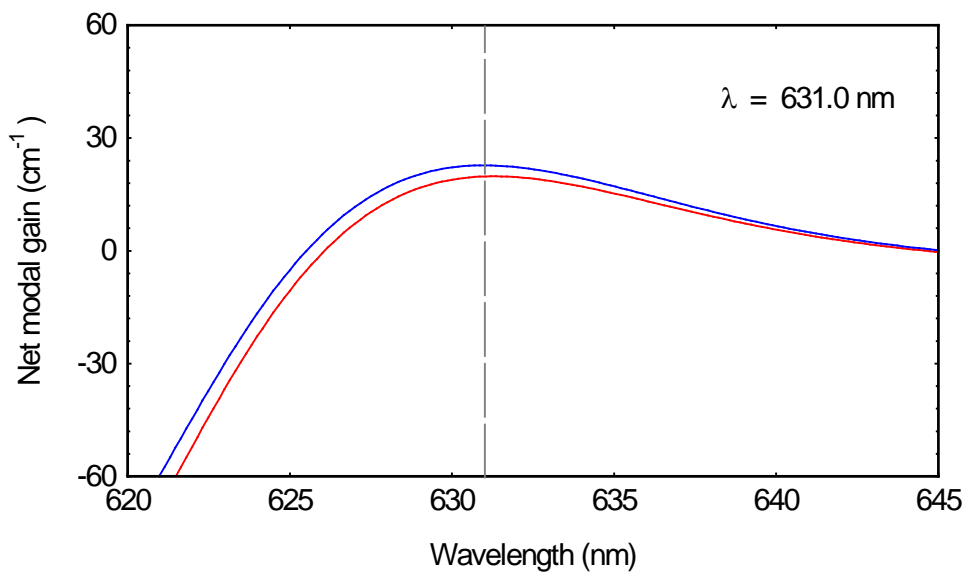


Figure 5.7 Average net modal gain spectra for section 1 (blue line) and section 2 (red line) for equal current density injection to each section. The wavelength of the net round trip gain maximum is indicated by the dashed grey line (numerical value inset).

Even though both sections are evenly pumped, the average carrier densities in each of the sections are not equal. This is because the photon distribution along the length of the cavity is non-uniform due to differing mirror losses of the cleaved and etched facets. Nevertheless, the peaks of the net modal gain spectra corresponding to each section (see figure 5.7) are approximately coincident and so, therefore, is the net round trip gain maximum. This case represents the short wavelength tuning limit of the device.

Case 2 ($J_1 > J_2 > 0$) the active gain-lever range

By lowering the current density in section 2, the peak of the net modal gain spectrum shifts towards longer wavelengths as the average carrier density in the section is reduced. In order to maintain laser action, the current density in section 1 must be increased to compensate for the loss of gain from section 2. As the gain increases in section 1, the gain peak shifts towards shorter wavelengths, cancelling somewhat the long wavelength shift of section 2. Nevertheless, as the gain in section 1 tends towards saturation, this short wavelength shift becomes less and less significant. This factor, combined with the asymmetry of the gain spectra (as expressed in equation 5.3) results in a net shift towards longer wavelength.

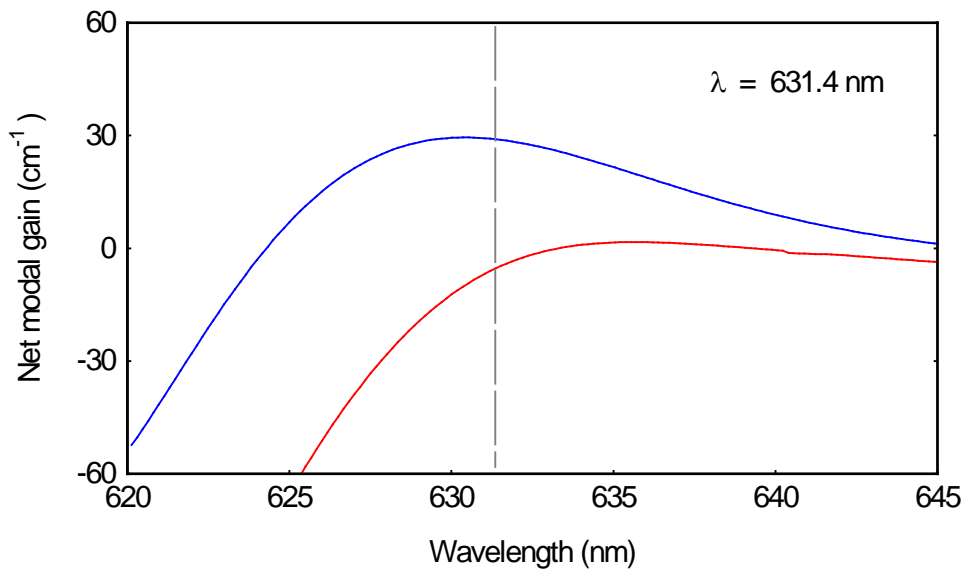


Figure 5.8 Average net modal gain spectra for section 1 (blue line) and section 2 (red line) for the active gain-lever case ($J_1 > J_2 > 0$). The peak net round trip gain (dashed grey line) has shifted to longer wavelength due to the non-uniform carrier density distribution.

Judicious tweaking of the currents in sections 1 and 2 allows the wavelength of the laser to be tuned continuously between the long and short wavelength limits of the tuning range while, at the same time, maintaining a constant power output at the cleaved facet.

Case 3 ($J_2 = 0$) the long wavelength tuning limit

When section 2 is left as an open circuit, the point at which the laser turns on represents the long wavelength tuning limit of the device. Increasing section 1 forward bias, tunes the lasing wavelength back towards shorter wavelengths as it optically pumps section 2. Eventually section 2 becomes transparent at the lasing wavelength and the L-I characteristic of the device will converge with that of the evenly pumped laser. Figure 5.9 demonstrates this tuning behaviour - to reach transparency in section 2 with this particular device geometry, requires an unfeasibly large current density of 9615 A cm^{-2} , this equates to a section 1 current of 5 amps. When section 2 is pumped to transparency, the carrier densities must pin, and so no further wavelength change can occur. There is still a disparity between the carrier densities at this point however, so the wavelength is not tuned all the way back to the short wavelength limit of the evenly pumped cavity: case 1.

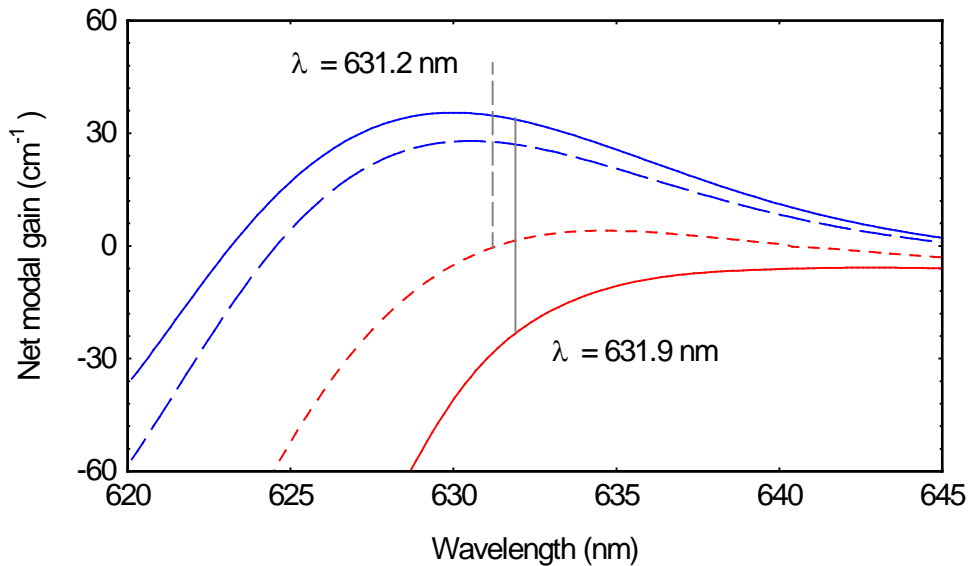


Figure 5.9 Average net modal gain spectra for section 2 floating and a section 1 current density of: 1298 A cm^{-2} (solid red and blue lines) and 9615 A cm^{-2} (dashed red and blue lines).

5.2.3 Optimisation of the tuning range

The analysis of the wavelength tuning behaviour developed with the rate equation simulations above, has been applied to define a set of general design principles to maximise the tuning range in the segmented contact device.

1. The optimum section length ratio is $S_1/S_2 = 1$. When section 2 is un-pumped, this ratio creates the largest average carrier density differential between the two sections and with it, the largest wavelength difference between the peaks of the gain spectra in each section.
2. The total cavity length should be minimised. This condition ensures that the gain in section 1 is close to saturation for the case when section 2 is floating, consequently the long wavelength tuning limit is maximised by reducing the short wavelength shift of section 1.
3. The lower cavity length limit is set by the requirement that the device is still able to achieve threshold when section 2 is floating. If the gain is too close to saturation in section 1 it will not be able to overcome the losses experienced in the un-pumped section and the device will not lase.

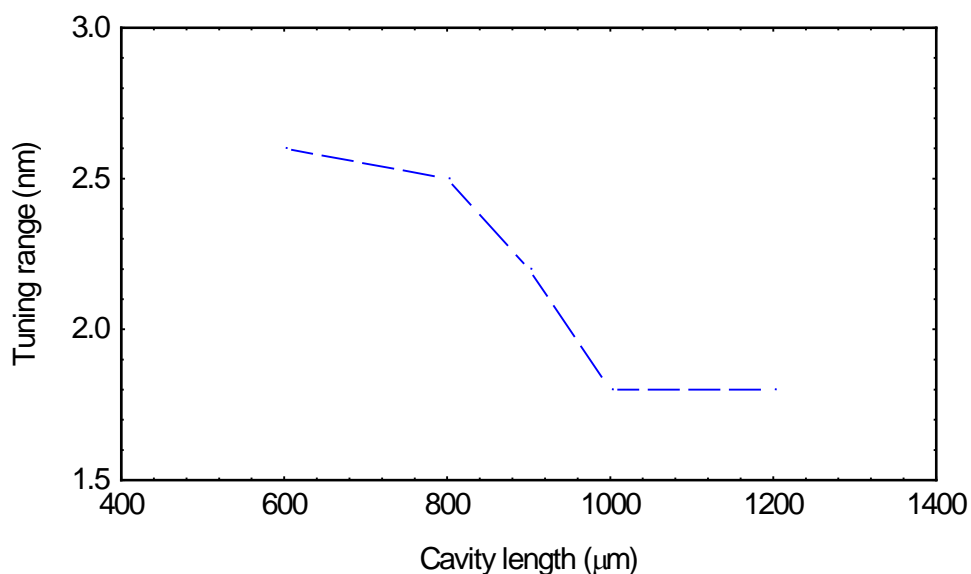


Figure 5.10 Optimisation of the cavity length for a device with a section length ratio $S_1/S_2 = 1$.

5.3 Self-pulsation

This section presents the results of an investigation into the self-pulsation behaviour of the segmented contact device described in section 5.2. The segmented contact system can be used to create a saturable absorber region within one of the laser sections of the coupled-cavity that can be used to induce self-pulsation by passive Q-switching. Grounding the absorber section provides an additional non-radiative recombination path for electron – hole pairs, reducing the carrier lifetime in the section and shortening the absorber recovery time. By applying a reverse bias electric field, the recovery time of the absorber section is further reduced as the carriers are now swept away more quickly [6]. Reverse biasing not only affects the recovery time of the absorber section, it also changes the magnitude and spectral distribution of the absorption in that section due to the quantum confined Stark effect [7].

Self-pulsation in the segmented contact device has been inferred by measuring the saturable absorption (the minimum requirement for self-pulsation) exhibited in the $L - I$ characteristics of the device while the absorber section is grounded and also when a reverse bias has been applied. Following the same approach as in section 5.2, analysis of this experimental behaviour has been carried out using rate equation simulations. To accurately model the change in the magnitude and spectral distribution of the absorption when reverse bias is applied, net modal absorption spectra have been measured for a range of reverse bias voltages. These experimental data have then been used to modify the gain fitting functions of the model following the procedure that was described in section 4.5.2. The reverse bias dependence of the absorber section recovery time has been modelled by varying the non-radiative carrier lifetime used in the model.

5.3.1 Net modal gain spectra as a function of reverse bias

In section 3.2 the net modal absorption spectrum was calculated using amplified spontaneous emission (ASE) spectra measured with the absorbing section grounded. Here, reverse bias net modal absorption spectra have been calculated using ASE measured with reverse bias applied across the absorbing section. The results have been plotted as negative net modal gain spectra in figure 5.11 alongside the net modal gain data that was previously presented in figure 3.4.

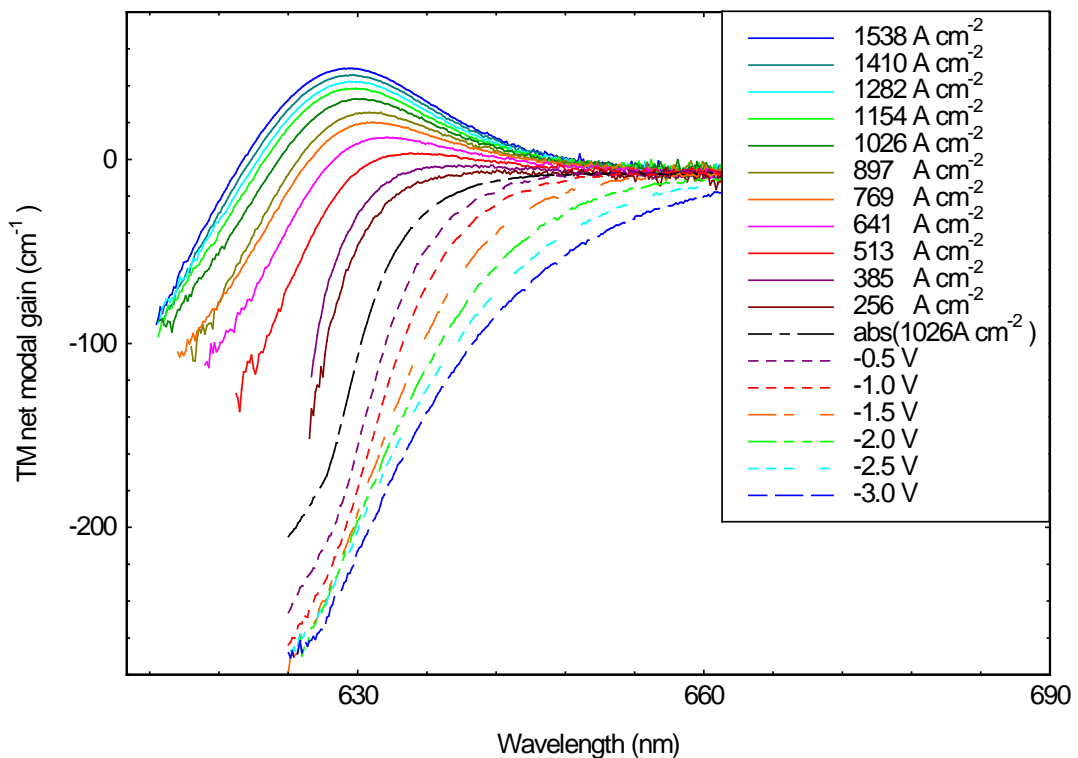


Figure 5.11 TM net modal gain spectra plotted as a function of current density (solid lines) and as a function of reverse bias (dashed lines) for a GaInP/AlGaInP SQW device.

As the level of reverse bias increases from 0 V to 3 V the position of the band edge can be seen to move to longer wavelengths. Furthermore the magnitude of the absorption at longer wavelengths increases steadily with increasing reverse bias, while at shorter wavelengths the absorption changes far less rapidly. This distortion of the spectral absorption is due to the quantum confined Stark effect induced by the reverse bias E-field [7].

5.3.2 L – I characteristics with reverse bias

Figures 5.12 and 5.13 present the L – I characteristics for the experimental and simulated devices respectively for various section 2 reverse biases.

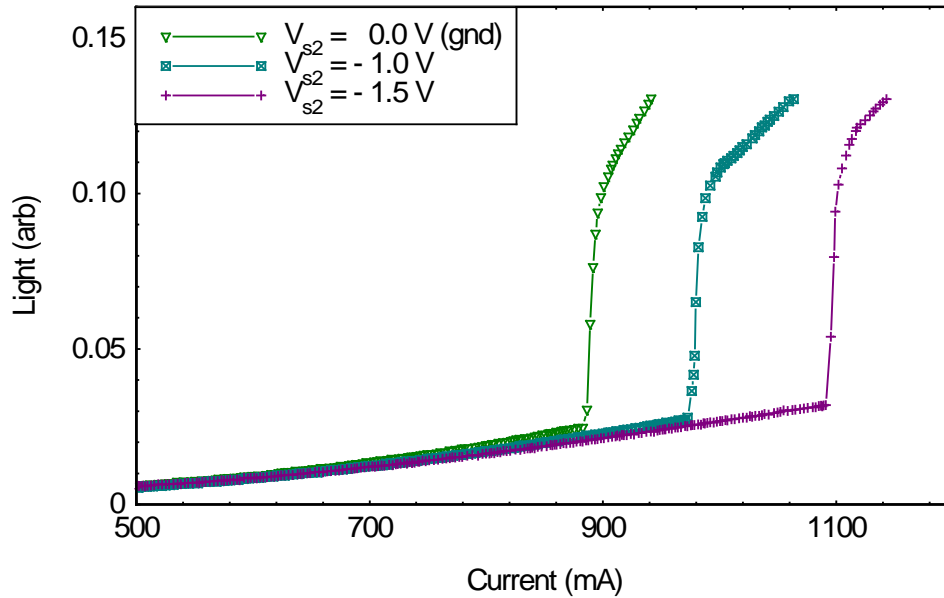


Figure 5.12 Light – current curves for section 2: grounded (green diamonds) and reverse biases of: 1.0 V (blue squares) and 1.5 V (purple circles).

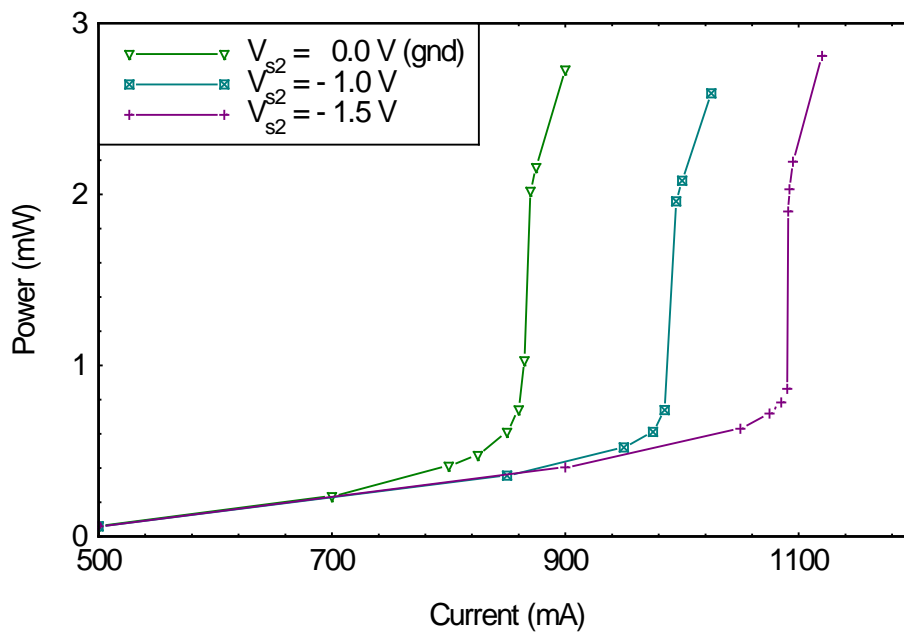


Figure 5.13 Simulated light – current curves for section 2: grounded (green diamonds) and reverse biases of: 1.0 V (blue squares) and 1.5 V (purple circles).

The simulated L-I curves have been generated by summing the spectral power output of the model and then averaging this total power over one complete self-pulsation period. For input current values that did not result in self-pulsation, the spectral sum was taken at a point in time when the device output had reached a steady-state.

The L – I curves for the experimental and simulated devices, plotted in figures 5.12 and 5.13 respectively, show good qualitative agreement. Both exhibit the characteristic kink associated with saturable absorption [8]. This behaviour is clear evidence of saturable absorption, the passive Q-switching mechanism by which self-pulsation is induced in diode lasers. This is a strong indication that self-pulsation can be induced in the experimental device. A fact that is further reinforced by the self-pulsation that is observed in the simulated device output presented in the following section.

5.3.3 Self-pulsation analysis

Analysis of the self-pulsation behaviour of the segmented contact device as a function of reverse bias has been carried out using simulated data generated using the rate equation model. To demonstrate how self-pulsation evolves in the segmented contact device, simulated time dependent lasing spectra have been plotted in figure 5.14 for different gain section input currents.

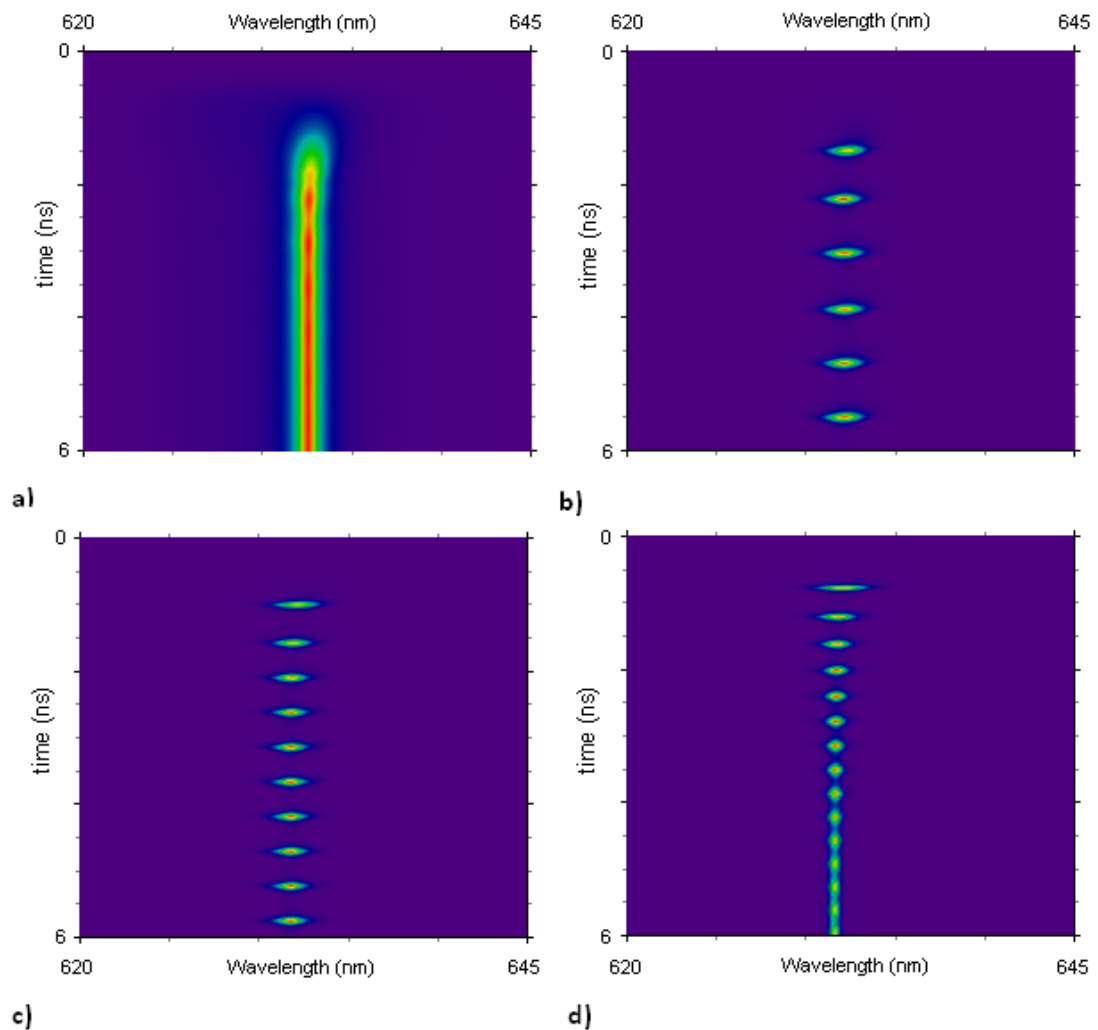


Figure 5.14 Time dependent lasing spectra for the simulated device with section 2 grounded and section 1 driven at current s of; a) 865 mA (steady-state lasing just above threshold); b) 875 mA (self-pulsing at 1.27 GHz); c) 925 mA (self-pulsing at 1.98 GHz) and d) 975 mA (prolonged relaxation oscillations tending towards steady-state lasing). The spectral resolution of the colour maps is 0.167 nm and the colours are auto scaled for each different plot so that red corresponds to the largest value of photon density and purple to the smallest value.

When the device is driven just above threshold, after some initial, faint, relaxation oscillations, the light output settles into continuous steady-state lasing. A relatively small increase in drive current of 10 mA is enough to increase the size of the initial turn-on pulse to the point where the absorber becomes partially saturated and self-pulsation occurs. Increasing the current still further reduces the initial turn-on delay which consequently increases the frequency of the self-pulsation. Eventually, at higher currents, the initial pulse is so large that the frequency increases to the point that the absorber cannot recover in time and the device settles back into a steady-state lasing regime. In figure 5.15 the frequency of the self-pulsation has been plotted as a function of input current for various biases.

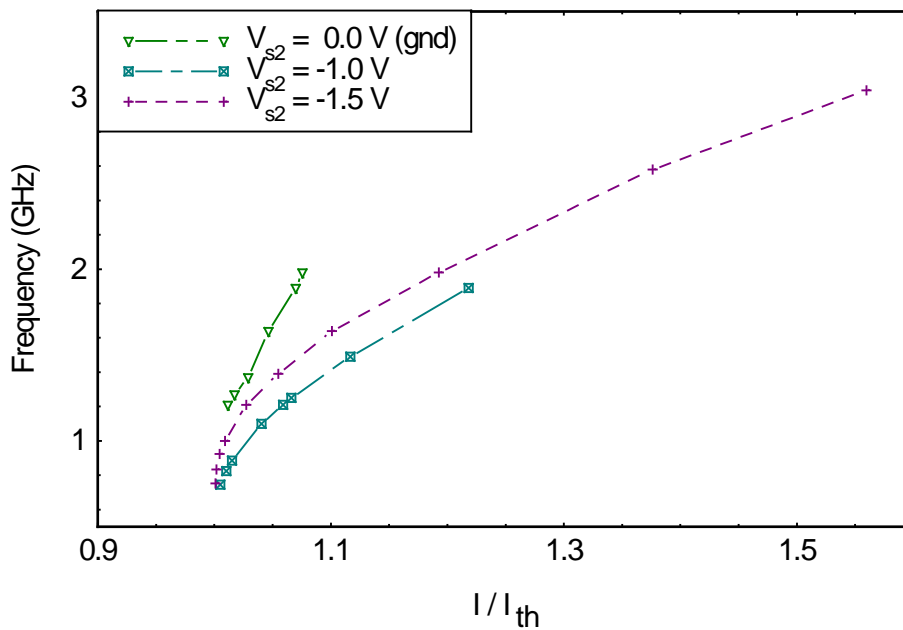


Figure 5.15 Plot of the modelled self-pulsation frequency versus section 1 current as a ratio of the threshold current when section 2 is grounded (green diamonds), and reverse biases of 1.0 V (blue squares) and 1.5 V (purple circles).

When the absorber section is grounded, the self-pulsation frequency can be tuned over a range of 800 MHz. This tuning range can be extended to over 2.3 GHz by applying a reverse bias of 1.5 V. For reverse biases larger than this, the gain section can no longer overcome the absorber section loss and the device ceases to lase. Tuneable self-pulsed lasers are of interest as stroboscopic excitation sources in cell imaging [4].

5.3.4 Frequency tuning with optical pumping

By incorporating a saturable absorber section into the coupled-cavity design, one of the laser sections can be operated as a self-pulsed laser. The self-pulsation frequency could be tuned using the optical injection of higher energy light from the opposing laser cavity. To demonstrate how this might be achieved, the rate equation model has been used to simulate a coupled-cavity device with three separate contacts, an 800 μm long laser section with two equal length contacts to be used to generate self-pulsation coupled across a 120 μm gap to a shorter, 400 μm long laser section used for optical pumping, see inset figure 5.16. The absorber section of the self-pulsed laser is left as an open circuit and the gain section is driven above threshold at $I_1 = 850$ mA. The current in the shorter optical pump section (with a threshold current of $I_{2th} = 315$ mA) is varied and the resulting self-pulsation frequency calculated by measuring the time delay between adjacent pulses of the total power output of the self-pulsed section. This is shown in figure 5.16.

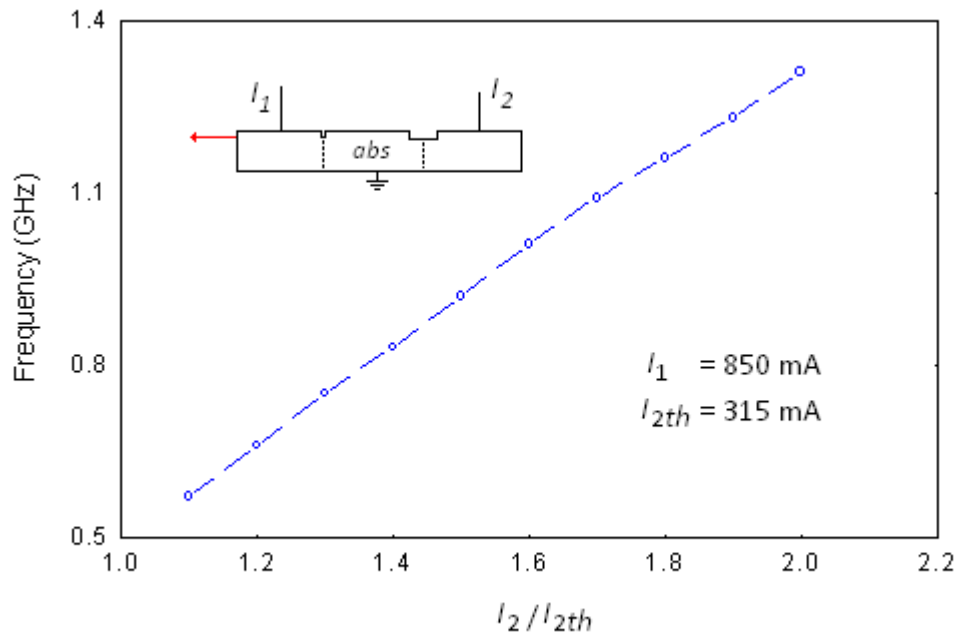


Figure 5.16 Self-pulsation frequency as a function of the optical pump section input current (blue circles). **Inset** Schematic illustration of the three section device geometry.

Optically pumping the absorber section of the self-pulsed laser effectively increases the gain to absorber section length ratio which in turn changes the self-pulsation frequency. The additional degree of control afforded by the optical pump current can, with careful selection of the input currents I_1 and I_2 , be used to tune the frequency of the self-pulsation whilst maintaining a constant peak output power.

5.3.5 Optical pump sensor

The L – I curves for the segmented contact device in section 5.2 showed that when one of the sections is left floating the device has a sharper turn on due to the change in loss that results from the gain section optically pumping the absorber section. This mechanism could be used to amplify the input from the optical pump section of the coupled-cavity in order to make the device more sensitive to gap loss perturbations. The simulated device geometry from figure 5.16 has been used to demonstrate how this mechanism might be employed. If the gain section of the self-pulsed laser is driven just below threshold, the device will only lase if the optical pump section provides enough input. A 10 % increase in the gap loss between the two laser sections is enough to stop the self-pulsation section from lasing at all which dramatically reduces the device output, see figure 5.17.

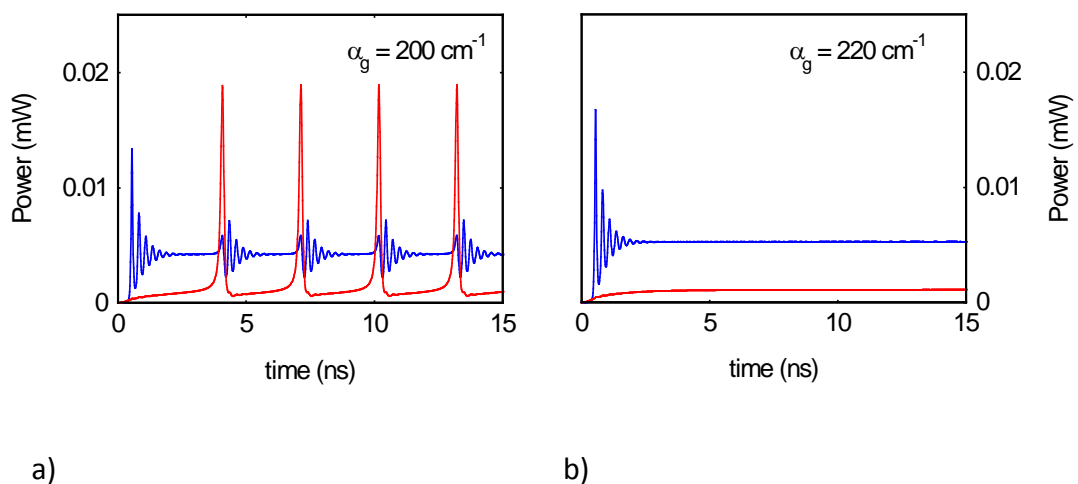


Figure 5.17 Simulated output for the self-pulsed laser (red lines) and the optical pump laser (blue lines) for $I_1 = 800 \text{ mA}$ and $I_2 = 473 \text{ mA}$ for gap losses of a) $\alpha_g = 200 \text{ cm}^{-1}$ and b) $\alpha_g = 220 \text{ cm}^{-1}$.

5.4 Summary

The addition of a segmented contact system to the coupled-cavity device would enable wavelength tuning via the gain lever effect. This facility could be used to spectrally align the laser sections of the coupled-cavity offering an extra degree of control over the coupling between them. Wavelength tuning in gain levered devices has previously been attributed to the longitudinal mode shift brought about by the carrier density dependent refractive index. In this chapter it has been demonstrated that the majority of the tuning effect can be explained by the carrier density dependence of the peak net modal gain spectrum. A wavelength tuning range of $\Delta\lambda = 1.2 \pm 0.2$ nm has been measured for a single cavity laser with a segmented contact length ratio of 4:1. The limits of the gain lever tuning range have been defined in terms of the device input parameters using a rate equation model to simulate the experimental device behaviour. The model has also been used to define a set of design criteria that can be applied to maximise the tuning range of gain levered devices.

The segmented contact system also offers a facility to induce self-pulsation through saturable absorption. The effects of reverse bias on the absorption characteristics of the AlGaInP quantum well material have been measured using the multi-section technique. This data has been used to modify the rate equation gain functions so that the changes in the magnitude and spectral distribution of the absorption, caused by reverse bias, are included in the model. The adapted model has been used to simulate the saturable absorption effects that are observed in the light – current characteristics of the segmented contact device with and without reverse bias. The resulting time dependent spectral output of the simulated device has been used to demonstrate the evolution of self-pulsation with increasing injection current. Using this technique, the input current dependence of the self-pulsation frequency has been studied as a function of reverse bias. The model has also been used to demonstrate how a segmented contact system can be used to amplify the effect of optical coupling within the coupled-cavity laser.

References

- [1] K. J. Vahala, M. A. Newkirk, and T. R. Chen "The optical gain lever: A novel mechanism in the direct modulation of quantum well semiconductor lasers", *Applied Physics Letters*, 54 (25), p.2506, 1989.
- [2] K. Y. Lau "Broad wavelength tunability in gain-levered quantum well semiconductor lasers", *Applied Physics Letters*, 57 (25), p.2632, 1990
- [3] T. Lee and R. H. R. Roldan "Repetitively Q-switched light pulses from GaAs injection lasers with tandem double-section stripe geometry", *IEEE Journal of Quantum Electronics*, Vol QE-6, No. 6, p.339, 1970.
- [4] D. R. Matthews, H. D. Summers, K. Njoh, R. J. Errington, P. J. Smith, P. Barber, S. Ameer-Beg, and B. Vojnovic "Technique for measurement of fluorescence lifetime by use of stroboscopic excitation and continuous-wave detection *Applied Optics* Vol. 45, No. 9, p.2115, 2006.
- [5] K. Y. Lau "Frequency modulation and linewidth of gain-levered two-section single quantum well lasers", *Applied Physics Letters*, 57 (20), p.2068, 1990.
- [6] A. M. Fox, D. A. B. Miller, G. Livescu, J. E. Cunningham and W. Y. Jan "Quantum Well Carrier Sweep Out: Relation to Electroabsorption and Exciton Saturation" *IEEE Journal of Quantum Electronics*, Vol. 27, No, 10 p.2281, 1991.
- [7] A. J. Moseley, D. J. Robbins, A. C. Marshall, M. Q. Kearley and J. I. Davies "Quantum Confined Stark Effect in InGaAs/InP Single Quantum Wells Investigated by Photocurrent Spectroscopy", *Semiconductor Science and Technology* Vol. 4, p. 184, 1989.
- [8] C. R. Mirasso, G. H. van Tartwijk, E. Hernández-García, D. Lenstra, S. Lynch, P. Landais, P. Phelan, J. O’Gorman, M. San Miguel, and W. Elsässer "Self-pulsating semiconductor lasers: theory and experiment", *IEEE Journal of Quantum Electronics*, Vol. 35, No. 5, p.764, 1999.

6.1 Conclusions

This thesis has described the work that has been carried out to investigate the potential of monolithic coupled-cavity semiconductor lasers for bio-sensing applications. This investigation has involved the design and fabrication of a novel micro-fluidic coupled-cavity laser sensor, experimental characterisation of this device and the development of a multi-mode travelling wave rate equation model for the interpretation of device behaviour.

In chapter 1 a threshold gain model was used to demonstrate that facet efficiency plays a key role in determining the nature of the coupling that occurs within the coupled-cavity device. A 50 % reduction in facet efficiency can lower the Q-factor of the gap coupler to the point where the coupling between the lasers can be approximated by the single pass transmission from one laser section to the other, thus minimising the resonant nature of the gap coupler. The fabrication and characterisation of these etched laser facets has been a priority of this work.

The high temperature plasma etching technique that was used to fabricate the etched facets of the prototype device was found to partially anneal the Ni and Cr etch-masks that were initially tested. This made the removal of these masks difficult which was found to reduce the quality of subsequent electrical contacts. By using SiO₂ as an alternative mask material, this issue has been avoided. However, the facets etched using SiO₂ masks have proved susceptible to faceting damage – an inherent plasma etching problem. By using mask thicknesses greater than 300 nm it was found that the damage could be limited to the upper region of the facets beyond the range of the optical mode where it is assumed it does not contribute to a loss of facet efficiency.

Chapter 3 presented a methodology for quantifying the efficiency of etched laser facets using the multi-section gain characterisation technique. This technique has been used to measure the efficiency of the plasma etched facets used in this work to be $\eta = 0.48 \pm 0.13$. The reduced facet efficiency is attributed to phase broadening of the laser light as it is reflected from the surface that has sub wavelength height

variations. AFM measurement of an etched facet height distribution has been used to infer a resulting facet efficiency value of $\eta = 0.41$. To improve etched facet efficiency, surface roughness would need to be reduced by optimising the electron beam lithography/plasma etching processes that have been used.

In chapter 4 the sensing capability of the prototype coupled-cavity device has been explored. Perturbation of the optical coupling between the two laser sections of the device can induce a wavelength shift in the laser output of $\Delta\lambda = 20 \pm 5 \text{ \AA}$. This change in wavelength has been attributed to the difference in the threshold gain requirements of the coupled-cavity and individual cavity allowed modes.

Interruption of the optical coupling causes the device to switch from lasing as a coupled-cavity to operating as two individual lasers. Rate equation modelling has been used to predict that, for the GaInP quantum well material used in this work, the size of the coupling effect can be maximized by minimising the cavity lengths of the individual laser sections of the device.

Gain leveraging and self-pulsation have been investigated as means of enhancing the sensing capability of the coupled-cavity device. Gain leveraging has been used to demonstrate a continuous wavelength tuning range of $\Delta\lambda = 1.2 \pm 0.2$ in a segmented contact laser. The wavelength tuning behaviour has been attributed to the carrier density dependence of the peak net modal gain spectrum. A set of design criteria have been defined that can be used to maximise the tuning range of gain levered devices. The rate equation model has also been used to demonstrate how an absorber section could provide a facility for frequency tuneable self-pulsation and a means of amplifying optical input for enhanced sensing.

The monolithic coupled-cavity semiconductor laser is a promising candidate for μ TAS cell biology applications. The monolithic nature of the device offers inherent advantages in terms of alignment and proximity of the analyte and sensor. Furthermore, this work has demonstrated the versatility of this configuration by identifying a number of different mechanisms which could be used for bio-sensing: direct detection in the source/detector mode, coupled-cavity sensing and the use of the gain lever mechanism for enhanced optical pump sensing.

6.2 Future work

One of the major challenges of this project has been the development of the prototype micro-fluidic coupled-cavity device that has been the basis of this investigation. Although many of the fundamental device fabrication issues have been dealt with during the course of the project, the micro-fluidic cell delivery system has not yet been tested on a working laser. One of the main focuses of future work therefore, would be to complete this element of the design so that the prototype device can then be used as a generic platform for future experimental investigations.

Once the micro-fluidic elements are operational, micro beads could then be used to simulate the influence of biological cell samples on the coupling between the laser sections of the device. A simple test would be to operate the device in source/detector mode and measure the effect that a passing bead has on the detector photocurrent. It is quite possible that, due to the width of the waveguide used in the prototype device (typically around 60 μm), a 10 μm bead, for example, would have only a negligible effect on the coupling. If so, it may be necessary to incorporate a narrow ridge waveguide system (see figure 6.1) into device design in order to maximise the influence that the analyte has on optical coupling.

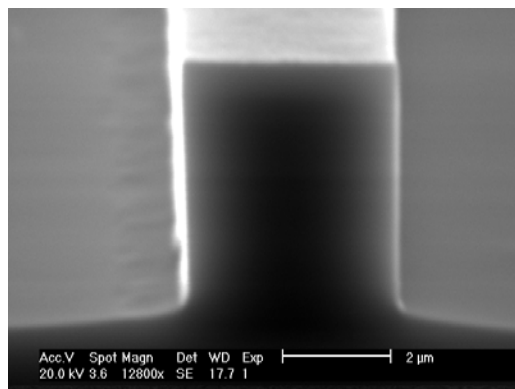


Figure 6.1 SEM image of a roughly 4 μm wide narrow ridge waveguide fabricated using the plasma etching process described in section 2.5[†].

In chapter 4 the rate equation model was used to demonstrate how the coupled-cavity sensing mechanism can be optimised. For the GaInP/AlGaInP quantum well material used for the prototype device, this would require cavity lengths of around $L_c = 300 \mu\text{m}$. Individual cavity lengths less than $L_c = 800 \mu\text{m}$ are incompatible with the present device design due to the real estate requirements of the micro-fluidics. As an alternative to reducing the cavity size, a semiconductor material that provides less gain could be used to allow longer laser cavities whilst still operating in the saturated part of the gain – carrier density curve where the coupled-cavity sensing effect is at its greatest. Quantum dot materials would be ideal for this as they saturate at much lower gain values than quantum wells, see figure 6.2.

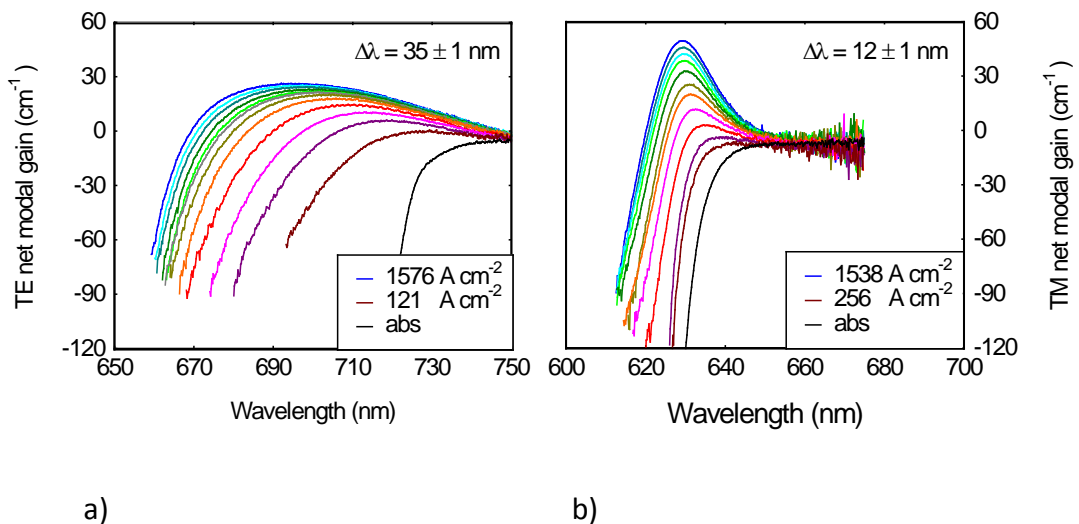
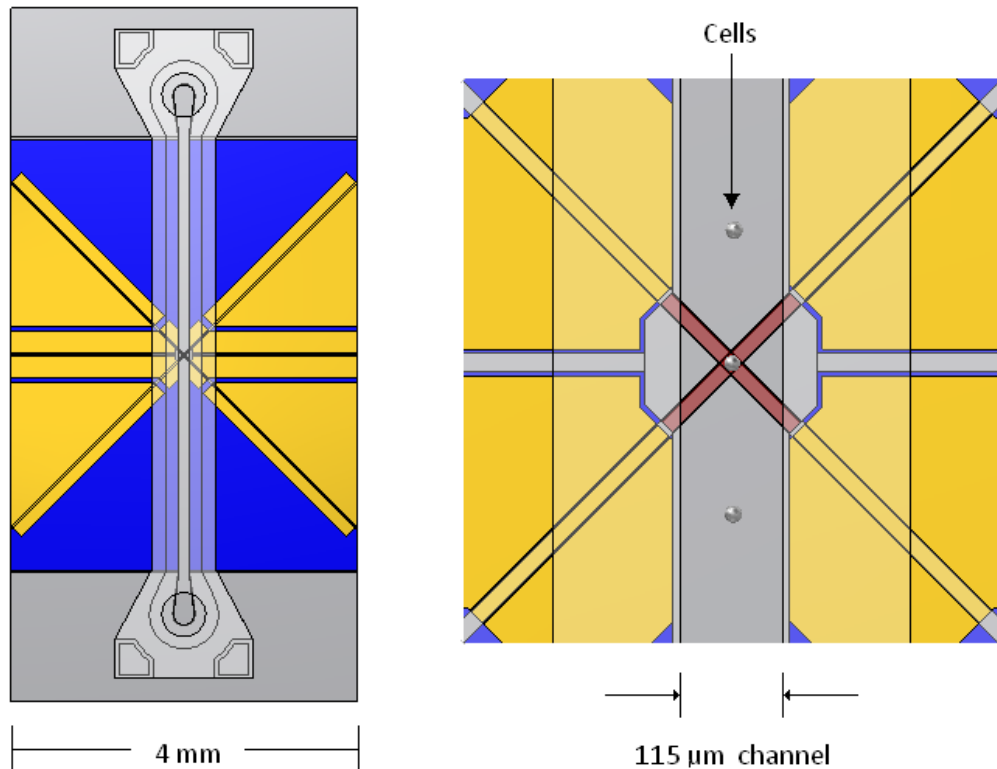


Figure 6.2 (a) TE net modal gain spectra for an InP quantum dot material with a peak net modal gain wavelength shift of $\Delta\lambda = 35 \pm 1 \text{ nm}$ for the measured current density range[†]. **(b)** TM net modal gain spectra for the GaInP quantum well material used in this project plotted over a 100 nm wavelength range for comparison. The peak net modal gain wavelength shift over a similar current density range to the dot material is $\Delta\lambda = 12 \pm 1 \text{ nm}$.

An optimised quantum dot coupled-cavity detector should also produce a much larger wavelength shift for a given threshold gain change. The quantum well material used in this project has a narrow spectral bandwidth and the peak of the gain only undergoes a small wavelength shift with current density, see figure 6.2 (b). Quantum dot materials by comparison have much broader gain spectra and

[†] Private communication with S. Shutts, Physics Dept, Cardiff University CF24 3AA, March 2012.

the gain peak shifts over a relatively large wavelength range. This also implies much greater scope for wavelength tuning using the gain-levering effect. The optical pump sensing mechanism that was identified in chapter 5 could be utilised within future device designs such as the coupled-cavity flow cytometer, see figure 6.3.



a)

b)

Figure 6.3 (a) Plan view of the proposed coupled-cavity flow cytometer with four crossed segmented contact lasers intersecting a micro-fluidic channel. (b) Close up of the interrogation region of the device with cells passing through the optical axes of the crossed lasers.

The traditional flow cytometer (illustrated in figure 1.1) has been emulated using a crossed segmented contact laser configuration; one laser would be operated as an optical pump, or source, while the other three would serve as detectors. The forward and side scattered light measured from each passing cell could then be analysed using statistical techniques, such as the cytograms plotted in figure 1.2. This device is just one example of how photonic structures could be combined with micro-fluidics in the future to offer great potential for bio-sensing.

Appendix 1: Scattering matrix elements

This appendix provides a derivation of the scattering matrix elements, equations 1.16 and 1.17, that are combined to obtain the complex coupling parameter used in the coupled-cavity threshold gain model introduced in chapter 1. Figure A1.1 shows a schematic illustration of the multiple internal reflections and transmissions that occur when light from laser section 1 passes into the gap coupler of a symmetrical coupled-cavity device i.e. one where the refractive index is the same in each of the laser cavities.

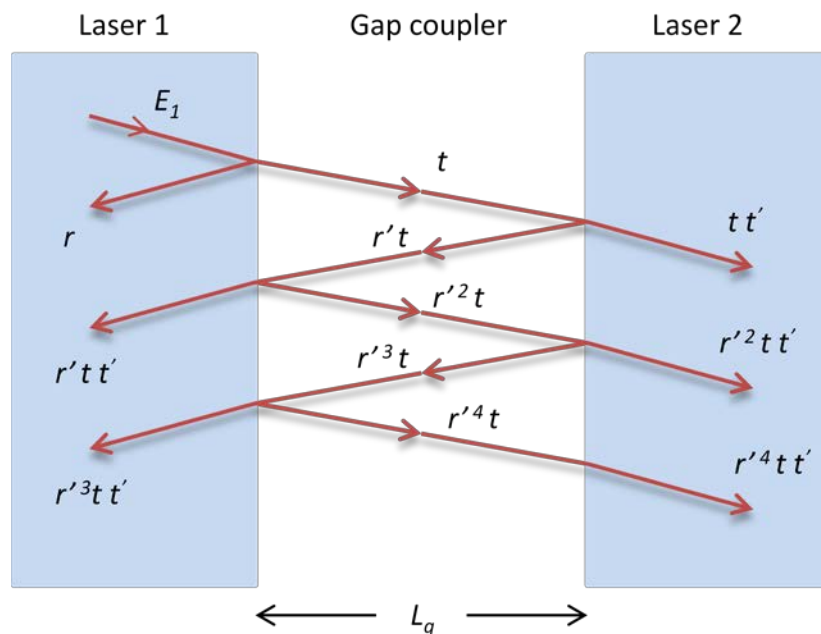


Figure A1.1 Schematic illustration of the multiple internal reflections and transmissions that occur inside the gap coupler of the coupled-cavity device.

The electric field of the light entering the gap coupler from laser section 1 can be approximated as a plane wave solution to Maxwell's equations:

$$E_1 = E_0 \exp(i(\omega t - kx)) \quad \text{A1.1}$$

where ω is the angular frequency of the E-field and k is its propagation constant in the x-direction. The amplitude reflectivity coefficients for the light that is reflected back into the laser section is labelled r and the light reflected back into the gap is r' . Assuming a normal angle of incidence, then

$$r = -r' \quad \text{A1.2}$$

where the minus sign accounts for the π phase shift that occurs on reflection from a material with a larger refractive index than that of the gap. The amplitude transmission coefficient is labelled t for light passing from higher to lower refractive index and t' for light passing from a lower to a higher refractive index material. For lossless transmission across the gap, conservation of energy demands that

$$t t' = (1 - r^2) \quad \text{A1.3}$$

The total reflection and transmission of the electric field amplitude E_1 at the gap can be determined by summing each of the individual round trip contributions shown in figure A1.1 to obtain the scattering matrix elements. For the reflection

$$S_{11} = [r + r' t t' e^{-i2kL_g} + r'^3 t t' e^{-i4kL_g} \dots] e^{i\omega t} \quad \text{A1.4}$$

and for the transmission

$$S_{12} = [t t' e^{-ikL_g} + r'^2 t t' e^{-i3kL_g} + r'^4 t t' e^{-i5kL_g} \dots] e^{i\omega t} \quad \text{A1.5}$$

Using equations A1.2 and A1.3, equations A1.4 and A1.5 simplify to

$$S_{11} = r - \frac{(1 - r^2)}{r} \sum_{p=1}^N [r^2 \exp(i2kL_g)]^p$$

A1.16

$$S_{12} = (1 - r^2) \sum_{p=1}^N (r^2)^{p-1} [\exp(ikL_g)]^{2p-1}$$

A1.17

Appendix 2:

Gaussian beam gap loss model

This appendix describes a Gaussian beam spreading model that has been used to estimate the reduction in coupling strength that occurs in the coupled-cavity laser because of the diffraction losses that are incurred by the optical mode as it traverses the gap coupler. The losses are assumed to be dominated by diffraction from the narrowest dimension of the waveguide, in this case, the direction perpendicular to the plane of the active layer with the losses in the other transverse direction being ignored as they are considered negligible by comparison (wide slab waveguide approximation).

The fundamental mode of the waveguide is assumed to have a Gaussian E-field distribution in the z-direction

$$E(z) = E_0 \exp\left(\frac{-z^2}{w_0^2}\right) \quad (\text{A2.1})$$

where w_0 is the beam width at which the field amplitude has dropped to 1/e of its peak value E_0 . The E-field of the mode propagating across the gap is modelled using the modified Gaussian distribution

$$E(x, z) = E_0 \frac{w_0}{w(x)} \exp\left(\frac{-z^2}{w(x)^2}\right) \quad (\text{A2.2})$$

where the beam width $w(x)$ increases with distance travelled in the x-direction according to equation A2.3, see figure A2.1, which also causes the peak amplitude to be reduced by a factor of $w_0/w(x)$.

$$w(x) = w_0 \sqrt{1 + \left(\frac{\lambda x}{\pi w_0^2} \right)^2}$$

(A2.3)

where λ is the wavelength of the light inside the gap.

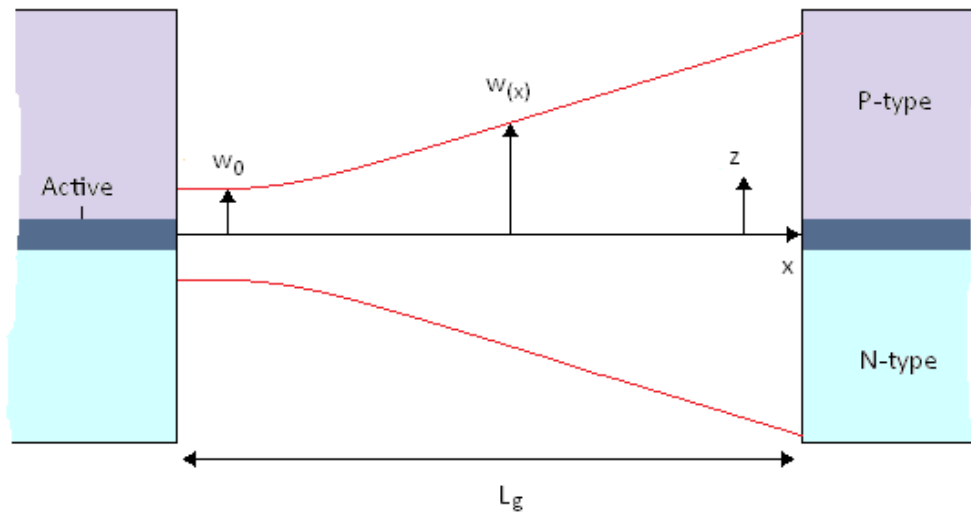


Figure A2.1 The Gaussian beam width $w(x)$ diverges from its waveguide value of w_0 as the mode propagates in the x direction across the gap.

The coupling efficiency of the gap coupler can be estimated by considering how much of the optical power emitted by one of the laser sections is coupled into the fundamental transverse mode of the other. This is done by calculating the overlap integral of the incident E-field distribution, E_{inc} , with the E-field distribution of the waveguide mode, E_{mode} .

The normalized power coupling efficiency $P(x)$ of the gap coupler can then be written as

$$P(x) = \frac{|\int E_{inc}^* E_{mode} dz|^2}{\int E_{inc}^* E_{inc} dz \int E_{mode}^* E_{mode} dz} \quad (A2.4)$$

Describing E_{mode} and E_{inc} with equations A2.1 and A2.2 respectively, equation A2.4 becomes

$$P(x) = \frac{\left| \int \exp\left(-z^2 \left(\frac{1}{w(x)^2} + \frac{1}{w_0^2}\right)\right) dz \right|^2}{\int \exp\left(\frac{-2z^2}{w(x)^2}\right) dz \int \exp\left(\frac{-2z^2}{w_0^2}\right) dz} \quad (A2.5)$$

using the definite integral:

$$\int_{-\infty}^{\infty} \exp(-ax^2) dx = \sqrt{\frac{\pi}{a}} \quad (A2.6)$$

equation A2.5 simplifies to

$$P(x) = \frac{2w_0 w(x)}{w(x)^2 + w_0^2} \quad (A2.7)$$

The fraction of the electric field amplitude that is coupled from one laser section to the other after a single pass of the gap coupler is

$$F(L_g) = \sqrt{P(L_g)} \tag{A2.8}$$

where L_g is the length of the gap coupler.

This discrete single pass loss can be converted to a distributed gap loss, α_g , defined as the fractional reduction in the electric field amplitude per unit distance travelled across the gap

$$\alpha_g = -\frac{1}{E} \frac{\Delta E}{\Delta x} = \frac{\ln(F(x)^{-1})}{x} \tag{A2.9}$$

Appendix 3:

Table of cleaved and etched facet laser properties

Table A3.1 Summary of the cleaved-cleaved facet (C-C) and cleaved-etched facet (C-E) laser properties used to calculate device threshold current densities in chapter 3.

Device	L (μm) $\pm 2 \mu\text{m}$	w (μm) $\pm 2 \mu\text{m}$	I_{th} (mA) $\pm 2 \text{ mA}$	J_{th} (A cm^{-2})
S1CC(a)	366	71	263	1012 ± 30
S1CC(b)	420	71	286	959 ± 28
S1CC(c)	585	71	313	754 ± 22
S1CC(d)	790	71	397	708 ± 20
S1CC(e)	993	71	453	643 ± 18
S2CC(a)	318	62	236	1197 ± 41
S2CC(b)	449	62	252	905 ± 30
S2CC(c)	608	62	284	753 ± 25
S2CC(d)	748	62	315	679 ± 22
S2CC(e)	755	62	321	686 ± 23
S2CC(f)	900	62	367	658 ± 22
S1CE(a)	782	71	416	749 ± 21
S1CE(b)	1005	71	471	660 ± 19
S1CE(c)	1005	71	491	688 ± 20
S2CE(a)	452	62	281	1003 ± 33
S2CE(b)	582	62	314	870 ± 29
S2CE(c)	765	62	370	780 ± 26
S2CE(d)	762	62	380	804 ± 26
S2CE(e)	906	62	400	712 ± 23
S2CE(f)	900	62	434	778 ± 25
S2CE(g)	1218	62	516	683 ± 22